

**Commissioning of a Model of the IBA Universal Nozzle
in Double Scattering Mode in the Monte-Carlo Tool TOPAS
at the University Proton Therapy Dresden**

Master Thesis
for the acquisition of the academic degree
Master of Science (M. Sc.)

submitted by

Jan Eulitz
born on April 11th 1990
in Dresden, Germany

Institut für Kern- und Teilchenphysik
Technische Universität Dresden
&
Oncoray - National Center for Radiation Research in Oncology
2017

submitted on March 9th 2017

Primary Reviewer: Prof. Dr. Arno Straessner

Secondary Reviewer: Prof. Dr. Wolfgang Enhardt

Supervisors: Dr. Armin Lühr, Dr. Benjamin Lutz

Abstract

Purpose Monte-Carlo simulations for proton therapy have the potential to reduce the measurement effort for each patient and to reduce range margins that are related to dose calculation uncertainties. They allow to estimate variable relative biological effectiveness (RBE) distributions in a patient and help to quantify the effect of applying variable RBE models in proton therapy. An accurately benchmarked Monte-Carlo model will support the research and medical physicists by providing and delivering relative and absolute dose, particle fluence and linear energy transfer distributions in and outside the patient. There is still a gap between the routine use of Monte-Carlo simulations in physics and the usage of the Monte-Carlo technique for practical research purposes in medical physics. This master thesis aims to bridge the gap by commissioning a Monte-Carlo model of the proton therapy treatment head at the University Proton Therapy Dresden (UPTD), in order to predict measured dose distributions in a water phantom within clinical tolerances.

Methods For patient treatment at UPTD, a so-called universal nozzle is used. Until now, patients are only treated within the so-called double-scattering mode at UPTD. A model of the universal UPTD nozzle in double-scattering mode is commissioned in the Monte-Carlo software TOPAS (TOol for PArTicle Simulation). Deviations between simulated and measured dose distributions in a water phantom are systematically reduced by adjusting the initial beam energy distribution, the thicknesses of the single scatterer foils and the time-dependent modulation of the beam current in the 4D Monte-Carlo simulation. After adjustment, the accuracy of TOPAS in simulating relative and absolute doses in a water phantom is studied. So-called output factors, relating dosimeter readings to absolute dose in a treatment field, are simulated and systematically compared to measurements. The specific nozzle settings for the simulation of one proton treatment plan (glioma) are implemented in TOPAS. Simulated dose distributions in the patient are compared to predictions from the treatment planning system in order to estimate the accuracy of the automated TOPAS implementation of the proton plan. Deviations between the simulated and planned dose distributions are quantified. The distribution of the linear energy transfer (LET) is simulated in the patient. Based on the simulated LET and biological input data from in-vitro cell experiments (glioma cells) a variable relative biological effectiveness (RBE) is calculated and dose deviations between the variable and the constant RBE model are studied.

Results The adjusted simulated depth-dose distributions predict the plateau regions of measured depth-dose curves within 1% accuracy. The absolute range differences ΔR_{90} and ΔR_{80} between the measured and simulated distal fall-off regions are below 0.15 mm for all nozzle options. The maximum range difference ΔR_{20} is ≤ 0.54 mm. Systematic uncertainties of the beam current modulation at the proximal shoulder region are obtained. The absolute maximum difference between simulated and measured lateral profiles in the field size is $W_{50} \leq 0.95$ mm and for the lateral penumbras it is $P_{\text{left}}, P_{\text{right}} \leq 0.55$ mm. The current accuracy of the output factor prediction in TOPAS is 3%. It can be improved to 2%, when applying nozzle option dependent calibration factors. The absolute dose of the planned dose distribution (treatment planning system) for a patient is predicted with gamma pass rates above 95% at the high dose region, when applying a local gamma criterion of 1 mm and a dose criterion of 3%. Systematic deviations between the simulated and planned dose distribution

are observed at the field plateau edges and at regions with high material density gradients. The positions of the simulated and planned dose grid are similar within the resolution of one voxel, which is 2 mm. Systematic dose fluctuations up to 2% occur in the simulated dose profiles in the patient, which appear too large to be solely explained with statistical dose fluctuations of the Monte-Carlo simulations. At the distal field edges of the central plateau region the simulated linear energy transfer increases up to 10 keV/ μ m. Hot spots of a calculated variable relative biological effectiveness (RBE) distribution in the patient are observed in regions with high LET spikes and can increase up to RBE = 1.6. In addition, RBE values below 1.1 occur in the target volume. The dose (RBE), which is predicted by using the variable RBE model is up to 15% higher in the distal plateau edges compared to the one that is derived by applying a constant RBE of 1.1.

Conclusions The commissioned Monte-Carlo model allows to predict relative doses in a water phantom within the clinical tolerances. When applying further improvements of the adjusted model parameters, it might be possible to simulate absolute doses within the measurement uncertainty. The model is ready to be used for automated simulations of proton treatment plans and the prediction of absolute planned dose distributions in the field plateau regions within clinically relevant accuracies. The simulation tool represents a solid basis for future RBE studies in patients by providing spatial distributions of the physical quantities that determine the radiobiological effect of proton irradiation.

Kurzfassung

Motivation Monte-Carlo Simulationen haben das Potential den Messaufwand pro Patient zu reduzieren und können dazu beitragen, den Anteil der Reichweitetoleranzen zu verkleinern, welcher durch Unsicherheiten der Dosisvorhersage im Patienten verursacht wird. Zudem erlaubt es die Monte-Carlo Methode Vorhersagen über die variable relative biologische Wirksamkeit (RBE) im Patienten zu treffen, und kann dazu genutzt werden, den Effekt eines variablen RBE in der Protonentherapie zu quantifizieren. Ein präzises, an Messdaten adjustiertes Monte-Carlo Modell, unterstützt die Physiker und Medizinphysiker an der Universitätsprotonentherapie Dresden durch Vorhersagen von relativen und absoluten Dosisverteilungen, sowie Fluenz- und LET- (Linear Energy Transfer) Verteilungen im und außerhalb des Patienten. Im Vergleich zum routinierten Einsatz der Monte-Carlo Methode in der Physik werden die Vorteile von Monte-Carlo Simulationen für angewandte Fragestellungen in der Medizinphysik noch zu wenig genutzt. Die vorliegende Masterarbeit trägt dazu bei, diese Lücke weiter zu schließen, indem ein Monte-Carlo Modell des Strahlausgangs der Protonentherapieanlage an der UPTD kommissioniert wird, mit dem Ziel, gemessene Dosisverteilung in einem Wasserphantom innerhalb klinischer Toleranzen zu reproduzieren.

Methoden Für die Protonenbehandlungen an der UPTD wird eine sogenannte universelle Nozzle eingesetzt. Bis jetzt werden Patienten ausschließlich im so-geannten "double-scattering"-Modus behandelt. Ein Modell der universellen UPTD Nozzle im "double-scattering"-Modus wird in der Monte-Carlo Softwareumgebung TOPAS (TOol for PArticle Simulation) kommissioniert. Abweichungen der simulierten Dosisverteilungen von den Messdaten werden systematisch reduziert, indem die Protonen-Strahlquelle, einzelne Streufolien und die zeitlich Modulation der Strahlintensität in der 4D Monte-Carlo Simulation adjustiert werden. Sogenannte Output-Faktoren, welche die Dosimeterausgabe zur absoluten Dosis im Bestrahlungsfeld in Relation setzen, werden simuliert und systematisch mit Messdaten verglichen. Die spezifischen Einstellungen der Nozzle, welche für die Simulation eines Protonenplans (Glioma Patient) notwendig sind, werden in TOPAS implementiert. Simulierte Dosisverteilungen im Patienten werden mit den Berechnungen des Bestrahlungsplanungssystems verglichen, um Aussagen über die Genauigkeit der TOPAS-Simulationen im Patienten treffen zu können. Zudem wird der lineare Energietransfer (LET) im Patienten simuliert und darauf aufbauend ein variables Modell der relativen biologischen Wirksamkeit angewendet. In das Modell fließen biologische Parameter aus in-vitro Zellexperimenten (Glioma Zellen) ein. Die RBE gewichteten Dosen des variablen RBE-Modells werden mit den simulierten Dosisverteilungen verglichen, welche einen konstanten RBE von 1.1 annehmen.

Resultate Die adjustierten simulierten Tiefendosiscurven sagen den Plateaubereich der gemessenen Dosisverteilungen innerhalb der klinischen Toleranz von 1% voraus. Die Reichweitenunterschiede ΔR_{90} and ΔR_{80} zwischen den simulierten und gemessenen Tiefendosiscurven sind ≤ 0.15 mm für alle Nozzle-Optionen. Die maximale absolute Reichweitedifferenz ΔR_{20} ist ≤ 0.54 mm. Systematische Unsicherheiten der optimierten zeitlichen Modulation des Protonenstrahls können beobachtet werden, insbesondere im proximalen Schulterbereich der Tiefendosiscurven. Die maximalen absoluten Differenzen zwischen den simulierten und gemessenen lateralen Dosisprofilen liegen im Bereich ≤ 0.95 mm für die lateralen Feldgrößen W_{50} und innerhalb von 0.55 mm für die sogenannten lateralen

Penumbras, welche die lateralen Feldkanten beschreiben. Die aktuelle Vorhersagegenauigkeit der Output-Faktoren liegt bei 3 %. Durch die Einführung konstanter Kalibrierungsfaktoren innerhalb jeder Option kann die Genauigkeit auf 2 % verbessert werden. Die absolute Dosis, welche vom Bestrahlungsplanungssystem für einen Protonen-Bestrahlungsplan errechnet wird, kann durch simulierte Verteilungen derart vorhergesagt werden, sodass im zentralen Hochdosisbereich Übereinstimmungen $\geq 95\%$ erreicht werden, welche durch sogenannte Gamma-Pass-Rates (GPR) beschrieben werden. Das verwendete geometrische Kriterium der verwendeten Gamma-Analyse ist 1 mm und das dazugehörige Dosis-Kriterium ist 3 %. An den Plateaugrenzen des Bestrahlungsfeldes und in Regionen hoher Material-Dichtegradienten können systematische Unterschiede zwischen den simulierten und geplanten Dosisverteilungen beobachtet werden. Die Patienten-Positionierung in TOPAS relativ zum Bestrahlungsplanungssystem ist auf einen Voxel genau (2 mm). In den simulierten Dosisprofilen werden systematische Dosisfluktuationen in der Größenordnung von 2 % beobachtet, welche als zu groß anmuten, um allein auf statistische Unsicherheiten der Monte-Carlo Simulation zurück geführt werden zu können. An den distalen Feldkanten werden LET Werte bis zu $10 \text{ keV}/\mu\text{m}$ voraus gesagt. Die Bereiche mit hohen RBE Werten korrespondieren zu den Regionen mit hohen LET Werten und können an den Feldgrenzen Werte von bis zu 1.6 erreichen. Gleichzeitig, werden RBE Bereich mit Werten ≤ 1.1 im bestrahlten Volumen errechnet. Die Unterschiede zwischen den Dosen, welche mit einem variablen RBE gewichtet wurden zu denen, welche mit einem konstanten RBE von 1.1 gewichtet sind, können bis zu 15 % betragen.

Schlussfolgerungen Das kommissionierte Monte-Carlo Modell erlaubt die Vorhersage von relativen Dosisverteilungen in einem Wasserphantom innerhalb klinischer Toleranzen. Durch eine weitere Optimierung der Parameter, welche zur Adjustierung der Simulation benutzt wurden, und eine verbesserte Beschreibung des Dosimeter-Messvolumens in TOPAS, ist die Vorhersage von absolute Dosisverteilungen innerhalb der Messunsicherheit von 1 % möglich. Das Model is fertig adjustiert für die automatisierte Simulation von Protonenplänen an der UPTD und benutzt werden um absolute Dosisverteilungen im Patienten innerhalb klinisch akzeptierter Toleranzen vorherzusagen. Durch die Vorhersage von räumlichen Verteilungen physikalischer Größen im Patienten, welche die relative biologische Wirksamkeit von Protonen bestimmen, ist eine Basis für zukünftige RBE Studien in Patienten geschaffen.

Contents

Glossary	X
List of Figures	XIII
List of Tables	XIV
1 Introduction	1
2 Theoretical Foundations	5
2.1 Proton Interactions in Matter	5
2.1.1 Stopping	5
2.1.2 Scattering	6
2.1.3 Nuclear Interactions	8
2.2 Proton Beam Description	9
2.2.1 Macroscopic Proton Beam Parameters	9
2.2.2 Physical Dose Distribution of Protons	10
2.2.3 The Monte-Carlo Method	12
2.2.4 Therapeutic Dose Distribution of Protons	13
2.2.5 Aspects of Proton Radiobiology	16
2.3 Passive Scattering in Proton Therapy	19
2.3.1 Beam Adaption Techniques	19
2.3.2 Output Factors	24
3 Materials and Methods	27
3.1 Adjustment and Validation of TOPAS Dose Distributions	33
3.1.1 Adjusting TOPAS SOBP Fall-Off Region	36
3.1.2 Adjusting TOPAS SOBP Range	40
3.1.3 Implementing TOPAS Beam Current Modulation	42
3.1.4 Validating TOPAS Depth-Dose Curves	46
3.2 Output Factor Simulations for Absolute Dosimetry	47
3.2.1 Comparison between TOPAS OF Simulations and Reference Measurements	47
3.2.2 TOPAS Outputfactor Simulations for Patient QA	50
3.3 TOPAS Simulation of a Proton Treatment Plan	52
3.3.1 Automated Proton Plan Integration into TOPAS	53
3.3.2 Dose Simulations in a Patient CT	55
3.3.3 LET Simulation and RBE Calculation in a Patient CT	60

4 Results	63
4.1 Adjustment and Validation of TOPAS Dose Distributions	63
4.2 Output Factor Simulations for Absolute Dosimetry	71
4.3 TOPAS Simulation of a Proton Treatment Plan	76
5 Discussion	83
5.1 Adjustment and Validation of TOPAS Dose Distributions	83
5.2 Output Factor Simulations for Absolute Dosimetry	85
5.3 TOPAS Simulation of a Proton Treatment Plan	88
6 Summary and Conclusion	93
Bibliography	I
Acknowledgment	V
Selbständigkeitserklärung	VI
Appendix	VII
A Adjustment and Validation of TOPAS Depth-Dose Distributions	VII
B Output Factor Simulations for Absolute Dosimetry	XX
C TOPAS Simulation of a Proton Treatment Plan	XXVI

Glossary

AP Aperture

BCM Beam Current Modulation

BES Beam Energy Spread

BP Bragg Peak

CP Compensator

CS Contoured Scatterer

CT Computed Tomography

DICOM Digital Imaging and COmmunications
in Medicine

EES Energy Selection System

FS First Scatterer

GEANT4 GEometry ANd Tracking

HU Hounsfield Unit

IC Ion Chamber

ICRU International Commission on Radiation
Units and Measurements

IBA Ion Beam Applications

LINAC Linear Accelerator

MGH Massachusetts General Hospital

MU Monitor Units

NIST National Institute of Standards and Tech-
nology

OF Output Factor

PBS Pencil Beam Scanning

PP Pristine Bragg Peaks

PP1 First Pristine Bragg Peak

PS Passive Scattering

PSATR Physical Measurement Laboratory

RBE Relative Biological Effectiveness

RMW Range Modulation Wheel

SAD Source-to-Axis Distance

SOBP Spread Out Bragg Peak

SS Second Scatterer

TOPAS TOol for PArticle Simulation

TPS Treatment Planning System

UPTD University Proton Therapy Dresden

WET Water Equivalent Thickness

List of Figures

1.1	Protons vs Photons	1
1.2	Oncoray Buidling	2
2.1	Mean Excitation Energy	6
2.2	Stopping Power Aluminum	6
2.3	MCS Setting	7
2.4	MCS angle and energy loss	7
2.5	Bragg Peak Curve.	11
2.6	SOBP Notations.	15
2.7	LQ-Model	17
2.8	SOBP Notations.	17
2.9	Proton RBE Values	19
2.10	Scattering systems	20
2.11	RMW Principle of Operation.	21
2.12	Compensator Principle	22
2.13	Aperture UPTD	22
2.14	Compensator UPTD	22
2.15	Passive Scattering	23
3.1	Energy Selection System	29
3.2	TOPAS Nozzle Implementation	31
3.3	TOPAS Scatterers	31
3.4	TOPAS Range Modulation Wheel	31
3.5	Aperture TOPAS	32
3.6	Compensator TOPAS	32
3.7	Nozzle Simulation	32
3.8	Deviations	34
3.9	Water Phantom	34
3.10	Water Phantom	34
3.11	Bortfeld Fit	38
3.12	Mean Beam Energies	38
3.13	Measured BES	39
3.14	Iterative BES Calculation	39
3.15	PP1 Range Offset	41
3.16	All Offsets	41
3.17	Step Function	43
3.18	TOPAS Pristine Peaks	43

3.19	xi2-Fit	44
3.20	Absolute BCM Weights	44
3.21	BCM Function	44
3.22	Fit Deviation	45
3.23	Deviation Distribution	45
3.24	TOPAS IC23	48
3.25	SOBPs Reference Data	49
3.26	QA SOBPs constant Modulation	49
3.27	Calibration Points Patient 1 Field 1	51
3.28	Coordinate Systems	53
3.29	TOPAS Setup Patient 1 Field 1	57
3.30	TOPAS Setup Patient 1 Field 2	57
3.31	Stopping Power Distribution	58
3.32	Relative Mass Density Distribution	58
3.33	CT Image Patient 1	59
3.34	Plan Dose Image Patient 1	59
4.1	BES Curve	64
4.2	Initial Beam Energy Spectrum	64
4.3	PP1 Range Offsets	65
4.4	Comparison Reference $R_{\text{req}} = 19.8$ cm	66
4.5	Comparison Validation $R_{\text{req}} = 21.2$ cm	66
4.6	SOBP Fall-Off Offsets	67
4.7	SOBP Fall-Off Offsets Validation	67
4.8	Comparison Lateral Profiles	68
4.9	Field Sizes Lateral Profiles X	69
4.10	Field Sizes Lateral Profiles Y	69
4.11	Output Factors Reference Fields	72
4.12	Output Factors Constant Modulation	72
4.13	Output Factors with Constant Range 11 cm	73
4.14	Output Factors with Constant Range 18 cm	73
4.15	Output Factors Patient 1, Field 1	73
4.16	Output Factors Patient 1, Field 2	73
4.17	Full OF Distribution	74
4.18	Full OF Distribution with Option Calibration	74
4.19	Dose Distributions Patient 1	77
4.20	Patient 1 Dose Differences, Varying X , Y , Z Position	78
4.21	Patient 1 Convergence Analyze	79
4.22	Gamma Analyze Patient 1	80
4.23	GPR(Y) Distribution	80
4.24	TOPAS LET Distributions Patient 1	81
A	Adjusted TOPAS SOBP Reference Data	XIV
B	Adjusted TOPAS SOBP Validation Data	XV

C	Lateral Profiles SOBP 1	XVI
D	Lateral Profiles SOBP 2	XVII
E	Delta E	XVIII
F	Delta E	XVIII
G	Fit Stability	XIX
H	Output Factors with Constant Range 14 cm	XXIII
I	Output Factors with Constant Range 18 cm	XXIII
J	Output Factors with Constant Range 22 cm	XXIII
K	Output Factors with Constant Range 26 cm	XXIII
L	Output Factors $V_{IC23_{12}}$, V_{IC23_4}	XXIV
M	Output Factors Option Adjusted $V_{IC23_{12}}$, V_{IC23_4}	XXV
N	TOPAS Setup Patient 1 Field 1	XXVII
O	TOPAS Setup Patient 1 Field 1	XXVII
P	Dose Distributions Patient 2	XXVIII

List of Tables

2.1	Fractions of energy of 150 MeV proton beam	8
3.1	TOPAS Beam Source	29
3.2	Measurement Uncertainties	35
3.3	FS Foil Thicknesses	42
3.4	Parameters Points Patient1	52
3.5	Field and Nozzle Parameters Patient1	52
3.6	UPTD Coordinate Systems	56
3.7	DICOM Tags	56
3.8	Dose and CT Image Parameters	56
3.9	Chaudhary Input Parameters	60
4.1	Mean Option Offsets	65
4.2	Alpha Ratios	71
4.3	Gamma Analyze Patient 1	82
5.1	Results Comparison Dose Distributions	84
5.2	Results Output Factors	86
A	IBA Nozzle Sub-Options	VII
B	Reference and Validation Data	VIII
C	Lateral Validation Data	IX
D	Comparison Reference SOBP	X
E	Comparison Validation SOBP	XI
F	Comparison Validation Lateral 1	XII
G	Comparison Validation Lateral 2	XIII
H	OF:QA Reference Data	XXI
I	OF:QA Data constant Modulation	XXI
J	OF:QA Data constant Range	XXI
K	Mean Value and Variance of $\Delta\psi_{\text{rel}}$	XXII
L	Relative OF Errors Research Data Part 1	XXII
M	Relative OF Errors Research Data Part 2	XXII

1 Introduction

Over the past century, radiation oncology, one of the three big pillars in cancer therapy, has developed individualized treatments based on anatomical information combined with clinical parameters [1]. The technology-driven improvement of treatment conformity, including advanced image guidance and particle therapy, and novel biological concepts for personalized treatment, are two main strategies, acting synergistically, which will enable further widening of the therapeutic window of radiation oncology. The main advantage of particle therapy is the reduced total energy deposited in the patient as compared to photon techniques (Figure 1.1). This reduction is achieved, because of the finite range of the particle beam, which adds an additional degree of freedom to treatment planning [2], and the higher biological effect of protons compared to photons.

In particle therapy, the majority of patients are treated with protons. Because of the limited information on the proton beam distribution in the patient, proton therapy has not reached its full potential, yet. The dose distribution of a proton beam has a very sharp fall-off at its distal edge. Therefore, uncertainties of the proton beam range can have an impact on the clinical outcome of the therapy. Range uncertainties occur due to uncertainties in dose prediction, in patient positioning and due to anatomical changes during the course of treatment. To take these uncertainties into account safety margins are defined. One important goal of research in proton therapy is to reduce these range margins to minimize the dose that is deposited in the healthy tissue. Currently, several experimental techniques are under development, which aim to predict the proton beam range in the patient more precisely [3–5].

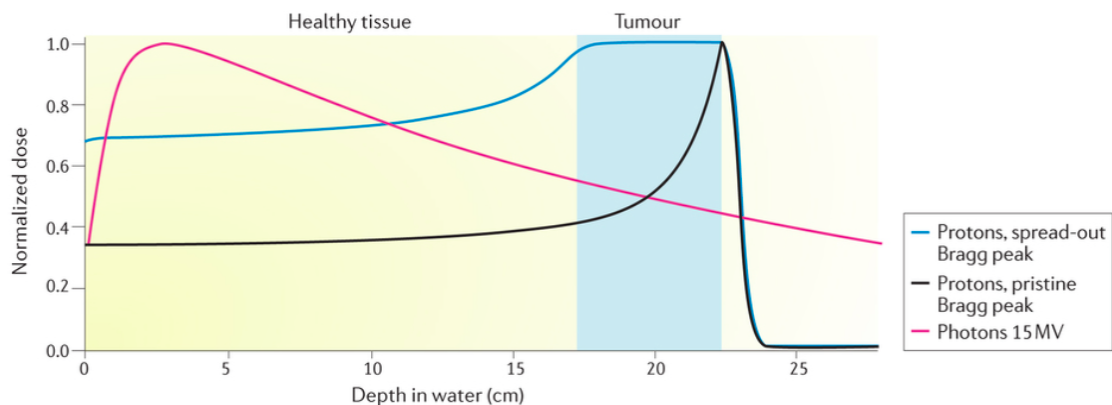


Figure 1.1: Schematic illustration of the differences in dose deposition between a clinical photon beam, created by a 15 MV linear accelerator (LINAC), and a therapeutic proton beam (spread-out Bragg peak) [1].

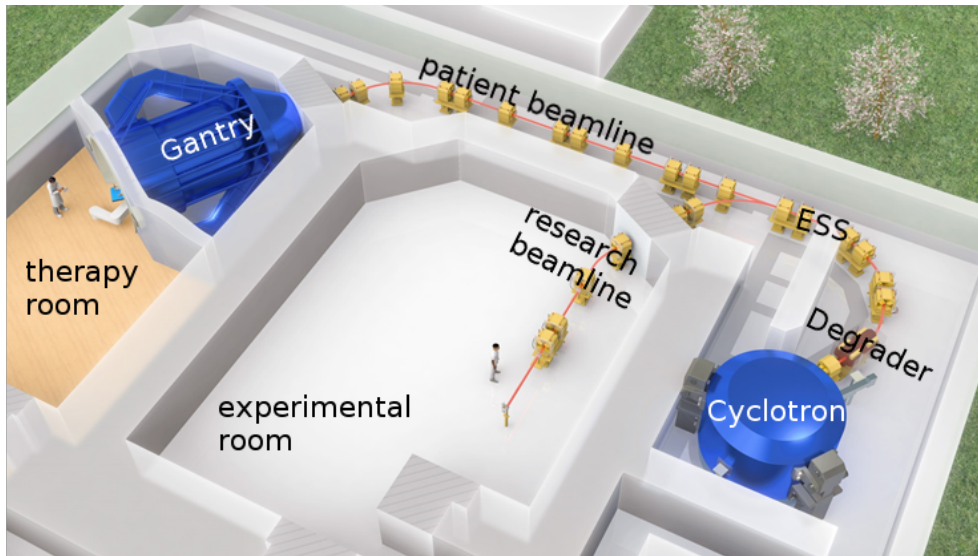


Figure 1.2: Schematic illustration of the proton therapy facility in Dresden, including the cyclotron proton accelerator, which delivers a 235 MeV proton beam, a degrader, which moderates the beam energy and the energy selection system (ESS), which adjusts the spatial, angular and energy beam distribution. The beam can be steered to a experimental and a treatment room by beam line components. The treatment room contains the gantry that rotates around the patient. The gantry contains the IBA universal nozzle.

Those techniques benefit from the usage of computer simulations, which can be used to inter- and extrapolate experimental data. The currently most accurate computational method to model a therapeutic proton beam is the so-called Monte-Carlo method. Monte-Carlo simulations allow to predict absolute doses, particle fluences and the linear energy transfer in- and outside of the patient. They have the potential to reduce range uncertainties that are related to dose calculation uncertainties and allow to study the influence of a variable relative biological effectiveness in proton therapy [2, 6]. However, there is still a gap between the routine use of Monte-Carlo simulations in physics and the usage of the Monte-Carlo technique for practical research purposes in medical physics. This master thesis aims to bridge the gap by commissioning a full 4D Monte-Carlo model of the patient treatment head at the University Proton Therapy Dresden (UPTD) .

The treatment head at UPTD is also called universal nozzle. A schematic illustration of the UPTD facility is illustrated in Figure 1.2. The nozzle was constructed and is still maintained by the company IBA (ion beam applications). It can deliver proton beams in a so-called double-scattering and a pencil-beam mode, while the pencil-beam mode is currently prepared for patient treatment. Until now, patients have only been treated within the double-scattering mode. A model of the IBA universal nozzle in double-scattering mode was implemented in the Monte-Carlo software TOPAS (TOol for Particle Simulation) [7]. The model requires a Monte-Carlo specific commissioning in order to be able to predict measured doses within the clinical tolerances. The objective of this thesis is to perform the commissioning by adapting the TOPAS model, in particular the beam source and the beam modulation, which are used in the 4D Monte-Carlo simulation.

As a first goal, relative depth-dose distributions should be simulated within the measurement uncertainty for all possible treatment fields. Secondly, absolute dose values in a water phantom should be predicted in the simulation within clinically relevant accuracy. The third goal is to provide a full

simulation of a proton treatment plan including the absolute dose distribution in the high dose region within clinical tolerances.

All three goals will be addressed within this thesis in three adjacent sub-chapters. The following chapter introduces based on the interactions of protons in matter the shape of therapeutic dose distributions in proton therapy. Furthermore, relevant clinical notations, aspects of proton radiobiology and technical principles of a double-scattering system including the concept of the output factor, are briefly introduced.

2 Theoretical Foundations

Based on the proton interactions in matter the physical and therapeutic depth-dose distribution is derived. Therefore, the benefit of the Monte-Carlo method in modeling dose distributions in proton therapy is outlined. Aspects of the proton radiobiology are introduced briefly in order to be able to explain the concept of the relative biological effectiveness. Technical principles of a double-scattering system in proton therapy are summarized and the concept of the output factor is introduced.

2.1 Proton Interactions in Matter

2.1.1 Stopping

The stopping of protons in matter can be described mainly by the so-called Bethe-Bloch equation for energies used in radiotherapy ([3 – 300 MeV]). At this energy regime protons stop in matter mainly through inelastic collisions in the Coulomb fields of the atomic electrons of the target material. For proton energies above 300 MeV energy loss through bremsstrahlung dominates, for energies below 3 MeV energy loss through nuclear interactions becomes dominant [8]. At the radiotherapy energy regime the proton energy loss through elastic Coulomb collisions with atomic nucleus and through bremsstrahlung is negligible.

The Bethe-Bloch-equation (Equation (2.1)) describes the energy loss per path length, which fast charged heavy particles (e.g. protons, alpha particles, heavier ions) do suffer as they traverse a material, through inelastic collisions with atomic electrons. The energy loss depends on the particle velocity and the target material. Bethe delivered the quantum mechanical relativistic form of his equation using quantum mechanical perturbation theory to the second order of the projectile proton number z (z^2). The higher perturbation orders correspond to further correction terms of the Bethe-Bloch-equation (z^3 Barkas-Andersen-effect, z^4 Bloch-correction [9]).

$$-\frac{dE}{dx} = \left(\frac{e^4}{4\pi\epsilon_0^2 m_e c^2} \right) \cdot n_e \cdot z^2 \cdot \frac{1}{\beta^2} \cdot \left[\frac{1}{2} \ln \left(\frac{2m_e c^2 \beta^2 \gamma^2 T_{\max}}{I^2} \right) - \beta^2 - \frac{\delta}{2} - \frac{C}{Z} \right] \quad (2.1)$$

e and m_e are the electron charge and mass. ϵ_0 is the electrical field constant. β and γ are relativistic parameters, which are functions of v the projectile velocity, and c , the velocity of light. n_e is the electronic density of the target material and contains the material density ρ , the atomic numbers of the material A and Z , and the unified atomic mass u . T_{\max} is the maximum energy which can be transferred to an electron in one inelastic collision. T_{\max} is a function of m_e , the projectile mass M and velocity v . The denominator is a Taylor polynomial until the second order in m_e/M . In first

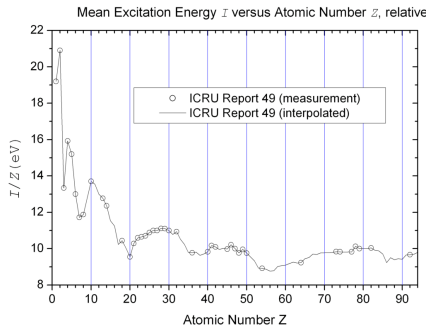


Figure 2.1: The mean excitation energy I of the elements, divided by the proton number Z of those elements. The plot is generated using data from the program PSTAR (NIST, [10]) and is kindly provided Prof. em. Dr. Helmut Paul.

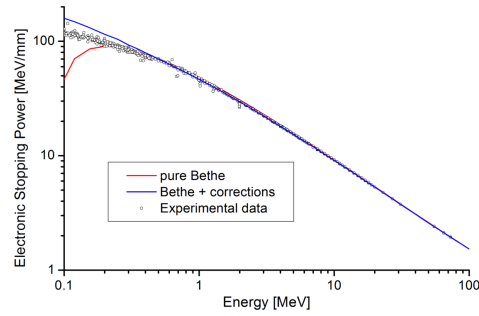


Figure 2.2: Stopping power of aluminum for protons as a function of the proton energy, including the Bethe-Bloch equation without (red) and with corrections (blue). The plots are generated using data from the program PSTAR (NIST, [10]) and are kindly provided Prof. em. Dr. Helmut Paul.

approximation, m_e/M is zero.

$$n_e = \frac{Z \rho}{A u} \quad \beta = \frac{v}{c} \quad \gamma = \frac{1}{\sqrt{1 - \beta^2}} \quad T_{\max} = \frac{2m_e c^2 \beta^2 \gamma^2}{1 + 2\gamma \left(\frac{m_e}{M}\right) + \left(\frac{m_e}{M}\right)^2} \quad (2.2)$$

I is the mean excitation energy (also I -value) of the target material. I and n_e are the material input parameters of equation (2.1). The I -value of an atom can be calculated by integrating over all electronic quantum states. For the elements those integral can be approximated numerically. Nevertheless, in radiation therapy one has to deal with tissue materials, that contain complex molecular structures. The electronic energy levels of those molecules cannot simply be derived from the energy levels of the elements. Therefore the I -value uncertainty can vary for different materials. Figure 2.1 illustrates measured and interpolated I -values for elements up to proton numbers of 92 .

There are two important corrections to the Bethe-Bloch equation. The first one is the so-called shell correction C/Z , and becomes important for low projectile velocities v (non-relativistic). If v is in the order of the electron orbital velocity in the target material, capturing processes play an increasing role and change the amount of transferred energy. The second correction is the so-called density correction $\delta/2$ and is important for high v (relativistic). The extended transversal component of the electrical field of a relativistic particle is shielded more or less by the electronic density of the atoms. The atom gets polarized and this has an impact on the energy loss of the relativistic particle. Figure 2.2 illustrates the stopping power of aluminum for protons as a function of the proton energy, whereby the Bethe-Bloch equation with and without corrections is compared to measurements.

2.1.2 Scattering

Scattering of protons in matter happens through various electromagnetic collisions with atomic nuclei. This statistical process is called multiple Coulomb scattering (MCS) and can be mapped to a random walk of the protons in angle. The sum of all small random deflections will lead to a Gaussian core and a single scattering tail from the not quite rare large single scatterers in the target.

In clinics, usually only the Gaussian part has to be considered for MCS, because it contains about 98 % of the protons [11, p. 37]. The Gaussian approximation is only valid if the amount of scattering material is large enough to ensure that there are enough scattering events to justify the dominance of the statistical nature of the process. But if the amount of scattering material becomes too large, the beam energy can no longer be assumed as to be constant. Shifts of the proton energy in the material have an influence on the scattering distribution of the protons. The lateral distribution $X(r)$ is defined as the amount of particles which traverse a measurement plane (MP). r is the lateral distance of each surface element from the MP center. The beam has a cylindrical symmetry. The MP is placed at distance L from the source. In Gaussian approximation, X_0 is defined as the root mean square (rms) of $X(r)$. The dependency of the scattering angle on X_0 and L is illustrated in Figure 2.3.

$$\tan \Theta_0 = \frac{X_0}{L} \quad \underline{L \gg X_0} \quad X_0 \approx L \cdot \Theta_0 \quad (2.3)$$

There are a lot of measured values of Θ_0 for a large assortment of thicknesses and target materials [11, p. 38]. In Gaussian approximation the dependence of Θ_0 on scattering material and proton energy can be described by Highland's formula. 14.1 MeV is a numerical constant [11, p. 38], pv the kinematic factor, d_S the scatter thickness and L_R the radiation length of the scatter material, which can be found in tables. Highland derived his formula by fitting a version of Molière's theory [12], which is one of the most comprehensive, accurate and elegant theory to describe MCS of protons in matter. Highland parameterized the full Molière's theory, with additions from Bethe and Hanson. A direct conclusion of Highland's formula is that high- Z materials (lead, tantalum) should be used for proton beam scattering, whereby low Z materials (lexan) have a small impact on Θ_0 . In stopping power it behaves in the opposite way, because the stopping power is proportionate to Z/A (Equation (2.1)).

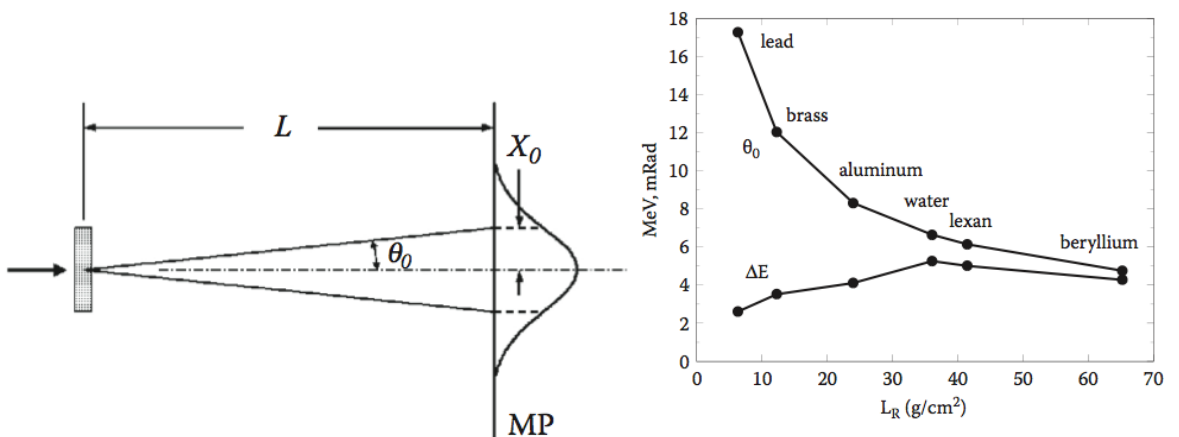


Figure 2.3: MCS in a Thin Slap including the measuring plane (MP), the root mean square spread X_0 and Θ_0 , which is usually smaller than 16° ([10], [11, p. 23]).

Figure 2.4: MCS Angle and Energy Loss. Multiple scattering angle and energy loss for 160 MeV protons traversing 1 g/cm^2 of various materials ([10], [11, p. 23]).

$$\Theta_0 = \frac{14.1\text{MeV}}{pv} \sqrt{\frac{D_S}{L_R}} \left[1 + \frac{1}{9} \log_{10} \left(\frac{D_S}{L_R} \right) \right] \text{ rad} \quad (2.4)$$

$D_S = d_S \cdot \rho_S$ d_S ... scatter thickness ρ_S ... scatter material density

$\tau \equiv \frac{E}{mc^2}$... reduced kinetic energy

$pv = \frac{\tau + 2}{\tau + 1} E = 297\text{MeV} (E = 160\text{MeV})$

$L_R = \frac{1432.8 \cdot A}{Z(Z + 1)(11.319 - \ln Z)} \frac{\text{g}}{\text{cm}^2}$... radiation length of the scatter material

2.1.3 Nuclear Interactions

Nuclear interactions are rare compared to the electromagnetic interactions of protons. They are more difficult to model and have a smaller biological impact. Nevertheless, they remain important, for instance, because of the production of free neutrons and high energetic photons. Both are neutral particles, which can travel long distances without interaction. The neutrons can produce unwanted dose deposition far away from the tumor region, through indirectly ionization (nuclear collisions with protons). High energetic photons (gamma radiation) can be used for tracking the proton beam in-vivo [3, 4].

There are three types of nuclear interaction: elastic, nonelastic and inelastic. In an elastic interaction total kinetic energy is conserved and target nuclei and projectile are unchanged by the reaction. In nonelastic and inelastic interactions total kinetic energy is not conserved. While in inelastic interactions final nucleus are the same as the bombarded nuclei, in nonelastic reactions the target can undergo breakup or can be excited in higher quantum state. Also particle transfer reactions may occur [11, p. 46]. So $^{16}\text{O}(p,p)^{16}\text{O}$ is an elastic reaction, $^{16}\text{O}(p,p)^{16}\text{O}^*$ (* means excited state) is inelastic and $^{16}\text{O}(p,2p)^{15}\text{N}$ is nonelastic. All protons from the source, which slow down in the material are called primaries, where particles from inelastic or nonelastic interactions called secondaries. Protons in H_2O can scatter with hydrogen at a relative angle of approximately 90° , share the original kinetic energy and may appear as secondaries. Therefore, they should be included in any counting of secondaries [11, p. 47]. Protons, neutrons, γ -rays, heavy fragments such as alphas and recoiling residual nuclei are possible secondaries from nonelastic interactions in a therapy energy regime, whereby heavier fragments than alphas are rare. Table 2.1 shows the fractions of E_{initial} that are carried away for secondaries of a 150 MeV proton beam modeled by a Monte Carlo simulation [13]. Heavy fragments carry little energy and that is why they have a lower relative biological effect (RBE), despite their high-ionization density [11, p. 48].

Table 2.1: Fractions of energy carried away by secondaries for 150 MeV proton beam [11, p. 47].

Particle	p	deuterium	tritium	^3He	α	Recoils	n
Fraction E_{initial}	0,57	0,016	0,002	0,002	0,029	0,016	0,20

2.2 Proton Beam Description

2.2.1 Macroscopic Proton Beam Parameters

The microscopic proton interactions determines the macroscopic beam characteristics. There are mainly four important macroscopic parameters, which are used in proton therapy to describe a proton beam, the stopping power S , the particle fluence ϕ , the dose D and the linear energy transfer LET.

The stopping power $S = \frac{dE}{dx}$ can be divided into three fractions, because there are three stopping processes of fast charged heavy particles in matter.

$$S = \frac{dE}{dx} = \frac{dE_{\text{col}} + dE_{\text{rad}} + dE_{\text{nuc}}}{dx} \approx \frac{dE_{\text{col}}}{dx} \quad E \in [3 \text{ MeV} | 300 \text{ MeV}] \quad (2.5)$$

dE_{col} refers to the proton energy loss, coming from the inelastic collisions with atomic electrons as described in Equation (2.1). dE_{rad} describes the proton energy loss through bremsstrahlung. dE_{nuc} represents the energy loss through elastic Coulomb collisions with atomic nucleus. At radiotherapy energies ($E \in [3 \text{ MeV} | 300 \text{ MeV}]$) dE_{col} is the dominant term.

The particle fluence ϕ describes the amount of particles dN , that cross an infinitesimal surface element dA . A more general definition would be to define ϕ as the integral over the particle flow density \vec{F} . \vec{F} is a vector field, which describes the amount of particles, that flow per surface element $d\vec{A}$ through a surface A .

$$\phi = \frac{dN}{dA} \quad \phi = \int_A \vec{F} \cdot d\vec{A} \quad (2.6)$$

The dose D , a proton beam deposit in a material, is defined as the amount of energy dE , which is deposited in a mass element dm . D can be expressed by the stopping power S , the particle fluence ϕ and the material density ρ . The majority of the dose of a proton beam is deposited by its secondary electrons.

$$D = \frac{1}{\rho} \cdot S \cdot \phi = dN \cdot \frac{V}{m} \cdot \frac{dE}{dx} \cdot \frac{1}{dA} = \frac{dV}{dx \cdot dA} \cdot \frac{dE}{dm} = \frac{dE}{dm} \quad (2.7)$$

The LET of a proton beam is defined as the stopping power, excluding secondary electrons above a certain energy threshold Δ_e . Therefore the LET can be understood as a localized stopping power. The proton energy loss, which leads to the production of high energetic secondaries, that transport the energy far away from the beam center is excluded. If Δ_e is infinite high, the LET and S fall together.

$$\text{LET}(\Delta_e < \infty) < S \quad \text{LET}(\Delta_e = \infty) = S \quad (2.8)$$

In radiation fields that contains a mixture of particles with different energies and/or masses, one distinguish between dose averaged and fluence averaged LET, depending on the question of interest. i

defines the number of different particle types.

$$\text{LET}_D = \frac{\sum_i \int \text{LET}(i, E) D_i(E) dE}{\sum_i \int D_i(E) dE} \quad (2.9)$$

$$\text{LET}_\Phi = \frac{\sum_i \int \text{LET}(i, E) \Phi_i(E) dE}{\sum_i \int \Phi_i(E) dE} \quad (2.10)$$

Locally densely ionizing radiation is called high-LET radiation, sparsely ionizing is called low-LET radiation.

2.2.2 Physical Dose Distribution of Protons

The dose D is the most important beam parameter in radiotherapy, because it is directly correlated to biological radiation damage (deterministic radiation damage). The dose distribution $D(z)$ of a certain radiation type in a material, integrated perpendicular to the depth z , is called depth-dose-distribution (DDD). The DDD of a certain radiation type, including the lateral dose deposition is relevant for the treatment planning. The three dimensional dose distribution of a proton beam $D(x, y, z)$ can often be reduced, at least in isotropic density materials, to two dimensions using cylindrical coordinates. This is justified, because a proton beam usually has cylindrical spatial symmetry, in first approximation.

$$D(x, y, z) \rightarrow D(r, z) \quad r = \sqrt{x^2 + y^2} \quad (2.11)$$

The DDD of a proton beam is called Bragg curve with its maximum called Bragg peak (BP). The BP is named after William Henry Bragg who discovered it in 1903. The characteristic shape of a Bragg curve is determined by the dependency of S on β and therefore on the proton velocity v (Equation (2.1)).

$$S \propto \frac{1}{\beta^2} \cdot f(\beta) \quad (2.12)$$

The $\frac{1}{\beta^2}$ dependency of S dominates the dependency of S on the v and therefore the proton energy transfer increases as the proton slows down. At the same time the proton fluence changes only moderately and as the material density stays constant too, the dose increases with decreasing proton velocity. Therefore, the dose, a proton beam would deposit in a material, increases with depth ($D(z) \propto \frac{1}{z^2}$) until a maximum. The maximum is reached because of proton fluence loss, that increases rapidly for small proton energies. This leads to a sharp dose fall-off behind the maximum of a Bragg curve. Figure 2.5 illustrates the shape of a Bragg curve (Monte-Carlo simulation) including the corresponding fluence and LET distributions.

The characteristic shape of a Bragg peak, allows to define a range for the DDD of protons and heavier ions. By definition, the range R is the depth of material, at which half of the protons have stopped, by undergoing just electromagnetic interactions. This corresponds approximately, to the material depth at 80% of the maximum dose at the distal fall-off region. In principle the range R (or mean projected range) of the proton beam can be derived by integrating the Bethe-Bloch equation. The range is approximately the total path length R_{total} . Because of the MCS of the protons in matter it is

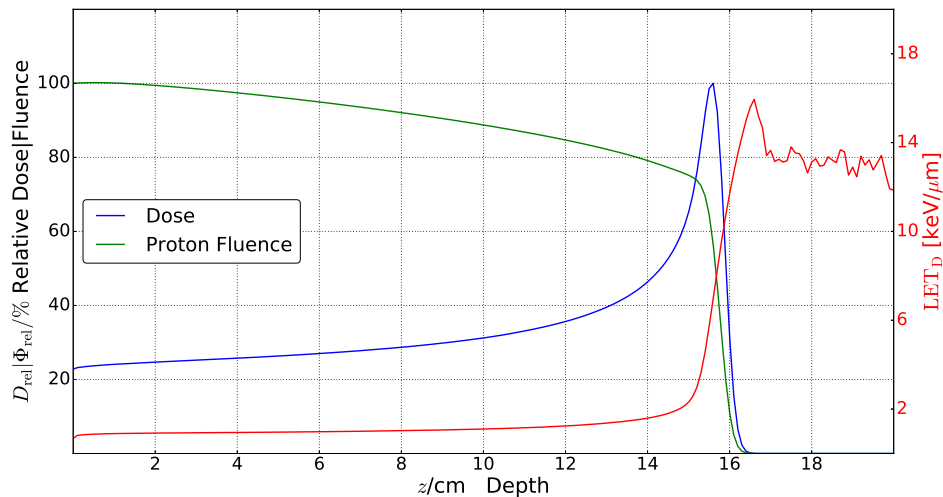


Figure 2.5: Illustration of the physical depth-dose distribution of a proton beam with Gaussian spatial, angular and energy distribution including the corresponding proton fluence and LET distribution. All distributions are generated by a Monte-Carlo simulation in a water phantom. The initial mean beam energy is approximately 150 MeV. 50 millions primary protons are simulated.

effectively somewhat smaller. For a 100 MeV proton beam in water R and R_{total} are similar within a 0.2% accuracy. [11, p. 35]).

$$R \approx R_{\text{total}}(E_{\text{initial}}) = \int_{E_{\text{initial}}}^{E_{\text{final}}} \left(\frac{1}{\rho} \frac{dE}{dx} \right)^{-1} dE = \int_{E_{\text{initial}}}^{E_{\text{final}}} \frac{dE}{S/\rho} \quad (2.13)$$

The sharpness of the peak of a Bragg curve is decreased through basically two processes, the range straggling and the spread of the initial beam energy distribution σ_E . Because the stopping of the individual protons, through a large number of inelastic collisions with atomic electrons, is a statistical process, not all protons stop at the same range. In first approximation, the range distribution of individual protons that lost all their energy E_0 is Gaussian. The real distribution is slightly asymmetric, because of multiple elastic scattering, which can make the (projected) range smaller, but never larger [14]. Next to the range straggling the initial beam energy distribution increases the spread of the Bragg peak. In reality, a proton beam is not mono-energetic. The energy spread σ_E depends on the individual characteristics of the accelerator, the beam guide, and the collimation system.

It is difficult to derive a general analytical expression of the three dimensional dose distribution a proton beam deposit in matter. Nevertheless, the author in Ref.[14] derived an analytical form of the Bragg curve $D(z)$, including range and energy straggling effects and proton fluence loss, by applying certain approximations. It might be even possible to derive an analytical representation of $D(r,z)$, by using the assumption a cylindrical symmetry. Those expressions have a great benefit in fitting measured or simulated data. Nevertheless, they are too inaccurate to be used in predicting doses in the patient within clinical tolerances. In clinics, so called treatment planning software (TPS) is used to predict the dose distribution in the patients. So-called pencil beam algorithms calculate the dose distributions using numerically deterministically procedures. The most general expression of the dose distribution $D(x,y,z)$, measured by a detector, would be an integral over the mechanical phase space

$$\Gamma = (x, y, z, p_x, p_y, p_z, t) = (x, y, z, E, \theta, \phi, t).$$

$$D = \int_{\Gamma} f(\Gamma) d\Gamma = \int_{\Gamma} g(\Gamma) J(\Gamma) d\Gamma \quad (2.14)$$

$g(\Gamma)$ is the detector response function and J the particle flow density. J defines the number of particles that flow through a surface A during a time t .

$$J = \frac{1}{A} \frac{dN}{dt} \quad (2.15)$$

J can be calculated using the particle transport equation, which is a special form of the Boltzmann equation [15]. It can be derived, by assuming a stationary particle flow equilibrium in a macroscopic volume V and an infinitesimal energy, angle and time element $dE d\Omega dt$.

$$\frac{dN}{dt} = 0 = J \cdot A = (A) + (B) - (C) - (D) \quad (2.16)$$

(A) stands for the primary particles in V from the source. (B) describes secondary particles, that are produced through interactions in V . Before the interaction they are in the state (E', Ω', t') and after in the state (E, Ω, t) . (C) stands for particles, that are leaving V . (D) describes the particles, which get absorbed in V or interact in V and therefore are leaving the state (E, Ω, t) . Using the concept of the stationary particle flow equilibrium, the particle transport equation can be written in a short form, by using the functional $F[J]$, that describes the secondary particles that are produced through interactions in V , by assuming that there are no interactions between the different particle types.

$$\frac{dJ(\Gamma)}{d\Gamma} = F[J(\Gamma)] + K \cdot J(\Gamma) \quad F[J] = \int_{\Gamma} d\Gamma \mu(\vec{r}, E' \rightarrow E, \vec{\Omega}' \rightarrow \vec{\Omega}) \cdot J \quad (2.17)$$

μ is the total cross section and $K \cdot J(\Gamma)$ describes the primary particles. Because of the derivation $\frac{dJ(\Gamma)}{d\Gamma}$ Equation (2.17) is not numerical stable. Therefore, it is rewritten in an integral form, whereby $S(\Gamma)$ describes the particle source.

$$J(\Gamma) = \int_{\Gamma} d\Gamma J(\Gamma) + S(J) \quad (2.18)$$

This is a seven dimensional integral and in general, only numerically solvable. At those dimensions, numerical stochastic procedures are in the ascendancy compared to numerical deterministic procedures, when considering the computation time. One stochastic method, which is widely used in particle physics and which is considered as the gold standard for dose calculations in radiation therapy, is the so-called Monte-Carlo (MC) method.

2.2.3 The Monte-Carlo Method

The basic idea of using the Monte-Carlo method in proton therapy is to use the stochastic nature of the particle interactions to map $D(x, y, z)$ more precisely [2]. One basic assumption is, that the microscopic particle cross sections can be determined with higher accuracy, than the macroscopic

particle flow density and dose distribution. This goes back to the difficulty in predicting, analytically or by using deterministic algorithms, the MCS of the protons and their fluence loss.

The Monte-Carlo method is a procedure coming from the stochastic theory. Based on a large amount of similar random experiments it is used to solve analytically not (or at least at high effort) solvable problems. When using the Monte-Carlo technique as a computational tool, the random experiments are performed in the computer by generating pseudo-random numbers. It is called pseudo-random, because those numbers just appear to be random but in reality they are calculated by a deterministic algorithm. For every starting value, also called seed, the algorithm generates the same numerical sequence. Therefore it is important to change the seed for every simulation to avoid any correlations. Often those pseudo-random numbers are generated periodically, which means that after a certain amount of generated numbers, the value of the number will repeat. As one uses the Monte-Carlo technique to map random nature processes, the quality of the pseudo-random number generator defines the accuracy of the simulated output. The pseudo-random numbers are sampled from known probability distributions. Those probability distributions are the physical input in this purely mathematical technique. In radiation therapy the probability distributions are the differential cross sections of the particles in matter. The dose D , as illustrated in Equation (2.14), can be interpreted as the expectation $E(D_i)$ of N sampled doses D_i , whereby J has to be interpreted as a probability density function (PDF). Each D_i corresponds to a certain particle trajectory. If N is large enough $E(D_i)$ will converge to D , according to the law of large numbers.

$$E(D_i) = D = \int_{\Gamma} J(\Gamma)g(\Gamma)d\Gamma \quad (2.19)$$

It can be shown, that statistical uncertainty σ is proportionate to one over the root of N . $[\Gamma]$ represents the phase space integration interval.

$$D = \sum_{i=1}^N D_i + [\Gamma] \cdot \sigma \quad \sigma \propto \frac{1}{\sqrt{N}} \quad (2.20)$$

A reduction of the statistical uncertainty of a Monte Carlo simulation by the factor 2 requires an increase of N by the factor 4. An important assumption for the derivation of the particle transport equation is the absence of any co-interactions between the particles. This assumption is accurate, because the protons mainly screened from each other by the target electrons. In principle each proton in a MC simulation can be simulated at a different central-processing-unit (CPU). This high parallelization would not be possible, if the proton would co-interact. Co-interactions would massively increase the simulation time.

2.2.4 Therapeutic Dose Distribution of Protons

There are different clinical volume definitions in radiation therapy. The gross tumor volume (GTV) defines the macroscopic tumor volume that is visualized through a diagnostic technique. The clinical target volume (CTV) is a connected region, which contains, next to the tumor volume, regions where proliferative tumor cells are expected. The planning target volume (PTV) includes certain safety margins, which are coming from range uncertainties. Range uncertainties can be caused by organ

motions or by uncertainties in the reproduction of the patient positioning in the fractional radiation therapy. The treated volume (TV), which is surrounded by an iso surface, defines an area, in which the deposited dose is expected to be sufficient to reach the treatment goal. The irradiated volume (IV), denotes the healthy tissue volume, which irradiated unwantedly as a side product of the tumor treatment. One has to notice, that the additional margin around the CTV, the PTV, depends on the irradiated organ, the quality of the reproduction of the patient positioning and the geometrical uncertainties of the treatment field.

The physical dose distribution D has to be superimposed and formed in depth and laterally to ensure a homogenous dose distribution in the TV. There are two techniques, which are used in proton therapy, to full-fill this task: the passive scattering (PS) and the pencil beam scanning (PBS) [16]. PS is a delivery technique, in which scattering and range- shifting materials spread the proton beam from a lateral spread of only a few millimeters to cancer sizes which can exceed 20 cm [11, p. 2172]. In PBS, magnets deflect and steer the proton beam. Under computer control, the beam "paints" the treatment volume, voxel by voxel, in successive layers. In passive scattering the scattering components ensure a homogenous lateral beam profile of the physical dose for every selected beam energy. The dependency of the lateral homogeneity on the beam depth modulation is minimized. Therefore, one can reduce the construction of a therapeutic proton dose distribution out of physical proton dose distributions, to one dimension. The clinical dose distribution is also called spread-out Bragg peak (SOBP), because the superposition of different Bragg curves can be understood as a spreading of the Bragg peak.

$$D_{\text{therapeutic}}(z) = D_{\text{SOBP}}(z) = \sum_{i=1}^N w_i D_i(z) \quad (2.21)$$

Because there is no general analytical expression of a Bragg curve $D_i(z)$, the weight-function $W(R)$, that describes the distribution of the weights w_i over the beam range R cannot be derived straight forward, for a given target volume. The authors in Ref. [17] and [18] derived an analytic expression of $W(R)$ and $D_{\text{SOBP}}(z)$, based on an analytic expression of the Bragg curve [14], which can be used as first approximation. d_a and d_b describe the left and the right edge of the plateau region of the therapeutic dose distribution.

$$W(R) = \begin{cases} \rho D_0 \frac{p \sin(\pi/p) \alpha^{1/p}}{\pi (d_b - R)^{1/p}} & \text{for } d_a \leq R < d_b \\ 0 & \text{for } R < d_a, R > d_b \end{cases} \quad (2.22)$$

$W(R)$ can be derived using Geiger's rule: $R = \alpha E_0^p$ ($\alpha \approx 1.9 \cdot 10^{-3}$ for protons in water, $p \approx 1.8$ for protons with energies between 10 and 200 MeV) and a simplified analytical form of the Bragg curve D_{BP} without range straggling [14].

$$R - d = \alpha E^p(d) \quad D_{\text{BP}} = \rho^{-1} \frac{dE}{dd} = \frac{1}{\rho \alpha^{1/p} (R - d)^{1/1/p}} \quad (2.23)$$

$D_{\text{SOBP}}(z)$ can be written using the Heaviside-function H , whereby the curve profile is flat in the

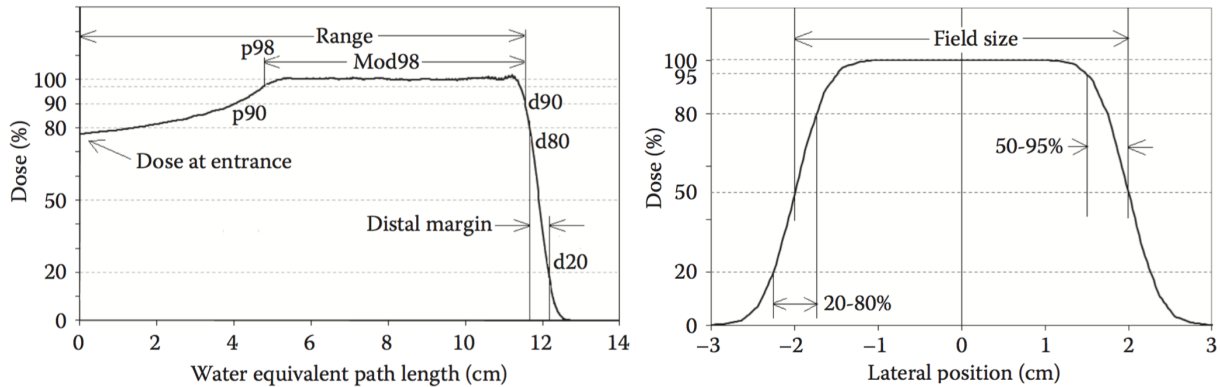


Figure 2.6: Illustration of certain clinical notations, that are used to characterize the depth-dose profile (left sub-plot) and the lateral profile (right sub-plot) of a therapeutic dose distribution (SOBP) [11].

depth interval $[d, d_b]$.

$$D_0 H(d_b - d) = \int_d^{d_b} W(R) D_{BP}(d, R) dR \quad (2.24)$$

By replacing D_{BP} with equation (2.23) one can derive $W(R)$ analytically using Laplace transformation. The analytical expression of $W(R)$ gives a first hint about the absolute SOBP weight distribution and could be discretized to get the absolute weight numbers for every Bragg curve D_{BP} . Nevertheless, as there are no range straggling effects included the accuracy of those weights is limited. A more general approach is to use numerical optimization algorithms. To optimally map the lateral shape of the three dimensional SOBP distribution (SOBP field) there are geometries that block or degrade the beam time dependent. The influence of those components can be summarized in a function $f_i(x, y)$. $f_i(x, y)$ changes slightly for every proton beam, because the beam blocking and range-shifting depend on the beam energy. The full therapeutic beam dose distribution of a passively scattered proton beam can be expressed by:

$$D_{\text{therapeutic}}(x, y, z) = \sum_{i=1}^N f_i(x, y) w_i D_i(x, y, z) \quad (2.25)$$

Equation (2.25) is valid for pencil beam scanning, too. In PBS $f_i(x, y)$ describes the influence of the magnetic fields. The calculation of the optimal beam energies and beam intensity weights is more complex. There are some important SOBP notations used in proton therapy, which are illustrated in Figure 2.6. The range R of a SOBP is defined as the material depth at 90% dose. The modulation M can be defined as the distance between the depth positions $M_{98} = R_{98} - p_{98}$, $M_{95} = R_{95} - p_{95}$ or $M_{90} = R_{90} - p_{90}$. By convention IBA (Ion Beam Applications) uses the M_{95} modulation definition. For measured dose distributions at UPTD the M_{90} convention is used. For the description of lateral profiles in clinics a so-called field size $W_{50} = r_{50, \text{right}} - r_{50, \text{left}}$ and lateral penumbras, for the left ($P_{\text{left}} = r_{80, \text{left}} - r_{20, \text{left}}$) and the right ($P_{\text{right}} = r_{80, \text{right}} - r_{20, \text{right}}$) lateral profile flank, are defined. $r_{20, \text{left, right}}$, $r_{50, \text{left, right}}$ and $r_{80, \text{left, right}}$ are defined as the lateral positions, which correspond to 20, 50, 80% of the maximum of the left and the right profile flanks, when the profiles are normalized

to the central lateral plateau region.

2.2.5 Aspects of Proton Radiobiology

Protons damage the tumor directly, through the ionization of cell molecules and indirectly through the production of chemicals, like free radicals, which disrupt cell functions. Ionized bio-molecules could disrupt cell functions, too. The most important target in proton therapy is the deoxyribonucleic acid (DNA) macromolecule. Protons induce single (SSB) and double strand breaks (DSB), whereby the latter are more difficult to repair. If two SSB (and also DSB) are close to each other, they get even harder to repair. The dependency of the (tumor) cell survival on the microscopic distribution of DSB and SSB is the reason, why sparsely ionizing ion radiation (high LET) induce a higher biological cell damage compared to the lose ionizing photon irradiation (low LET). Because the proliferation rates of tumor cells are much higher, compared to those of healthy tissue cells, a genetic damage can propagate much faster. The lack in nutrients supply of tumors mitigates cell repair mechanisms. The quality of the cell repair mechanisms can vary within the tumor tissue, as it depends on cell type, cell cycle state, the nutrients supply and the cell environment. A tumor can contain a large number of different cells. Because a tumor has a very active metabolism, it is able to accumulate cells from different regions of the body. Similar to the concept of dose or stopping power, one can sum up all statistical biological damages to a macroscopic parameter, the biological damage \mathcal{E} . One has to have in mind, that not only the energy deposition is a stochastic process, but also the reaction of the complex system cell. The biological effect that is induced by a certain amount of protons could be defined as the surviving fraction S_{frac} of tumor cells γ_{cell} , after a certain amount of time t .

$$\mathcal{E} = \mathcal{E}_{\text{Physics}} + \mathcal{E}_{\text{Chemistry}} + \mathcal{E}_{\text{Biology}} \quad (2.26)$$

$\mathcal{E}_{\text{Physics}}$ = DNA damage distribution, free energy of the DNA polymer,...

$\mathcal{E}_{\text{Chemistry}}$ = Distribution of free radicals,...

$\mathcal{E}_{\text{Biology}}$ = Cell type, cell state, cell environment, organ environment, ...

As \mathcal{E} is a function of time t one needs to choose a representative time interval t_{rep} , that contains the most important adverse effects, that can occur in proton therapy. There are adverse effects that can occur a couple of years after the irradiation. Nevertheless, it gets more and more difficult to relate a certain adverse effect, that arises a couple of years after the irradiation to a radiation damage straight after the patient treatment. One can model the biological effect as the negative natural logarithm of the tumor cell surviving fractions S_{frac} after the a certain biological endpoint time.

$$\mathcal{E} = -\ln(S_{\text{frac}}) \quad S_{\text{frac}} = \frac{N}{N_0} \quad (2.27)$$

N_0 is the initial number of cells and N is the number of unaffected cells in the tumor. In principle, the best treatment plan would not maximize the dose homogeneity in the target volume (TV), but maximize the biological effect \mathcal{E} . Nevertheless, until now the biological effect of photons and ions is not completely understood. Therefore, clinical data and data coming form cell and pre-clinical experiments, play an important role to study the dependency of \mathcal{E} on a macroscopic measurable physical parameter, the dose D . Therefore, one develops $\mathcal{E}(D)$ in by a Taylor series in D . It turns

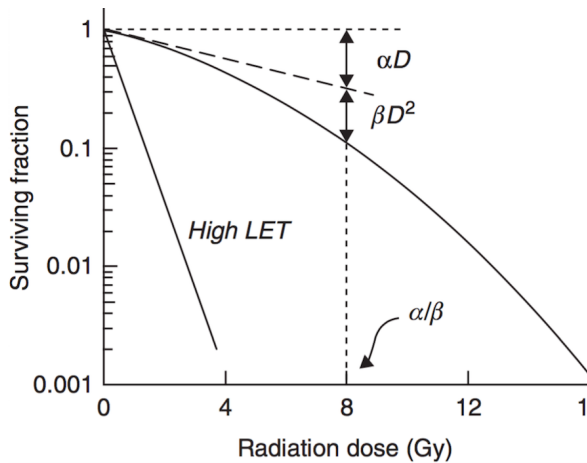


Figure 2.7: Illustration of the LQ-model [19].

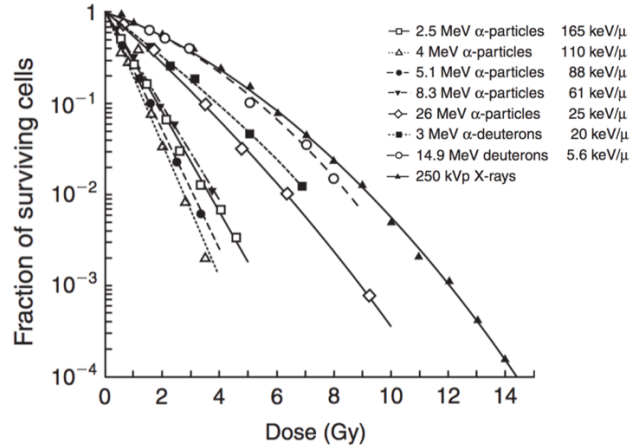


Figure 2.8: Survival of human kidney cells exposed in vitro to radiations of different LET. From Barendsen (1968) [19].

out, that a majority of measurements can be well described by the linear (D) and the quadratic (D^2) term.

$$\mathcal{E}(D) = \sum_{n=0}^{\infty} \lambda_n D^n \approx \lambda_1 D + \lambda_2 D^2 = \alpha D + \beta D^2 \quad (2.28)$$

$$S_{\text{frac}} = e^{-(\alpha D + \beta D^2)} \quad (2.29)$$

This relationship is also called linear-quadratic model (LQ-model). The linear coefficient is called α , the quadratic one is called β . The LQ-model can be used to fit experimental data. The coefficients contain the biological information of the system and are tabulated for different cell types and compositions. α and β are strongly related to the cell repair mechanisms, and vary for different cell types, cell cycles and cell environments. Next to the biological information, measurements illustrated that α and β depends on radiation type, and therefore on the microscopic structure of the energy deposition. Figure 2.7 illustrates a scheme of the LQ-model. In Figure 2.8, cell survival curves of human kidney cells are shown, which were exposed in vitro to radiation with different LET. The LQ-model can be motivated due analytical models that were developed in the so-called target theory [19, p.47], [20]. The multi-hit-model and the multi-target-model are two assumptions (which can be combined), which map the statistical nature of the energy deposition precisely, but simplify the mapping of the biological processes. Therefore, those models have only a heuristically benefit for the interpretation of measurements. There are alternatives to the LQ-model, which, for example, include the dynamics of cell repair (LPL-model [21]).

The LET adds an additional information about the local distribution of the energy deposition of a certain radiation type. The observed dependency of \mathcal{E} on LET illustrates that besides the overall macroscopic energy deposition the microscopic track structure plays a role for modeling the biological radiation damage. Densely-ionizing ion radiation induces more pronounced biological cell damage than sparsely ionizing photon radiation. If one compares a carbon (C^{6+}) Bragg curve with a proton Bragg curve with similar range and integral dose, there is a lot more ionization around one carbon track compared to a proton track because the stopping power is proportionate to the square of the

proton number z^2 of the projectile particle ((2.1)). Because the velocity of the carbon ion and the proton is comparable (under this conditions), the maximum energy and therefore the maximum range, that can be transferred to an electron is similar. A carbon track produces SSB and DSB, which are closer compared to a proton track and dense DNA strand breaks are more difficult to repair.

There is a large amount of clinical data for photon therapy. Those data contain information about long- and short term adverse effects. In clinics, one defines adverse effects that occur until three months after the irradiation as short term adverse effects, and adverse effects that occur after three months as long term adverse effects. Therefore, one can define the biological effect from a clinical point of view, as the amount of dose, that is necessary to maximize the tumor control T by minimizing the short term, A_{short} , and the long term adverse effects, A_{long} . The physician has to decide how to weight those three terms, based on his empirical knowledge and statistical analyses.

$$\min|\lambda_1 A_{\text{short}}(D) + \lambda_2 A_{\text{long}}(D) - \lambda_3 T(D)| \rightarrow D_{\text{opti}} \quad (2.30)$$

$$\mathcal{E}_{\text{clinical}} = D_{\text{opti}} \quad (2.31)$$

Because of the complexity of the radiobiological processes, one could neither derive $\mathcal{E}_{\text{clinical}}(\text{Photons})$ from first principles of physical energy deposition E_{physics} , nor $\mathcal{E}_{\text{clinical}}(\text{Protons})$. One main goal of the research in radio therapy is to better understand the relationship between $\mathcal{E}_{\text{clinical}}$ and E_{physics} . Because of the lack of understanding, one relates the ion therapy on the clinically much better analyzed photon therapy. The concept, which is used in clinics is the so-called relative biological effectiveness (RBE). The RBE of protons is defined as the dose of a reference radiation, D_x , divided by the proton dose, D_p , to achieve the same biological effect after a certain endpoint time t_{end} . The reference radiation is the photon radiation (D_γ).

$$\text{RBE}(t_{\text{end}}) = \frac{D_x}{D_p} = \frac{D_\gamma}{D_p} \quad (2.32)$$

Based on clinical data the RBE of protons is assumed to be 1.1 (constant). To apply a constant proton RBE of 1.1 has the advantage, that the conversion of photon dose into proton dose for clinical trials is straightforward. Furthermore, clinical dosimetry is based on homogeneous dose distributions in the target. [11, p.600]. Nevertheless, when applying a constant RBE one assumes, that the biological effect $\mathcal{E}(D, \text{LET})$ of protons and photons is similar. Recent research suggests the assumption, that there are deviations between $\mathcal{E}(D, \text{LET})$ of protons and photons up to 50%, particularly at the distal edges of the treatment fields. In those regions the mean velocity of the protons is low and therefore the LET, whereby the proton fluence is still sufficiently high, and therefore the dose. This suggest the usage of a RBE, that varies with the dose D . Figure 2.9 illustrates measured in vitro and in vivo data of proton RBE values [11, p.601]. From a clinical point of view one could argue, that no adverse effects could so far be definitively related to an underestimation of the proton RBE. Therefore there is no clinical necessity to assume the RBE to be variable. A variable RBE would increase the complexity of the treatment planning. Nevertheless, the absence of systematic adverse effects could also be related to the safety margins, that are related to range uncertainties and uncertainties in the patient positioning. Due those margins a systematic RBE underestimation could be washed out. A further reduction of range uncertainties in proton therapy, for instance due to Monte-Carlo simulations

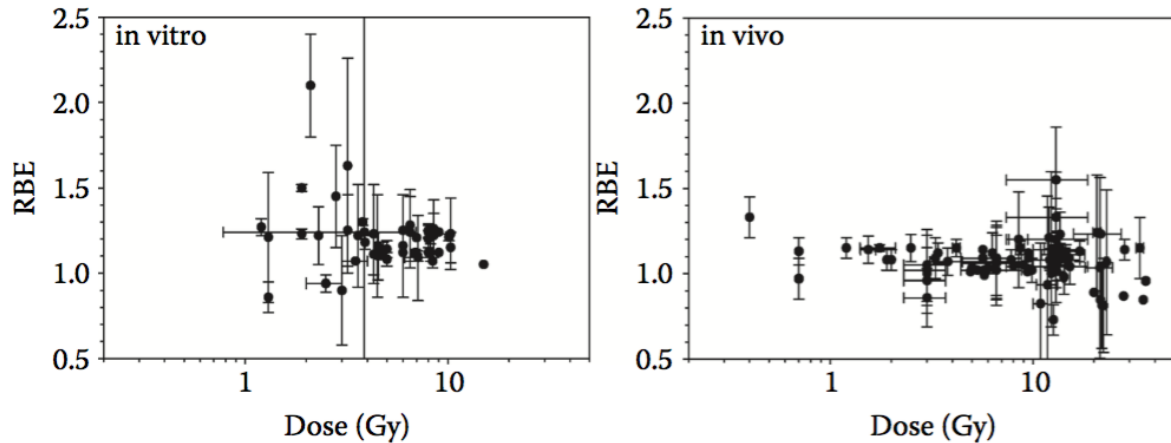


Figure 2.9: Measured proton RBE values (relative to ^{60}C) as a function of doses/fraction for cell inactivation measured *in vitro* (left) and *in vivo* (right) [11, p.601].

or direct measurements, could increase the importance of applying variable RBE models. In addition, there are patients, that show adverse effects at treatment field edges. Those effects can be related to a RBE underestimation, but however this has to be proven statistically. A variable RBE model for proton therapy could be derived straight forward using the LQ-model. By definition, the biological effect that is reached by applying the proton dose D_p should be the same as caused by the reference dose D_x .

$$\mathcal{E}(D_x) = \mathcal{E}(D_p) \rightarrow \text{RBE}(D_p, \alpha_x, \beta_x, \alpha_p, \beta_p) = \frac{\sqrt{\alpha_x^2 + 4\beta_x D_p(\alpha_p + \beta_p D_p)} - \alpha_x}{2\beta_x D_p} \quad (2.33)$$

The LET dependency can be included in equation (2.33) by assuming a linear relationship of α on LET ([22–26]). At those model the β parameter is assumed to be not a function of the LET.

2.3 Passive Scattering in Proton Therapy

Passive scattering (PS) is a delivery technique in which scattering and range-shifting materials spread the proton beam from a lateral spread of only a few millimeters to cancer sizes which can exceed 20 cm [11, p. 2172]. Compared to PBS, PS is less complex, when it comes to planning, computation, and equipment and the risk of target misses due to organ motion. For now it is considered as being more robust as PBS, particularly, when it comes to the treatment of moving organs.

2.3.1 Beam Adaption Techniques

A central part of a passive scattering nozzle is the scattering system. In principle one could use one scattering foil to spread the beam to a Gaussian shaped lateral profile. The standard deviation $\sigma_{x|y}$ of the Gaussian increases with the distance from the scattering foil, because of the mean scattering angle Θ_0 (Sub-section 2.1.2). By slicing out a central part of the Gaussian, using collimator material, one could obtain a homogenous lateral profile in first approximation. Nevertheless, this technique is

very inefficient and therefore cost-intensive. As larger the amount of protons, that has to be blocked, as larger the activation of the material and the number of produced neutron particles. By adding a second scatterer, one could increase the nozzle efficiency and decrease the nozzle size, and still obtain the same homogenous lateral profile as in the single scattering mode. Scattering systems, which contain two scatterers, are called double scattering systems. Depending on the lateral distance from the beam center, the second scatterer scatters the protons differently. Protons close to the beam center discover a high angle shift, protons with large distances from the beam center discovers a small angle shift. There are different double-scattering techniques, with different complexity [11, p. 127], [27]. One of the most efficient and accurate ones, is the one that is using a so-called contoured scatterer (CS). A CS is a component with an optimized thickness $d(x,y)$ distribution [28]. Figure 2.10 illustrates the function of a single scattering system using a flat scatterer, and of a double-scattering system using a contoured scatterer. When assuming Gaussian scattering the fluence distribution can

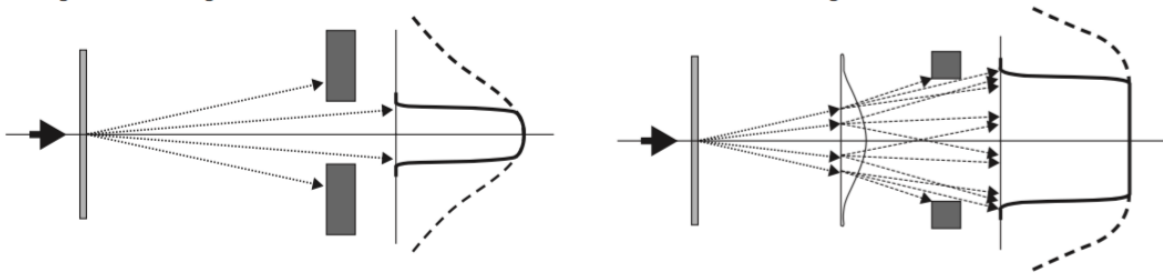


Figure 2.10: Scheme of a scattering systems using a single flat scatterer (left) and a double scattering system with a contoured scatterer (right) [11, p. 127].

be written analytically.

$$\phi_{\text{FS}}(r)dr = \frac{1}{\pi z_{\text{FS}} \Theta_{\text{FS}}} \exp\left[-\frac{r^2}{(z_{\text{FS}} \Theta_{\text{FS}})^2}\right] dr \quad (2.34)$$

z_{FS} is the distance of the first scatterer FS from the plane of interest, that contains the iso-center and is parallel to the FS. The iso-center is the position in depth, where the lateral beam profile should have the largest homogeneity. r defines the lateral distance from the beam center. Θ_{FS} is the characteristic angle of the FS, which can be approximated by Highland's formula (Sub-section 2.1.2). By adding the contoured scatterer to the system one has to fold $\phi_{\text{FS}}(\vec{r})$ with $\phi_{\text{SS}}(\vec{r})$, the fluence distribution of the second scatterer.

$$\Phi(\vec{r}) = \int \phi_{\text{FS}}(\vec{r}') \phi_{\text{SS}}(\vec{r} - \vec{r}') d\vec{r}' \quad (2.35)$$

By assuming rotational symmetry, thin scatterers and a small parallel entrance beam one can rewrite $\Phi(\vec{r})$ [11, p. 128].

$$\Phi(r) = \frac{1}{(2\pi z_{\text{FS}} \Theta_{\text{FS}})} \int_0^{2\pi} d\Phi \int_0^R \underbrace{\vec{r}' d\vec{r}' \cdot \exp\left[-\frac{r'^2}{(z_{\text{FS}} \Theta_{\text{FS}})^2}\right]}_{(i)} \cdot \underbrace{\frac{1}{(z_{\text{CS}} \Theta_{\text{CS}}(r'))^2} \cdot \exp\left[-\frac{(\vec{r} - \vec{r}')^2}{(z_{\text{CS}} \Theta_{\text{CS}}(r'))^2}\right]}_{(ii)} \quad (2.36)$$

z_{CS} is the distance from the second scatterer to the plane of interest, Θ_{CS} is the characteristic scattering angle of the contoured scatterer, that depends on radial position \vec{r}' . R is the radius of the contoured scatterer assuming all protons outside R are blocked. The radial coordinates \vec{r}' and R of the contoured scatterer are projected from the first scatterer onto the plane of interest. The first exponential term (i) describes the fluence of the beam hitting the contoured scatterer at position \vec{r}' . The second exponential term (ii) describes the contoured scatterer, which means the proportion of protons hitting the second scatterer at position \vec{r}' and ending up at position \vec{r} . This depends on the distance between \vec{r}' and \vec{r} and the angular spread of the contoured scatterer. Simplifications in this formula are: Gaussian scattering, rotational symmetry, thin scatterers and a small parallel entrance beam [11, p. 128]. Depending on the lateral position the CS material shifts the beam range differently. To achieve a similar range-shift for the full CS component, the CS is energy compensated by a low-Z material. Besides the first and second scatterer, in passive scattering one uses the air between the component and the range-shifting material as an additional scatterer.

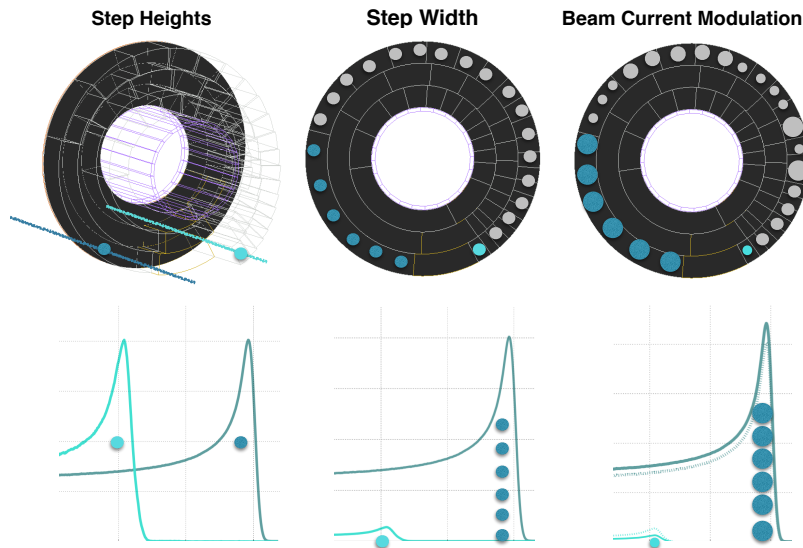


Figure 2.11: Principle of operation of a RMW including beam current modulation (BCM). The track step heights modulate the BP ranges and the step angular spreads modulate the BP weights. BCM can be used to further tune the weights in order to generate flat SOBP distributions. The RMW geometry is implemented using the Monte-Carlo tool TOPAS.

The range-shifting material is placed on a component, called range modulation wheel (RMW). A RMW contains different track steps, whereby the amount of material changes for every track step. The RMW rotates with a constant velocity (a couple of Hz) during a irradiation and the beam obtains time-dependently a different range-shift. The number of different range-shifts is determined by the number of track steps. The amount of the range shift is determined by the thickness of the steps. Each track step correspond to one Bragg peak. The integral weight of each Bragg peak is determined by the amount of protons, that are traversing one step and therefore on the angle step width. The geometry of a RMW is optimized to generate SOBPs with flat plateaus. As the stopping of a proton beam depends on the beam energy, the track perform well only within a certain energy interval. To produce flat SOBPs over the full therapeutic energy regime, several wheels are used, whereby each wheel contains various tracks. Each tracks step has a different thickness and therefore scatters the beam differently. To achieve a similar scattering performance within one track, every track is scattering compensated by a high- Z material. In principle each beam energy requires an own optimized RMW track, because the size of the weights of the single Bragg curves depends on the initial beam energy. Nevertheless, it is possible to fine-tune the weights by adjusting the beam current separately for every track step. This technique is called beam current modulation (BCM). Figure 2.11 illustrates the geometry and principle of operation of a RMW wheel, that contains three different tracks, and the principle of operation of the beam current modulation technique.

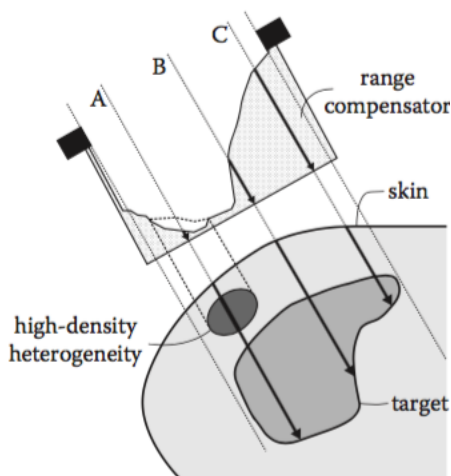


Figure 2.12: Scheme of the principle of operation of a compensator as used in PS [11].

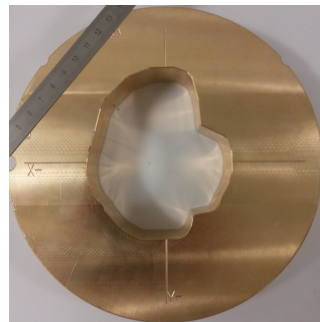


Figure 2.13: A brass aperture as used for one patient treatment field at UPTD. The figure is kindly provided by Hakan Östen [29]

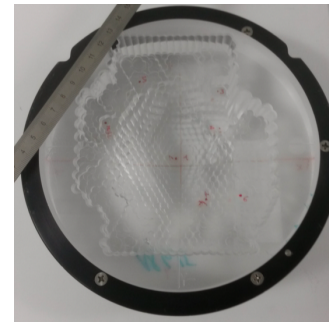


Figure 2.14: A lexan compensator as used for one patient treatment field at UPTD. The figure is kindly provided by Hakan Östen [29]

So far the introduced beam adaption techniques generate homogeneous dose distributions with cylindrical shape. To further adjust the dose distribution $D_{\text{SOBP}}(x,y,z)$ to the target volume $V(x,y,z)$ one applies a tumor specific collimation of the lateral field distribution $f_{\text{AP}}(x,y)$ and a specif range-shift $f_{\text{CP}}(x,y)$, depending on the lateral beam position. The patient specific collimation is done by a component called aperture (AP). For the patient specific range-shifting a so-called compensator is used.

For each patient treatment field a specific aperture and compensator (CP) have to be produced.

$$D_{\text{Patient}}(x,y,z) = f_{\text{AP}}(x,y) \cdot f_{\text{CP}}(x,y) \cdot D_{\text{SOBP}}(x,y,z) \quad (2.37)$$

An aperture is a collimator (high- Z material) with a hole, that covers the lateral extension of the target volume. A compensator is a block (low- Z material), which contains different drill holes. Depending on its distance to the beam center a proton has to traverse a different amount of CP material. Figure 2.12 illustrates the function of a compensator. One has to keep in mind, that in PS one can only adjust the distal field edge. The proximal edge cannot further be adjusted. Figure 2.13 and Figure 2.14 show a photograph of an aperture and a compensator as used at UPTD for one patient treatment field. The AP and CP are placed in a component called snout. The snout can be moved forward and backwards to the patient and has the function to minimize the snout position d_{pos} . The snout position is defined as the distance between the outer surface of the aperture, which is close to the patient. To the isocenter. The isocenter is defined in the treatment planing. It could be for example the geometrical or mass barycenter of the target volume. A PS nozzle usually includes an ion chamber for beam control measurements and the calculation of the so-called output factors. So-called jaws are used to minimize the irradiation of the patient due secondary particles. The jaws are two collimator, which can be shifted in x - and y - direction. A schematic of a PS nozzle is illustrated in Figure 2.15. There is

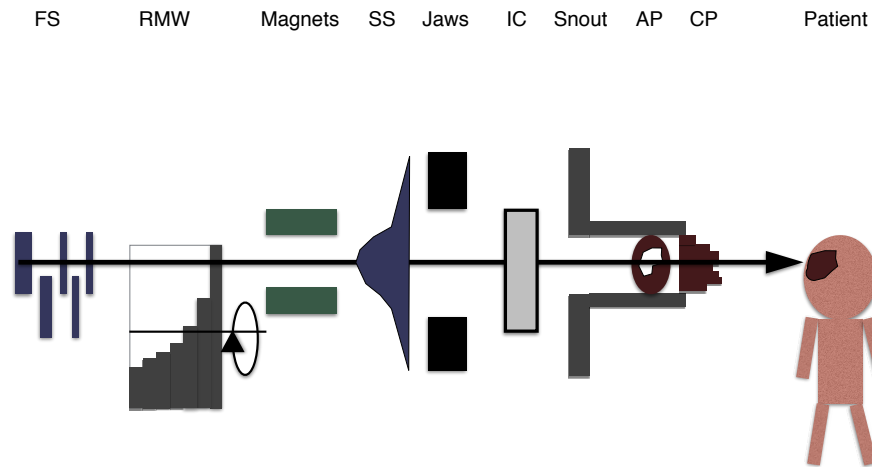


Figure 2.15: Schematic, not to scale of a passive scattering nozzle (IBA universal nozzle in double-scattering mode, UPTS), including first scatterer foils (FS), a range modulation wheel (RMW), magnets (not used in double scattering), a contoured second scatterer (SS), collimator Jaws, an ion chamber (IC), a snout, an aperture (AP) and a compensator (CP).

not one best solution, how to design a nozzle. It is a compromise between certain constrains. One can define the target function $f(\lambda_i)$, that describes the dependency of the SOBP field homogeneity on a set of parameters λ_i . λ_i represent basically the positions, thickness and material compositions of all geometries. By minimizing $f(\lambda_i)$ under certain constrains t_i , one would get the optimal values $\lambda_{\text{opt}i}$,

that leads to the most homogeneous lateral SOBPs profile in the isocenter.

$$|f(\lambda_i)| \rightarrow \min \quad \lambda_i = \text{positions, thicknesses, materials of all geometries}$$

$t_1 = \text{constrain 1: tolerance limit for lateral inhomogeneities}$
 $t_2 = \text{constrain 2: maximum required field size}$
 $t_3 = \text{constrain 3: tolerance limit for overall scattering angle}$
 $t_4 = \text{constrain 4: financial limit for material costs}$
 $t_5 = \text{constrain 5: high nozzle efficiency}$
 ...

2.3.2 Output Factors

A treatment planning system (TPS) for PS in proton therapy derives its beam model, by fitting measurement data. Therefore it uses implemented interpolation and extrapolation algorithms. Those algorithms can be motivated by physical laws or are based on mathematically sophisticated fitting routines. Depending on the amount and accuracy of the measurement data those fitting routines are able to predict the three dimensional dose profile $D(x,y,z)$ with high accuracy. A nozzle in double scattering mode usually delivers the beam in different options, whereby the options differ in the usage of geometries and/or beam current modulation. To cover all these options a large number of reference measurements has to be performed and put in the TPS. The points between the measured values are interpolated. The current TPS software, which is used in PS, is able to predict the spatial relative dose distribution within clinical tolerances. The prediction of the absolute dose within the clinical tolerance of 1% is not provided. This is related to uncertainties in the physical modeling of the absolute dose, which depends on a large amount of independent nozzle parameters.

To understand the unique field properties of every patient field, the beam profile has to be measured at characteristic points, which allow conclusions about the change in absolute dose. One measurement is usually performed in an ion chamber (IC), which is placed inside the nozzle. A second measurement is performed in the high-dose region of a SOBPs field in water phantom, when no compensator is used. A compensator is usually excluded, because it generates inhomogeneous dose profiles in the water phantom and therefore it is difficult to define characteristic field points. Both, the measurement in the IC and in the water phantom are performed in the so-called patient QA measurements for every patient treatment field. The ion chamber is filled with a gas (e.g. air.), with a known density. The dose inside the chamber is measured, by collecting secondary ions and electrons, which are produced due to electromagnetic or nuclear interactions of the protons with the gas molecules. If the active measurement volume in the IC is small enough, one can assume the proton stopping power to be constant. As the gas density stays approximately constant, too, the IC charge signal is proportionate to the beam dose. In clinics one normalizes the IC signal to a reference field and defines a so-called monitor unit (MU). 100 MU are the collected charge in the IC, which is required to achieve a total dose distribution of 2 Gy in the water phantom, for the specific settings of a reference treatment field. For a certain treatment it is helpful to summarize the measured signal in the IC ($x[\text{MU}]$) and the measured dose ($D_{\text{SOBPs}}/\text{cGy}$) in the water phantom to one value, the so-called output factor (OF). A

OF is defined as the ratio between D_{SOBP} and the MU signal in the IC.

$$\psi = \frac{D_{\text{SOBP}}}{\text{MU}} \quad (2.38)$$

The output factor represents a recalibration of the ion chamber in the nozzle. This recalibration has to be performed for each treatment field, because for each treatment field the aperture and the nozzle settings do change and therefore the ratio between the dose measurement in the water phantom and the MU signal in the ion chamber.

By using the measured OF values, one is able to predict the MU number, which is necessary to achieve the prescribed absolute dose in the patient. Therefore one has to assume, that the size output factor of the OF is not affected by the compensator.

$$\psi_{\text{QA}} = \psi_{\text{Patient}} \rightarrow \text{MU}_{\text{Patient}} = \frac{D_{\text{TPS}}}{\psi_{\text{QA}}} = \text{MU}_{\text{QA}} \cdot \frac{D_{\text{SOBP}}}{D_{\text{TPS}}} \quad (2.39)$$

If a treatment field contains N beams the beam weights can be derived straight forward using the $\text{MU}_{\text{Patient}}$:

$$D_N = \sum_{i=0}^N w_i D_i \quad w_i = \frac{\text{MU}_i(\text{Patient})}{\sum_{i=0}^N \text{MU}_i(\text{Patient})} \quad (2.40)$$

Predicting the output factors due a theoretical model and/or due simulations would have a large clinical and financial benefit, because one could reduce the measurement effort per patient. A theoretical model of the output factor has to include different dependencies. First, ψ is a function of the SOBP range R and the SOBP modulation M . If the ion chamber is at a nozzle position close to the patient and if the measurement volumes in the IC and the water phantom are close to the central beam axis, one can assume, that the IC signal x_{MU} is proportionate to the SOBP entrance dose D_0 [30]. The dose D_{SOBP} , which is measured in the water phantom, corresponds to the plateau dose D_p . D_p do not change within the plateau region. ψ can be approximated by the ratio between D_p and D_0 .

$$x_{\text{MU}} \propto D_0 \rightarrow \psi \propto \frac{D_p}{D_0} \quad (2.41)$$

D_p/D_0 can be approximated analytically [17], whereby z is defined as the depth in the water phantom.

$$\frac{D_p}{D_0(R, M)} \approx \frac{1}{1 + 0.44r^{0.6}} \quad r = \frac{R - M}{M} \quad (2.42)$$

Next to R and M , ψ depend on the so-called source-to-axis distance (SAD). The SAD is define as the distance from the source to the isocenter. In the patient QA the isocenter is defined as the SOBP plateau center. The SAD dependency, can be explained by the fact, that the proton field in passive scattering contains an overall scattering angle Θ_{PS} . Because, the PS nozzle is optimized under the constrain to minimize this angle, one can apply a small angle approximation.

$$\sin(\Theta_{\text{PS}}) \approx \Theta_{\text{PS}} = \frac{X_0}{\text{SAD}} \quad (2.43)$$

X_0 is root mean square of the Gaussian proton fluence distribution on the water surface. Equation (2.43) maps the full nozzle scattering to a single scattering problem, as described in Equation (2.3). Therefore Θ_{PS} contains all the nozzle specific scattering properties. For a constant scattering angle Θ_{PS} , SAD is proportionate to X_0 . The rms X_0 spans a circular plane A_r . Therefore the proton fluence per surface element, decreases with increasing SAD.

$$\Theta_{PS} = \text{const} \rightarrow \text{SAD} \propto X_0 \quad A_X = \pi X_0^2 \quad \phi_{A_X} = \frac{\phi}{A_X} \propto \frac{1}{\text{SAD}} \quad (2.44)$$

The decrease of ϕ_{A_X} with increasing SAD, is leading to a dose decrease within the SOBP plateau, when measuring the SOBP in a volume with a constant lateral extension along the beam axis. The IC position remains at the same depth position Z_{IC} for every patient treatment. The SAD changes, because of the varying snout position. Therefore the OF depends on the SAD, whereby the SAD dependency contributes with the inverse square (Equation (2.44)). Equation (2.42) is derived by assuming a parallel beam with $\text{SAD} = \infty$ ($\Theta_{PS} = 0^\circ$). For a nominal SAD those beam would have a linearly increasing plateau. Nevertheless, it is possible to derive an analytical expression of the ratio D_p/D_0 for a SOBP with a linearly increasing plateau at infinite SAD, which would be flat at a nominal SAD value [31]. Therefore one can approximate that at infinity small SAD variations, changes ϕ_{A_X} (and therefore the dose plateau slope) only linearly. The dose can be split in a flat and a linearly rising component. The full derivation can be found in Ref. [31]. The final analytical expression of the output factor can be written as a function of $r = (R - M)M$ and two factors a_0 and a_1 . Those two factors can be determined by fitting experimental data. They contain the SAD dependency of ψ .

$$\psi(R, M) = \psi_c \cdot \frac{D_c(z = 0, R_c, M_c)}{100/(1 + a_0 \cdot r^{a_1})} \quad (2.45)$$

Beside the range, modulation and the SAD the OF depends on the field size [32]. In particular scattering effects from the aperture can impact the measured dose in the water phantom D_p . The usage of different nozzle geometries within different nozzle options adds another uncertainty to the OF prediction. Because the overall nozzle efficiency and the field angle do change within every nozzle option, it might be justified to apply option correction factors, when fitting experimental data. Back scattered protons, can slightly change the dose signal in the IC. Changing nuclear production rates (neutrons, alpha, ...) might have an influence on ψ too.

3 Materials and Methods

First, the UPTD (University Proton Therapy Dresden) specific TOPAS settings are introduced, briefly. Therefore, the implemented TOPAS physics settings, the applied beam source. This includes a description of the TOPAS model of the nozzle geometry, beam source and physics settings and a description of the TOPAS versions, which are used. Second, the procedure of the adjustment of simulated depth-dose curves (DDC) is explained. It contains the optimization of the initial beam energy distribution and the calculation of TOPAS specific beam current modulation functions. Third, the implemented TOPAS setup for the simulations of output factors is described. Fourth, the automated implementation of one proton plan (brain) in TOPAS is explained. This includes the accurate positioning of the computed tomography image in the TOPAS world and the integration of patient specific geometries.

TOPAS Software TOPAS, is a Monte-Carlo toolkit, which was developed and validated specifically for applications in proton therapy [7, 33]. Its core is GEANT4 [34, 35], which is one of the most wide spread Monte-Carlo tools used in particle physics. The TOPAS default physical settings define specific parameters of the underlying GEANT4 software, which are leading to an accurate mapping of the physical processes, which are most relevant for applications in proton therapy [36]. TOPAS itself is controlled by a parameter control system instead of plain C++. Nevertheless, TOPAS can be extended by own C++ classes. TOPAS contains pre-built geometry classes for applications in proton therapy. It allows straight forward computed tomography (CT) and computer assisted design (CAD) image integration.

TOPAS Physics and Versions In GEANT4 and TOPAS, physical processes, that are required for a certain simulation, are summarized in so-called physics lists. A physics list specifies what particles and physical processes are defined, and defines various cut-offs and model options. For accurate dose and LET simulations in proton therapy, a physics list has to contain models for all secondary particles too (neutrons, helium ions, deuterons, tritons, photons, electrons, etc.). The differential cross sections of the electromagnetic and nuclear interactions are usually based on a combination of experimental data and theoretical models, which are used to fit measurements [35]. The particle transport is described and discussed in Ref. [37, p.7-12]. Depending on the differential cross section the interaction frequency of the particles vary. For particles, which undergo a large amount of interactions, certain approximations are applied, to limit the simulation effort. For example, it is almost impossible to simulate all scattering interactions of electrons in matter in a reasonable amount of time. Therefore, a certain number of scattering events is summarized or condensed to one event, with a mean scattering angle. This technique is called condensed history technique (CHT) and can vary within different MC algorithms. Uncertainties in the tracking of electrons can lead to uncertainties in the simulated dose distributions of protons. Nevertheless, compared to the uncertainties of deterministic algorithms, when it comes to the mapping of the multiple coulomb scattering (MCS) of protons and electrons,

the CHT uncertainties are negligible. Within the progress of this master thesis, there was a TOPAS upgrade from version 2 [38] to version 3 [39]. TOPAS version 3 uses the actual GEANT4 version 10.2.p01 [34], whereby TOPAS version 2 uses GEANT4 version 10.1.p02 [40]. TOPAS 3 contains several advantages, for example an improved CT image integration. Therefore this version is used for the simulation of the proton treatment plans. The commissioning of the TOPAS nozzle model is done for TOPAS version 2. As there are some changes in the physics list between the old [37] and the new [35] GEANT4 version, the commissioning will be repeated for version 3. GEANT4 version 10.2.p01 uses for example a default I-value for water of 78 eV, whereby GEANT4 version 10.1.p02 uses 75 eV.

TOPAS Beam Source In TOPAS version 2 there is a default pre-defined beam source, which corresponds to the proton beam at the Massachusetts General Hospital (MGH) Francis H. Burr Proton Beam Therapy Center. In TOPAS version 3 there is no pre-defined beam source, to avoid any confusions. The shape of the proton beam source is strongly facility dependent. If a cyclotron accelerator is used, which delivers a proton beam, with a constant energy, the proton beam source basically depends on beam steering and filtering in the cyclotron and the so-called energy selection system (ESS). An ESS is used to shift the mean beam energy depending on the requested treatment field range, by assuring similar beam source parameters. A proton beam at a therapy energy regime can be described accurately by its mechanical phase space: its spatial, angular and energy distribution. At UPTD a cyclotron proton accelerator is used together with an ESS. The TOPAS beam source settings are defined based on measurements from the company, which designed the proton therapy system at UPTD. The company is called ion beam applications (IBA) and is still responsible for the daily service of the cyclotron accelerator including the ESS. A scheme of the proton accelerating system as used at UPTD is illustrated at Figure 3.1. The spatial, angular and energy distribution can be accurately approximated by a Gaussian, whereby the angular Gaussian is very sharp. Therefore the beam can be assumed to be parallel in first approximation. IBA optimized the ESS, to deliver beams with maximal sharp Gaussian energy (\bar{E}, σ_E) and angular ($\bar{\Theta}, \sigma_\Theta$) distributions for every requested field range. For every requested beam energy a beam is delivered, with a spatial distribution a spread σ_X , which wont exceed 5 mm, when measure in an ion chamber straight in front of the nozzle (IC1). There is no systematic dependency of σ_X , which can be observed in the IBA measurement data. Its mean value of all σ_X measurements lie around 4 mm. As there are no experimental data of the angular distribution of the proton beam at UPTD, the same distribution is assumed, which is used at MGH. This assumption is justified, because at MGH a similar IBA cyclotron and nozzle system is used. In TOPAS the spread of the energy spectrum σ_E is defined relative to the mean beam energy \bar{E} by a value called beam energy spread (BES).

$$\text{BES} = \frac{\sigma_E}{\bar{E}} \quad (3.1)$$

The nozzle in double-scattering mode is able to deliver SOBPs with ranges between 4.6 cm and 28.4 cm. This corresponds to mean energies $\bar{E} \approx [155|228]$ MeV of the beam which enters the nozzle $\bar{E} \approx [155|228]$ MeV. Those values are calculated by using PSTAR (National Institute of Standards and Technology, NIST) conversion tables [10] by considering the change in the water equivalent thickness (WET) of the nozzle. The constant mean energy of the beam, that is leaving the cyclotron is 235 MeV. The UPTD specific beam source settings in TOPAS version 3 are listed in Table 3.1. Similar source settings are used in version 2. Just, some parameters are named differently. For the spatial and

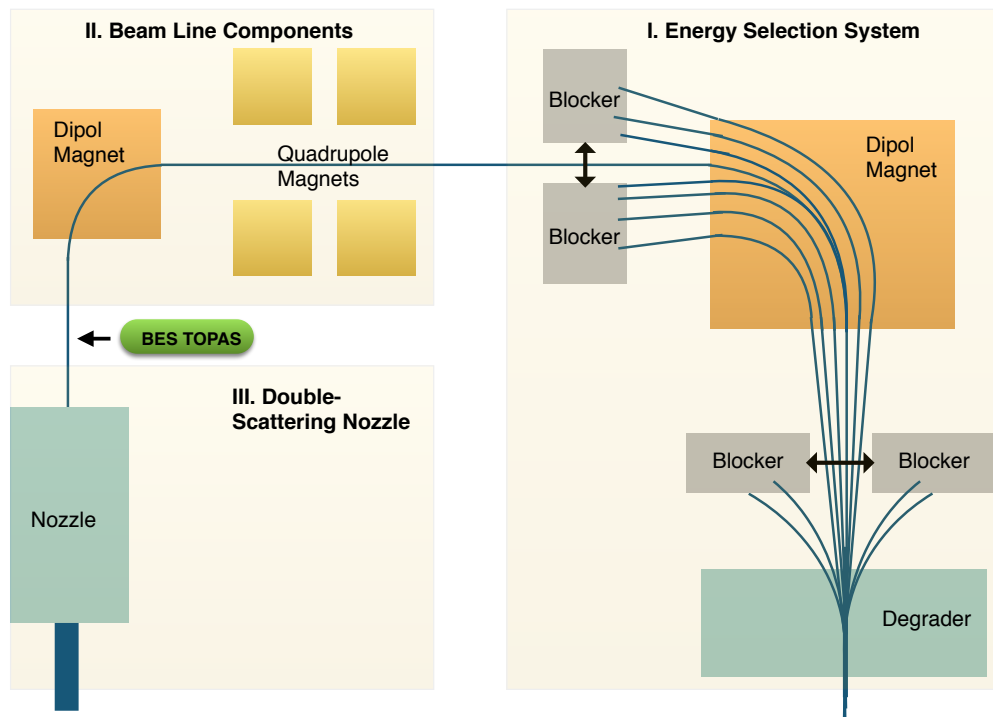


Figure 3.1: Schematic of the path, which the protons will travel after leaving the cyclotron accelerator. First, they will traverse the ESS, second they get shifted by beam line components and third they enter the IBA universal nozzle.

Table 3.1: TOPAS beam source settings at UPTD.

Spatial Distribution	s:So/DefaultDresden/BeamPositionDistribution = "Gaussian" d:So/DefaultDresden/BeamPositionSpreadX = 4 mm d:So/DefaultDresden/BeamPositionSpreadY = 4 mm s:So/DefaultDresden/BeamPositionCutoffShape = "Ellipse" d:So/DefaultDresden/BeamPositionCutoff = 20 mm d:So/DefaultDresden/BeamPositionCutoff = 20 mm
Angular Distribution	s:So/DefaultDresden/BeamAngularDistribution = "Gaussian" d:So/DefaultDresden/BeamAngularSpreadX = 0.0032 rad d:So/DefaultDresden/BeamAngularSpreadY = 0.0032 rad d:So/DefaultDresden/BeamAngularCutoffX = 45 deg d:So/DefaultDresden/BeamAngularCutoffY = 45 deg
Energy Distribution	d:So/DefaultDresden/BeamEnergy \approx 155 – 228 MeV u:So/DefaultDresden/BeamEnergySpread \approx 0.7 – 0.2

angular distribution recommended cut-offs are set to reduce the simulation time.

TOPAS Nozzle Geometry, Efficiency and Monte-Carlo Statistics The nozzle geometry is implemented in TOPAS based on IBA construction drawings (Dr. Benjamin Lutz). Figure 3.2 illustrates the TOPAS implementation of the IBA universal nozzle in double-scattering mode. The TOPAS nozzle model includes: (a) the first scatterer (FS), (b) the range modulation wheel (RMW), (c) the structural frame (SF), which includes (d) the second scatterer (SS) and (e) (f) the collimator jaws (JX, JY), (g) the ion chamber (IC23), (e) the snout and the patient specific components (i) aperture (AP) and (j) the compensator (CP). The space between the components is filled with air. The stopping and scattering of a proton beam depends on its energy. To increase the overall nozzle efficiency, different beam shifting and beam scattering geometries are used depending on the requested range. The quality of the treatment field homogeneity has to stay unaffected by those geometrical changes. IBA optimized its universal nozzle in double-scattering mode by using five first scatterer foils, three different contoured second scatterers and five range modulation wheel tracks. They divided the overall range interval, which the nozzle is able to deliver in double-scattering mode into eight options. Except for Option 1 and Option 2, each option is characterized by a unique combination of the SS component and the RMW track. The combinations of the FS foils do change for every requested range, and therefore they do not stay constant within an option. Each option is divided into three sub-options, whereby for each option IBA derived a unique time-depending modulation of the beam current. This modulation is also called beam current modulation (BCM). BCM is a technique, which can be used to compensate field inhomogeneities. Those inhomogeneities cannot be avoided, when using a discrete number of beam shifting and beam scattering geometries over a continuous energy interval.

An overview over the options and sub-options of the IBA universal nozzle in double-scattering mode is given in Table A. The TOPAS implementations of the five FS foils, the three CS and the RMW tracks are visualized in Figure 3.3 and Figure 3.4 in a more detailed view. The overall amount of RMW tracks is 9, whereby there are three wheels and each of them contains three different tracks. The four tracks, which are not used in double-scattering, are used when running the nozzle in single-scattering mode. Single-scattering fields are required for the irradiation of small treatment fields (e.g. eye cancers). Figure 3.5 and 3.6 illustrate an aperture and a compensator geometry in TOPAS. The corresponding images in reality are shown in Figure 2.13 and Figure 2.14. Figure 3.7 shows 100 primary protons traversing the TOPAS nozzle, including the secondary particles, that are produced in electromagnetic and nuclear interactions. The TOPAS simulation of the IBA universal nozzle is a 4D Monte-Carlo simulation, because there are geometries that have to change in time in order to obtain a therapeutic dose distribution. The time-dependent component is the RMW, that rotates in 256 time steps. The number of time steps is define by the power off resolution of the proton beam, which is 256 for a full wheel rotation. The RMW rotates with a constant frequency in the order of Hz, and the proton beam is switch on and off, depending on the requested field modulation. In the Monte-Carlo simulation this can be mapped to one wheel rotation. The nozzle efficiency increases with increasing requested range, because the overall scattering angle shrinks. Therefore the required simulation statistics depends not only on the scoring volume and the field simulation, but also on the field range. The dose measurement uncertainty is $\Delta D_{\text{Mess}} = 1\%$. The statistical dose simulation uncertainty is set to $\Delta D_{\text{Stat}} = 0.1\%$. ΔD_{Stat} is a compromise between the accuracy of the results and the simulation

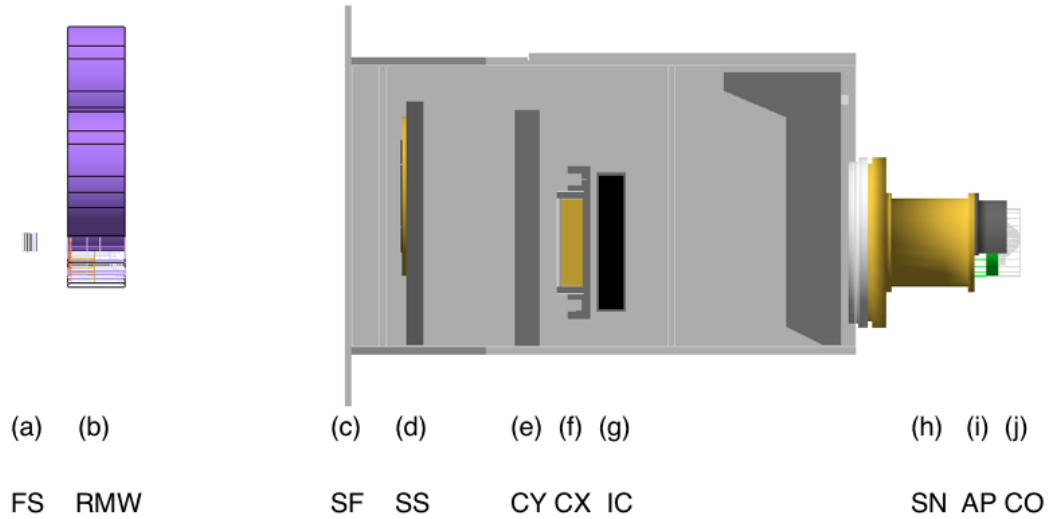


Figure 3.2: TOPAS implementation of the IBA universal nozzle in double-scattering mode based on IBA construction drawings. The TOPAS nozzle model is kindly provided by Dr. Benjamin Lutz.

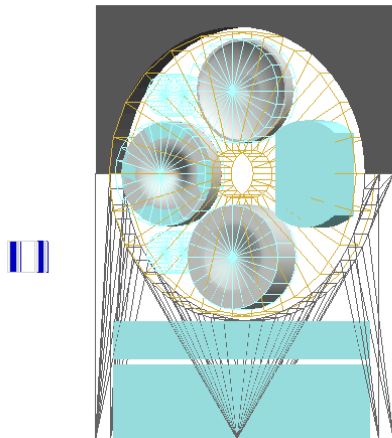


Figure 3.3: TOPAS model of the first and the second scatter, which is implemented based on IBA construction drawings.

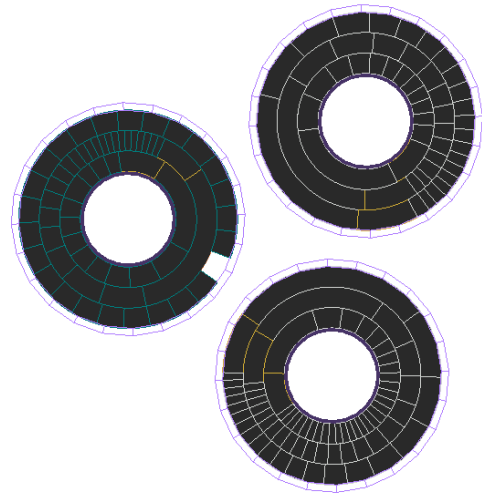


Figure 3.4: TOPAS model of range modulation wheel, which is implemented based on IBA construction drawings.

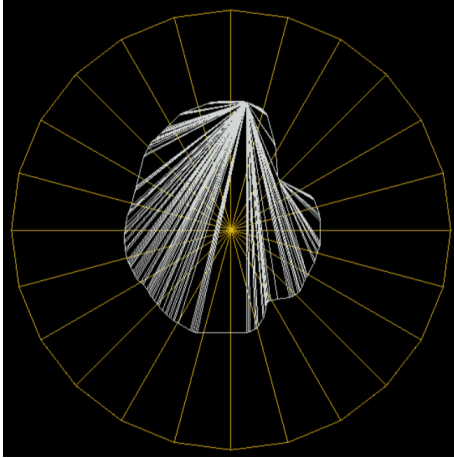


Figure 3.5: The TOPAS aperture model, that corresponds to the real one as shown in Figure 2.13.

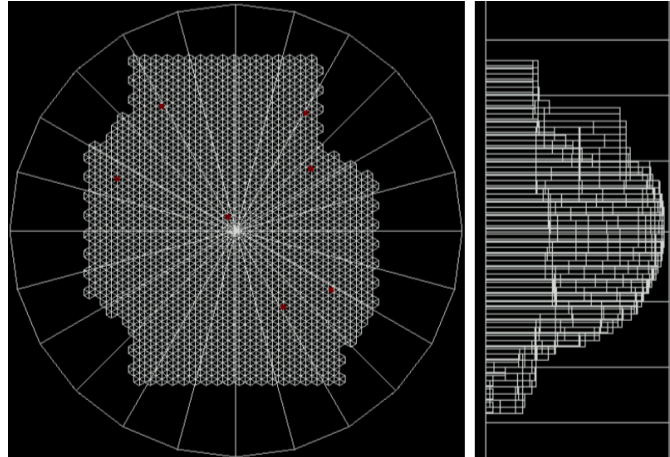


Figure 3.6: The TOPAS compensator model, that corresponds to the real one as shown in Figure 2.14.

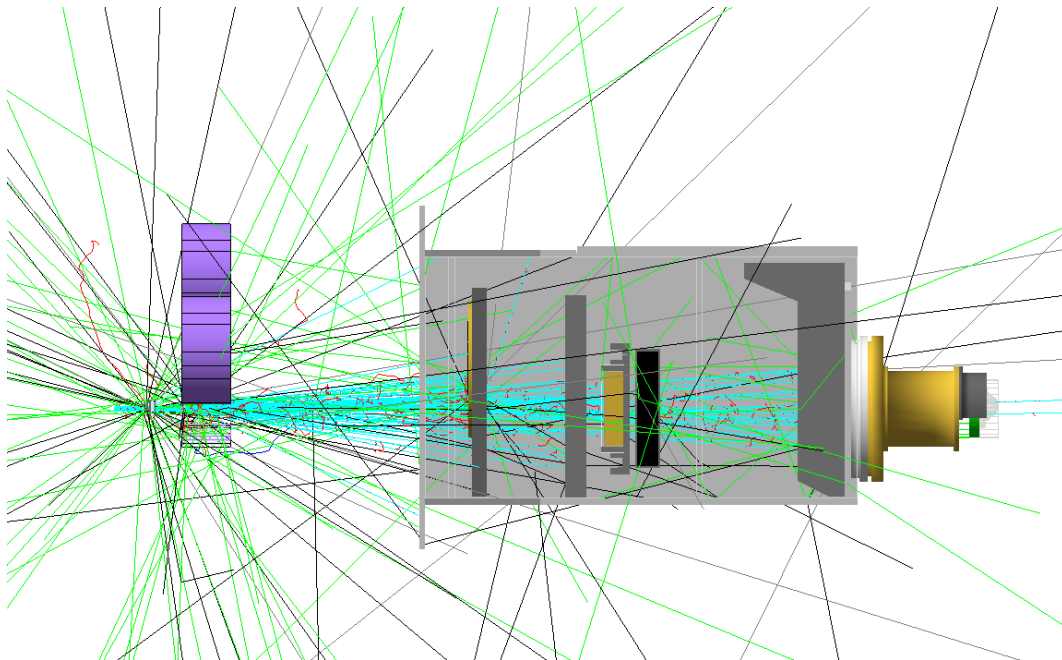


Figure 3.7: TOPAS Nozzle Simulation. 100 primary protons (cyan) traversing TOPAS Double-scattering nozzle and produce secondaries: neutrons (black), gamma (green), e^- (red), e^+ (blue) and other (grey).

effort. Nevertheless, convergence analyses show, that further increasing the simulation statistics do not significantly change the results. To achieve 0.1% statistical dose uncertainty, in a cuboid volume scorer ($3.33 \text{ mm} \times 3.33 \text{ mm} \times 300 \text{ mm}$) with 1 mm depth resolution, $N_p = 128$ millions primary protons have to be simulated. If one want to score the single Bragg curves of the SOBP at the same accuracy one has to increase N_p by a factor of ten. In this case ΔD_{Stat} also depends on the angular width of each track step, that generates a certain pristine Bragg peak (PP). For patient quality assurance simulations N_p has to be increased to 10 billions, because of the larger scoring field and the patient specific aperture, which decrease the nozzle efficiency. For the simulation of one field of a proton treatment plan, N_p should be around 50 billion in order to achieve $\Delta D_{\text{Stat}} = 0.1\%$. A treatment plan, which contains two fields, can be simulated in ten hours, when using the present computation infrastructure, which is provided by the Helmholtz Zentrum Dresden Rossendorf (HZDR). A further reduction of the simulation time is possible by applying so-called variance reduction techniques in TOPAS [41]. In principle, it is possible to pre-simulate the phase space upstream of the patient hardware for all possible configurations of range, modulation and field size. Next to the requirement of large computational resources and storage space, a disadvantage would be the inflexibility of this setup to future improvements [3, p. 92].

3.1 Adjustment and Validation of TOPAS Dose Distributions

The simulation of one dimensional SOBPs, in a water phantom do not reproduce reference measurements within clinical tolerance, when using the implemented nozzle geometry, a constant spread σ_E of the energy distribution and beam current modulation files, which were derived by IBA, in the commissioning of the real treatment head. So far the TOPAS model of the nozzle could not be used in clinics. Figure 3.8 illustrates the deviations between one measured (red) and one simulated (blue) SOBP without any further adjustments. Deviations in the slope of the SOBP fall-off region, in the SOBP range and in the overall SOBP shape can be observed. The first goal of the commissioning will be to minimize those deviations, until the uncertainties are within the measurement uncertainty, so in other words to shift the blue into the red curve.

The measurement uncertainties of the range (depth-dose profiles) and width determination (lateral profiles) are derived by using a set of around 100 SOBP fields, which are measured within the quality assurance measurements at UPTD. The range and width difference distributions are fitted with a Gaussian curve and the standard deviation σ define the measurement uncertainty. The values are presented in Table 3.2. The σ errors contain the uncertainty of the detectors in predicting the position and the relative dose of the measurement points. The depth-dose profiles are measured by using a Markus ion chamber. The lateral profiles are measured by using a diode. The clinical tolerances τ for the uncertainty of the SOBP range, modulation and width prediction are listed in Table 3.2, too. The range tolerance $\tau(R_{90})$ is defined as six times the standard deviation. $\tau(W_{50})$ is defined as eight times $\sigma(W_{50})$. Therefore, the probability that a certain range or width measurement do not full-fill the clinical criteria due statistical variations is almost zero. The uncertainty of the relative plateau dose measurement is approximately 1%. This value is obtained in personal communications with medical physicists at UPTD and contains the relative dose measurement uncertainty of the detectors (both, ion chamber and diode) and statistical fluctuations of the beam current.

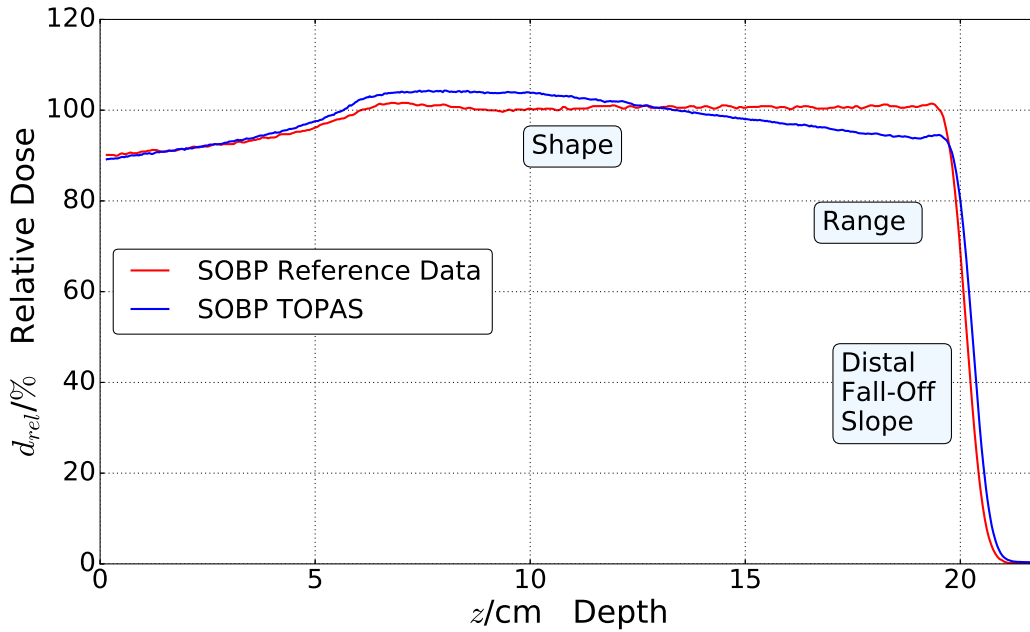


Figure 3.8: Illustration of the deviations between a simulated SOBP without further adjustments and an experimental SOBP curve, which was measured at reference measurements at UPTD. Both SOBPs correspond to a requested range $R_{\text{req}} = 19.8$ cm and a requested modulation of $M_{\text{req}} = 17.0$ cm).

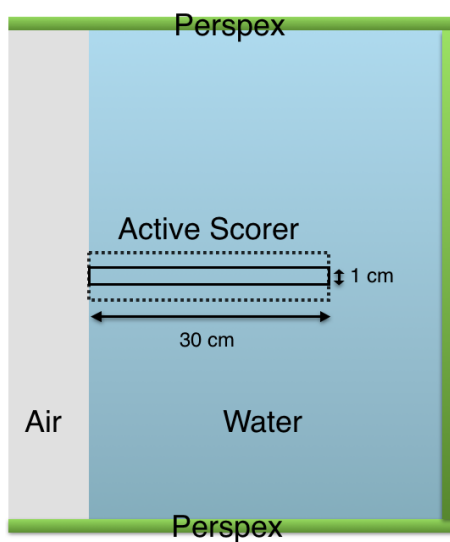


Figure 3.9: IBA blue phantom in TOPAS (Dr. Benjamin Lutz), including active scoring volume for depth-dose simulations

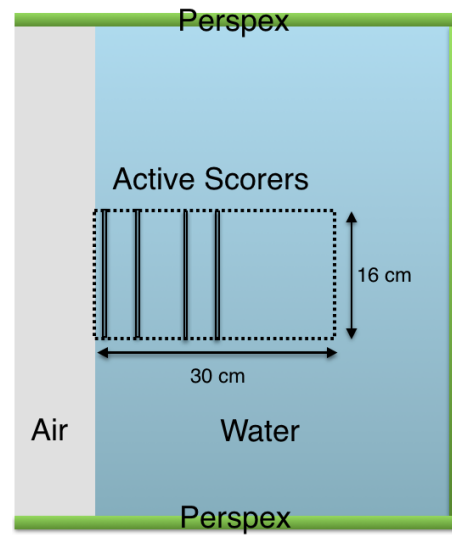


Figure 3.10: IBA blue phantom in TOPAS (Dr. Benjamin Lutz), including active scoring volume for the simulation of lateral dose profiles.

Table 3.2: Measurement uncertainties σ and clinical tolerances τ of the SOBP range, modulation, width and plateau dose prediction in a water phantom at UPTD . The σ values are derived in a statistical analyze of previous UPTD quality assurance measurements. The clinical thresholds are obtained in private communications with the medical physicists at UPTD.

Depth-Dose	$\sigma(R_{90})$ 0.25 mm	$\sigma(D_{\text{plateau}})$ 1 %	$\tau(R_{90})$ 1.5 mm	$\tau(R_{95})$ 1.5 mm	$\tau(M_{90})$ 2 mm	$\tau(R_{95,\text{proximal}})$ 2 mm
Lateral	$\sigma(W_{50})$ 0.25 mm	$\sigma(D_{\text{plateau}})$ 1 %	$\sigma(r_{20})$ 0.2 mm	$\sigma(r_{80})$ 0.15 mm	$\tau(W_{50})$ 1 mm	$\tau(W_{20}, W_{80})$ 1 mm

There are deviations in the geometrical shape and the material composition between the IBA construction drawings and reality. At the same time, it is not possible to determine these uncertainties, at least for the majority of the components, which are involved in double scattering. Usually, a component contains more than one material. For those geometries it is difficult to decide, which one is causing a certain range shift. One exception are the five first scatterer foils. They all consist out of a single material and next to the construction data, IBA provides measured data of the foil WET (water equivalent thickness). When neglecting material changes, the only remaining free parameters are the beam source settings. The most important source parameters are the mean beam energy \bar{E} and the BES. \bar{E} determines the SOBP range. The BES (or σ_E), determines the slope of the fall-off region. The influence of uncertainties in the spatial and angular beam distribution is small in passive scattering, because the scattering induced by the geometries dominates the spatial and angle distribution of the beam, which is leaving the nozzle. After the adjustment of the initial beam energy distribution (\bar{E}, σ_E) for the full therapeutic energy regime of the nozzle, one can implement a TOPAS specific beam current modulation (BCM) for every sub-option. The BCM has to be implemented afterwards, because its accuracy depends on the accuracy of the ranges and the fall-off regions of the Bragg curves, which are forming the SOBP distribution. For the adjustment of (\bar{E}, σ_E) and the BCM implementation a so-called reference dataset \mathcal{D}_{Ref} is used. \mathcal{D}_{Ref} contains 24 SOBP depth-dose curves including their corresponding first pristine Bragg peak curves (PP1). So, for every sub-option, there is one measured reference data SOBP and one corresponding measured PP1. \mathcal{D}_{Ref} is the fundamental experimental input data, which is used by the proton treatment planning system (TPS) in order to generate its beam model. It is measured in the so-called IBA blue water phantom with 0.5 mm depth resolution by using the so-called advanced Markus ion chamber (0.02 ccm PTW). The reference data serves as the physical ground truth.

To finish the commissioning of the shape of the SOBP fields, the determined adjustments have to be tested by using a new dataset, which is independent of \mathcal{D}_{Ref} . Therefore, a so-called validation dataset \mathcal{D}_{Val} is used, which is measured with the same resolution as \mathcal{D}_{Ref} , but with different ranges and modulations. \mathcal{D}_{Val} contains 24 SOBP depth-dose curves, one for every sub-option, and 54 lateral SOBP dose profiles, which correspond to 16 different SOBP fields. The snout position, which is used in \mathcal{D}_{Ref} and \mathcal{D}_{Val} is 10 cm for all fields. For ranges larger than 15 cm two square apertures (10 cm \times 10 cm) are used, otherwise its just one. Figure 3.9 illustrates the TOPAS representation of the IBA blue water phantom, including the active scoring volume, which is used in the simulation. The scorer has a cubic shape (1 cm x 1 cm x 30 cm). to map the depth dose measurements, where a square shaped Markus ionization chamber is used. The lateral scorer extension, has to be small enough to ensure lateral homogeneity. Figure 3.10 visualizes the IBA blue phantom with active scoring plates for the

simulation of lateral dose profiles for one SOBP field.

3.1.1 Adjusting TOPAS SOBP Fall-Off Region

The SOBP fall-off region will be adjusted by an iteratively optimization of the BES value in TOPAS. The iteration is continued until the deviations in depth at the fall-off region between the simulations and the measurements fall below a certain threshold. Therefore, the fall-off regions of the simulated and the measured PP1s are compared instead of comparing the full SOBP depth-dose curves. The threshold is set to 0.5 mm, which is in the order of the range measurement uncertainty. The start values of the BES iteration are determined by using experiences of a previous study [42] and measured data of the beam energy distribution, which are kindly provided by Johannes Petzoldt.

The energy spread σ_E of the initial proton beam, which enters the nozzle, influences the range straggling of every pristine Bragg peak (PP). An increase in σ_E is leading to an increase in the range straggling (RS). The larger the range straggling, the larger the negative slope of the distal fall-off region. The fall-off region of a SOBP is influenced at least by the first two pristine Bragg curves (PP1, PP2). Therefore the SOBP fall-off depends next to the range straggling of these two peaks also on their relative weights. To avoid this dependency, the measured PP1s are used to determine an optimal energy spectrum. For every measured PP1, with a certain requested range R_{req} , an accurate TOPAS BES input parameter has to be determined, in order to be able to re-simulate the measured PP1 with high accuracy. The quality of a certain (BES, R_{req}) PP1 is rated by analyzing the depth deviations and three characteristic dose points at the fall-off region (90 %, 80 % and 20 %). Those depth-deviations are denoted as ΔR_{90} , ΔR_{80} and ΔR_{20} . They are illustrated in Figure 3.11. If those deviations would be zero, the corresponding BES value would be optimal. To analyze the full range straggling, three depth-deviations, which corresponds to characteristic dose points in the proximal shoulder region, are calculated, too. They are labeled as ΔRv_{90} , ΔRv_{80} and ΔRv_{70} . The accuracy of the calculation of the depth differences between the simulated and measured PP1, depends on the accuracy of the normalization. To increase the normalization accuracy, both Bragg curves are fitted, by using a theoretical representation of the Bragg curve, the so-called Bortfeld- fit [14]. The Bortfeld-fit is valid for proton energies between about 10 and 200 MeV. The main four model constituents are:

1. A power-law relationship describing the range-energy dependency $R_0 = \alpha E_0^p$ ($E_0 = E(d=0)$ initial beam energy at depth $d=0$, $\alpha = 0.0022 \text{ cm MeV}^{-p}$, $p = 1.77$)
2. A linear model for the fluence reduction due to nonelastic nuclear interactions, assuming local deposition of a fraction of the released energy $\Phi(z) \propto 1 + \beta(R_0 - z)$ ($\beta = 0.012 \text{ cm}^{-1}$, z depth)
3. A Gaussian approximation of the range straggling distribution $\sigma_{\text{mono}} = 0.012 R_0^{0.935} \text{ cm}$ Width of Gaussian range straggling
4. A representation of the energy spectrum of poly-energetic beams by a Gaussian with a linear tail $\sigma_{E,0} \approx 0.01 E_0 \text{ MeV}$ width of Gaussian energy spectrum, $\epsilon \approx 0.0 - 0.2$ fraction of primary fluence contributing to the "tail" of the energy spectrum

As the heart of the analytical expression is the parabolic cylinder function $\mathcal{D}_x(y)$ one can split $D(z)$ into three depth intervals depending on the domain of the parabolic cylinder function. The domain is determined by the arguments R_0 and the total range straggling standard deviation σ ($\sigma^2 = \sigma_{\text{mono}}^2 + \sigma_{E,0}^2 \alpha^2 p^2 E_0^{2p-2}$).

$$D(z) = \begin{cases} \hat{D}(z) & \text{for } z < R_0 - 10\sigma \\ D(z) & \text{for } R_0 - 10\sigma \leq z \leq R_0 + 5\sigma \\ 0 & \text{otherwise} \end{cases} \quad (3.2)$$

The depth-dose distribution in water is shown in equation (3.3) and equation (3.4). Φ_0 is the primary particle fluence.

$$\hat{D}_{\text{H}_2\text{O}} = \frac{\Phi_0}{1 + 0.012R_0} [17.93(R_0 - z)^{-0.435} + (0.444 + 31.7\epsilon/R_0)(R_0 - z)^{0.565}] \quad (3.3)$$

$$D_{\text{H}_2\text{O}} = \Phi_0 \frac{e^{-(R_0-z)^2/4\sigma^2} \sigma^{0.565}}{1 + 0.012R_0} \cdot \left[11.26\sigma^{-1} \mathcal{D}_{-0.565} \left(-\frac{R_0 - z}{\sigma} \right) \right. \\ \left. + (0.157 + 11.26\epsilon/R_0) \mathcal{D}_{-1.565} \left(-\frac{R_0 - z}{\sigma} \right) \right] \quad (3.4)$$

Using the Bortfeld- fit a Bragg curve can be distinct described by the four parameter tuple (R_0 , Φ_0 , σ , ϵ). The fit has some difficulties for Bragg curves, which are sliced out of large SOBP fields, which are created in passive scattering. Nevertheless, by reducing the depth interval to the region of interest (Figure 3.11), all the 24 PP1 pairs can be fitted with high accuracy. σ_{mono} can be calculated analytically by using σ_{E_0} : $\sigma_{\text{mono}} \approx 0.012R_0^{0.935}$. Comparing the σ_{E_0} would be another possibility for adjusting the BES, because it represents the full range straggling of the pristine Bragg peaks.

Next to the σ_E , the range straggling is influenced by the water equivalent thickness (WET) of the nozzle and by the amount of water, the beam is traversing in the water phantom. The nozzle WET is created mainly by the specific RMW track step and the second scatterer, which is range compensated. Within an option the nozzle WET is increasing continuously, because of the first scatterer foils (FS). With increasing beam energy more FS material is required, to achieve a similar overall nozzle scattering angle. There are three down-jumps of the nozzle WET. Those down-jumps allow to reduce the beam energy by still achieving higher requested ranges. Therefore the IBA nozzle can be run at relatively high initial beam energies ($E_{\text{initial}} \approx 155 - 228$ MeV). Without these down-jumps, the nozzle has to be run at lower initial beam energies, at least for the first options. This would require an increase in the degrading (in the ESS), because the beam, which is leaving the cyclotron has a constant mean beam energy of 235 MeV. To achieve a similar sharpness of the beam energy, spatial and angular distribution, while applying a higher degrading, more protons have to be filtered. The overall efficiency of the proton delivering system would decrease. Figure 3.12 shows the mean beam energies, that are required to create SOBP fields with ranges as used in the reference data. As the BES depends on E_{initial} , it the down-jumps have an influence on the BES(R_{req}) distribution. BES measurements of the of the beam, which behind the ESS predicts BES values between 0.7% and 0.2% for energies in the

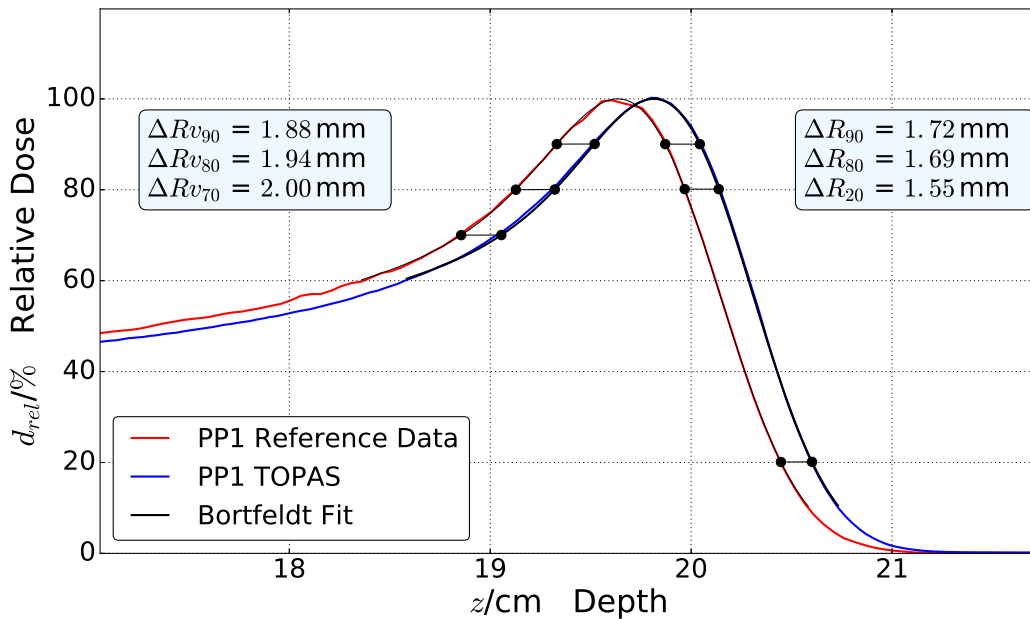


Figure 3.11: A reference data PP1 ($R_{req} = 19.8$ cm, $M_{req} = 17.0$ cm) and the corresponding simulated PP1, whereby both Bragg peaks are partially fitted using the theoretical Bortfeldt fit [14]. This minimizes the dependency of the range offset calculation on normalization uncertainties caused through the binning of the measuring and simulation grid. The range offsets are calculated at three characteristic points at the proximal PP1 shoulder- and at the distal fall-off region.

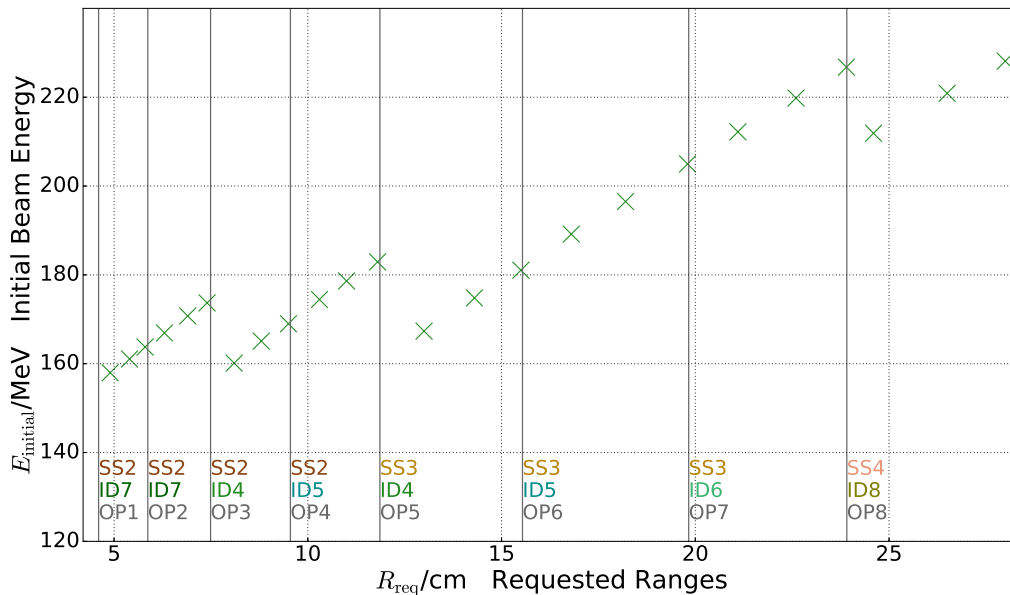


Figure 3.12: Mean beam energies, which corresponds to all requested ranges of the reference data SOBPs, for all TOPAS reference data simulation. The data is calculated based on the required nozzle WET, by using PSTAR data (NIST, [10]).

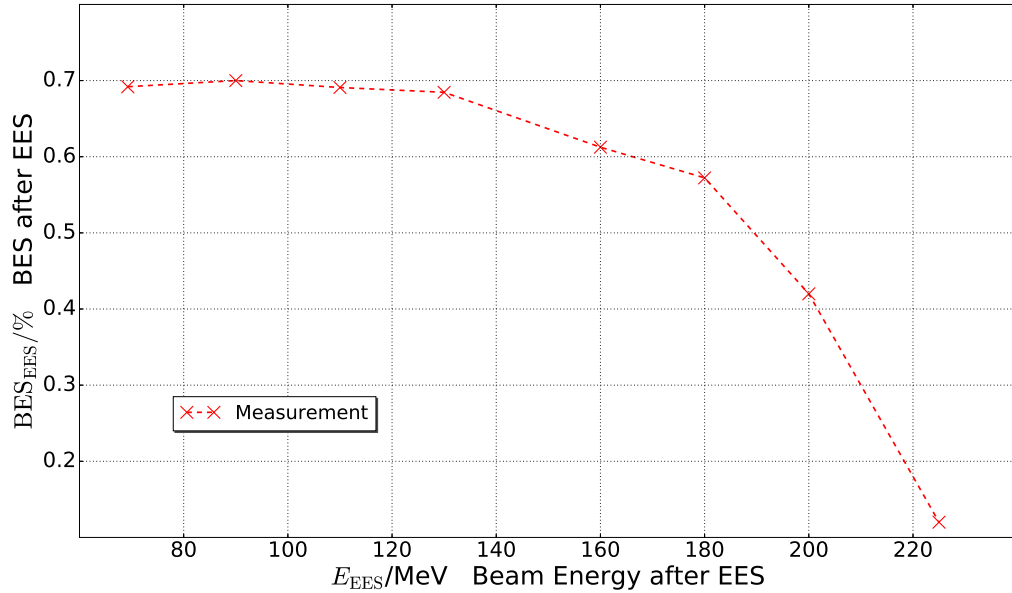


Figure 3.13: Measured BES values of the proton beam straight after leaving the ESS. The data were measured by Johannes Petzoldt at UPTD.

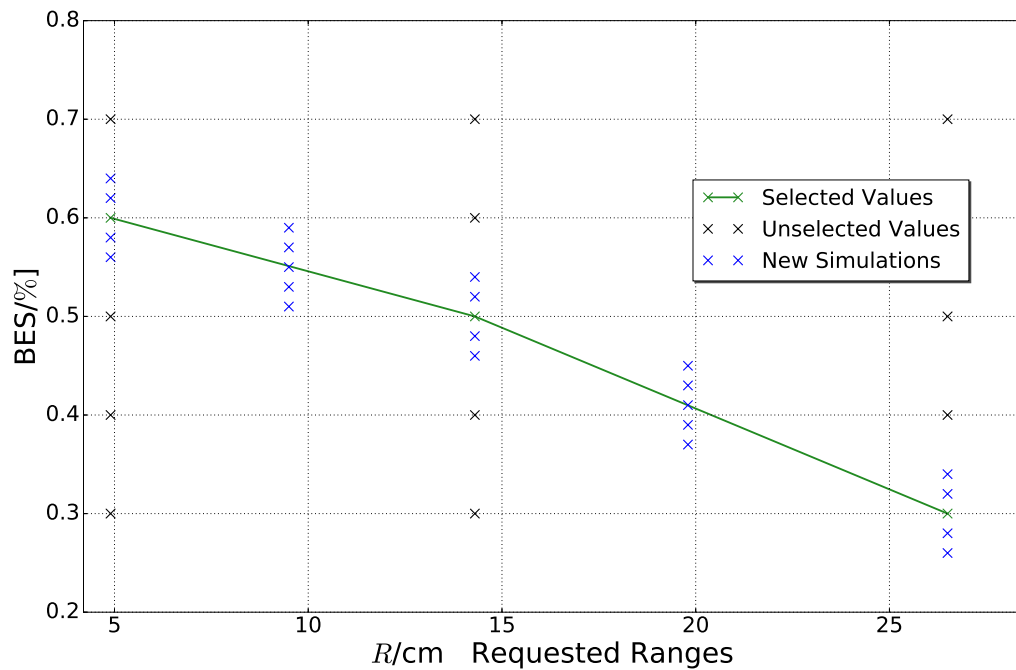


Figure 3.14: Iterative BES Calculation including the (R_{req}, BES) simulation points that corresponds to the first step of iterative BES calculation procedure.

interval [155 MeV|228 MeV] (Figure 3.13). There are no beam line components between the ESS and the nozzle, which have the potential, to change the beam energy distribution dramatically. Therefore the measurements are taken as a first BES approximation. The iteration is started by simulating PP1 curves with different BES values between 0.7% - 0.2%, for one low, one center and one high \mathcal{D}_{Ref} range. The principle of function of the BES optimization is illustrated in Figure 3.14. After simulating the first (BES, R_{req}) distributions, one select the ones with minimal fall-off deviation to the corresponding measured PP1s. The selected (BES, R_{req}) are linear interpolated. Around the interpolation lines new (BES, R_{req}) points are simulated and the process goes in the next iteration step. To limit the simulation effort the iterative procedure is stopped until the depth deviations in the fall-off region fall below a threshold of 0.5 mm, which is in the order of the range measurement uncertainty.

3.1.2 Adjusting TOPAS SOBP Range

The SOBP range is adjusted by shifting the initial mean beam energy E_{initial} by a constant value ΔE for each nozzle option separately. ΔE is derived by calculating the mean option range deviations $\langle \Delta R_{80} \rangle$ between the simulated and the measured PP1. To further increase the range accuracy between the simulations and the measurements, the thickness of the first scatterer foils is adjusted.

Similar, to the adjustment of the SOBP fall-off region, the SOBP range is adjusted by using only the first pristine Bragg peak (PP1). The SOBP range depends on the relative weights of the PP and this dependency changes with energy and when implementing beam intensity modulations into TOPAS. The Bortfeld- fit is used to minimize the dependency of the range offset on normalization uncertainties of the Bragg curves. The range offset calculation is visualized in Figure 3.15. The PP1s are simulated by using the adjusted BES values, which are derived in the previous section. IBA applied an option depending range shift, during the commissioning of the nozzle at UPTD. They applied those shifts to correct geometrical uncertainties, which lead to range uncertainties between their calculated predictions and QA measurements. They observed range offsets below 2 mm for every option. A constant, option depending range shift is applied in TOPAS, too. It would be difficult to justify the implementation of an energy depending range offset. Obviously, something must be wrong with the shape of the first scatterer foils, if the range variations within an option are too high. The FS foils are the only geometrical components, which are changed within an option. In addition an energy depending ΔR_{80} could lead to an over fitting of the nozzle model in TOPAS. Figure 3.16 visualizes the range offsets between the 24 \mathcal{D}_{Ref} PP1s and the corresponding simulated ones with adjusted fall-offs. The ΔR_{80} variations within the options are too high to justify the implementation of a mean option range shift in TOPAS. In addition, there are two options (Option 3,4), where $\langle \Delta R_{80} \rangle$ exceeds 2 mm, which is the maximum range uncertainty observed by IBA in the nozzle commissioning.. Therefore, the thicknesses of the FS foils are further adjusted by replacing the values, which are extracted by using the IBA construction drawings, by IBA measurements. IBA measured the thickness of each of the FS foils, which is used in double-scattering.

The measured foil thicknesses are listed in the units of water equivalent thickness (WET) and has to be transformed into real thicknesses for TOPAS implementation. A detailed description of the WET concept can be found in Ref. [43]. \bar{S}_w and \bar{S}_m are defined as the mean mass stopping powers

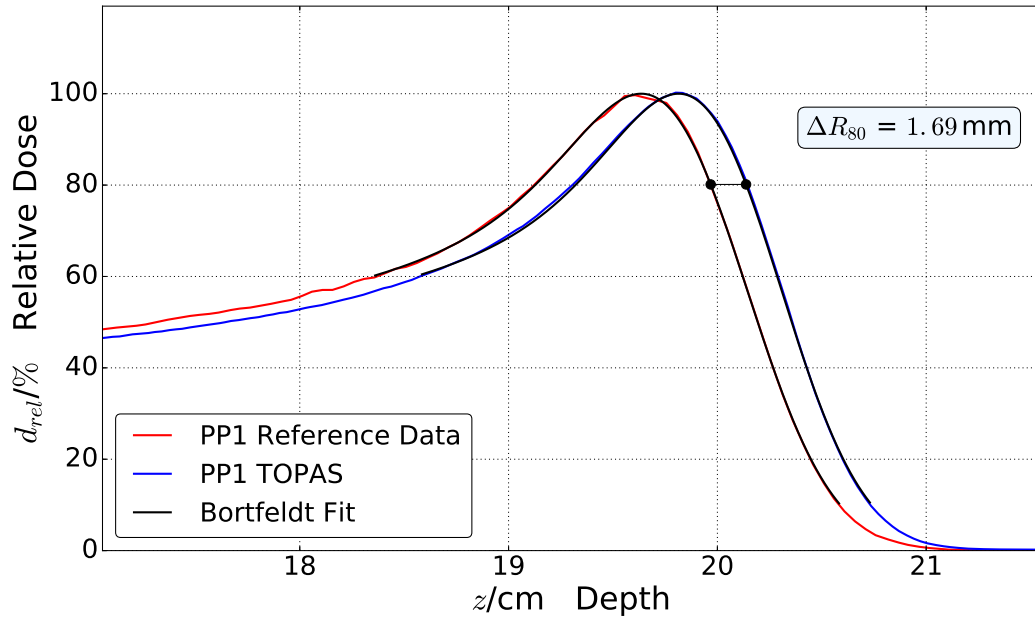


Figure 3.15: Range comparison of a TOPAS PP1 and a reference data PP1 ($R_{\text{req}} = 19.8 \text{ cm}$) with adjusted distal fall-offs.

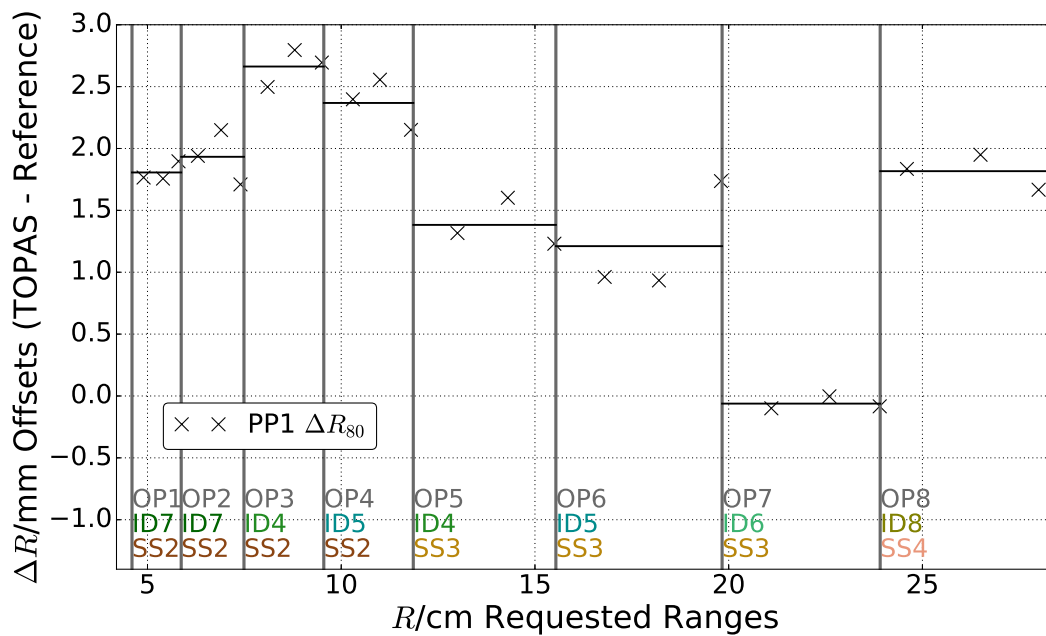


Figure 3.16: Range offsets ΔR_{80} of all simulated and measured PP1 pairs over the requested range including all IBA options and mean option offset values.

for protons in water (w) and in a material (m). The ratio $\bar{S}_w/\bar{S}_m = 0.516$ is provided by IBA. Table 3.3 lists the old thicknesses d_{old} from the construction drawings and the new ones d_{new} , coming from IBA measurements at UPTD, for the five foils used in double scattering (Foil 2, 3, 5, 6, 9).

$$\text{WET} = \frac{\rho_m \bar{S}_m}{\rho_w \bar{S}_w} \quad \rho_m | \rho_w = \text{material and water density} \quad (3.5)$$

$$d_{\text{TOPAS}}[\text{mm}] = \frac{d_{\text{IBA}}[\text{g}/\text{cm}^2]}{\text{WET}} = d_{\text{IBA}} \cdot \frac{\rho_w \bar{S}_w}{\rho_m \bar{S}_m} = \frac{d_{\text{IBA}}}{0.516 \cdot \rho_{\text{Tantalum}}} \quad (3.6)$$

Table 3.3: List of FS foil thicknesses of the five foils that are used in double-scattering at UPTD. d_{old} are extracted from IBA construction drawings. d_{new} corresponds to IBA measurements at UPTD.

Foil Label	2	3	5	6	9
Material	Tantalum	Tantalum	Tantalum	Tantalum	Tantalum
d_{old}/mm	0.2	0.8	0.4	0.1	0.05
d_{new}/mm	0.2096	0.8725	0.4191	0.0817	0.0348

3.1.3 Implementing TOPAS Beam Current Modulation

The beam current modulation is implemented in TOPAS by using the simulated pristine Bragg curves (PP), with adjusted fall-off regions and ranges, as base functions for fitting the measured SOBPs. The fit weights determine the ratio how much a certain PP has to be increased or lowered in fluence. The weights of the simulated PPs can be modulated by changing the amount of simulated particles in time. The RMW time digits that correspond to a certain PP, are derived by scoring depth-dose distributions for every time digit and by determining jumps in the ranges of those depth-dose curves.

The resolution of the mechanism, which controls, if a proton beam is powered on or off during an irradiation is 256 for one rotation of the range modulation wheel. Therefore, a TOPAS Monte-Carlo simulation of a SOBP field with full modulation, is divided into 256 time steps. The various rotations and irradiations of the RMW in reality are mapped to one RMW rotation in the Monte-Carlo simulation. In each time step during the simulation the amount of simulated particles, which should traverse the RMW, can be adjusted. The sampling rate of the beam in angle is 1.4° . The precise angular starting position of the beam in the RMW is an adjustable parameter of the nozzle machine and not generally known. To implement the BCM in TOPAS, it is necessary to know, which time digits corresponds to a certain PP. This depends on the track geometry. Five different tracks are used in passive scattering at UPTD. For each track, a full-modulation SOBP is simulated and for each time step the corresponding Bragg curves PP_{digit} are scored in a water phantom. A change in range R_{digit} of the PP_{digit} corresponds to a change in the track step. Each track step changes the nozzle WET differently. Figure 3.17 visualizes the $R_{\text{digit}}(\text{digit})$ function for the RMW track ID5 (Option 4,6). $R_{\text{digit}}(\text{digit})$ has the shape of a step function, whereby each step corresponds to one RMW track step. The R_{digit} points at small digits belong to the first digits, where the beam is traversing a so-called stop blocker. Since, only a small amount of particles do reach the water phantom and is able to deposit dose there, they cannot be interpreted as ranges. The border digits, where the nozzle WET changes are derived by using the derivative of $R_{\text{digit}}(\text{digit})$ (Figure 3.17, lower sub-plot). $R'_{\text{digit}}(\text{digit})$

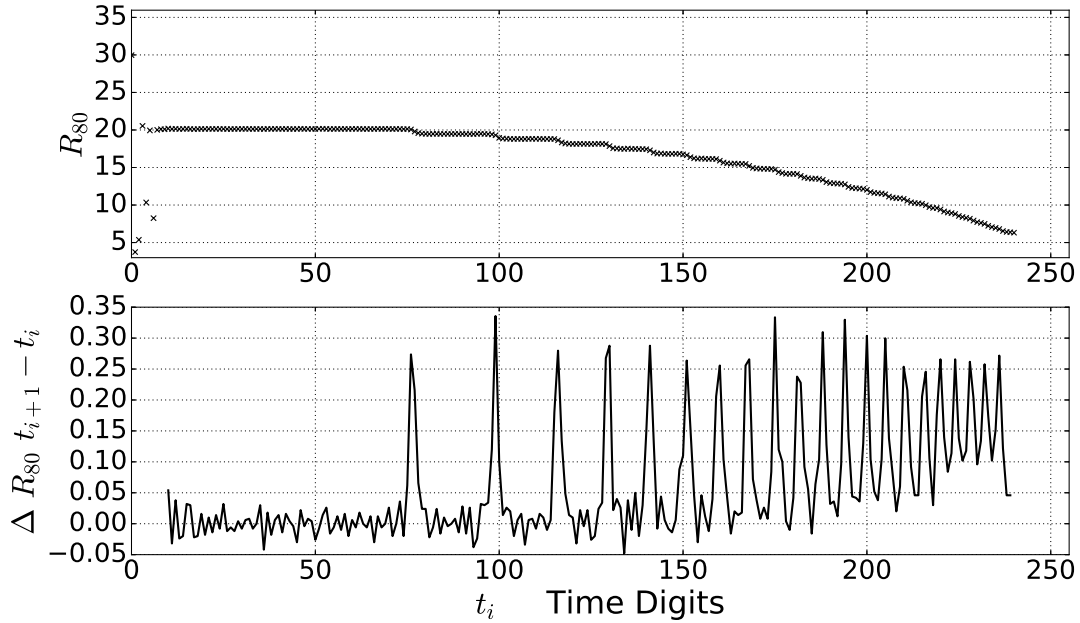


Figure 3.17: Step Function. $R_{80}(\text{digit})$ - function including corresponding difference quotient for Track ID 5 (option 6).

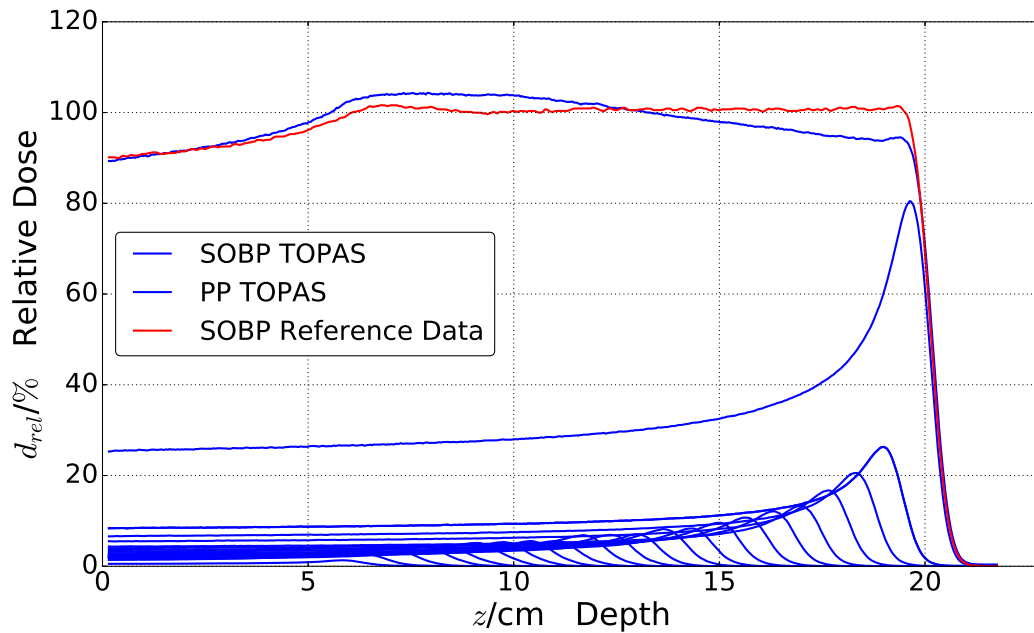


Figure 3.18: A simulated TOPAS SOBP ($R_{\text{req}} = 19.8 \text{ cm}$, $M_{\text{req}} = 17.0 \text{ cm}$) without beam current modulation and its corresponding base functions (PP), which are derived using the procedure as illustrated in Figure 3.17.

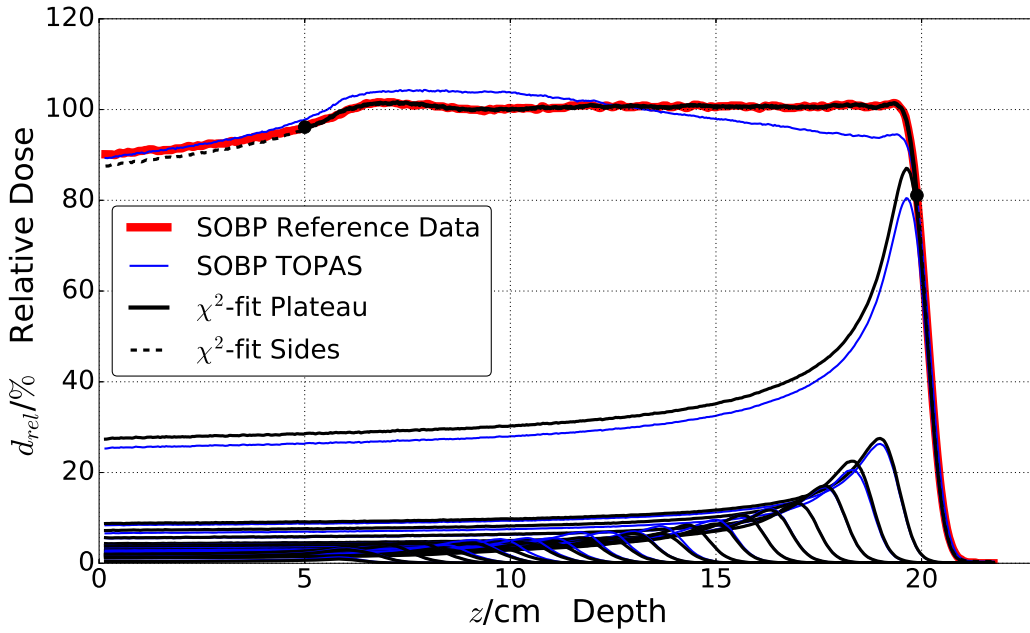


Figure 3.19: χ^2 -Fit of a reference data SOBP ($R = 19.8$ cm, $M = 17.0$ cm) using the PP of the corresponding TOPAS SOBP as base functions.

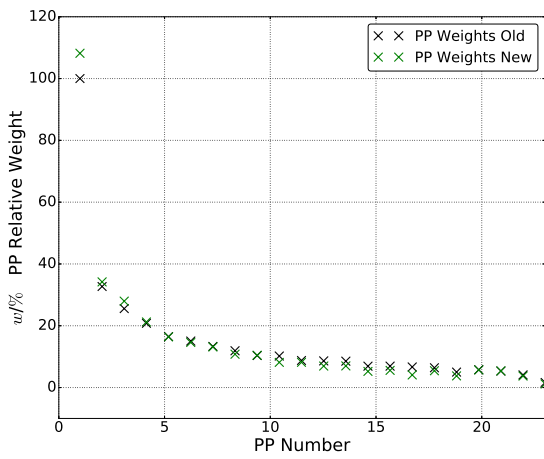


Figure 3.20: Absolute BCM weights before and after χ^2 -fit as illustrated in Figure 3.19.

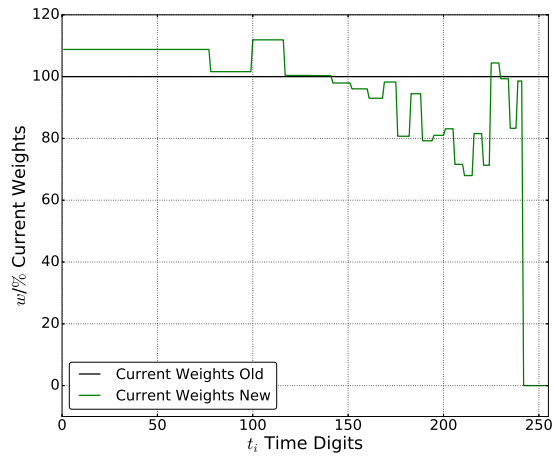


Figure 3.21: BCM function, that shows the relative weight enlarging or delarging over one full RMW rotation (Figure 3.19).

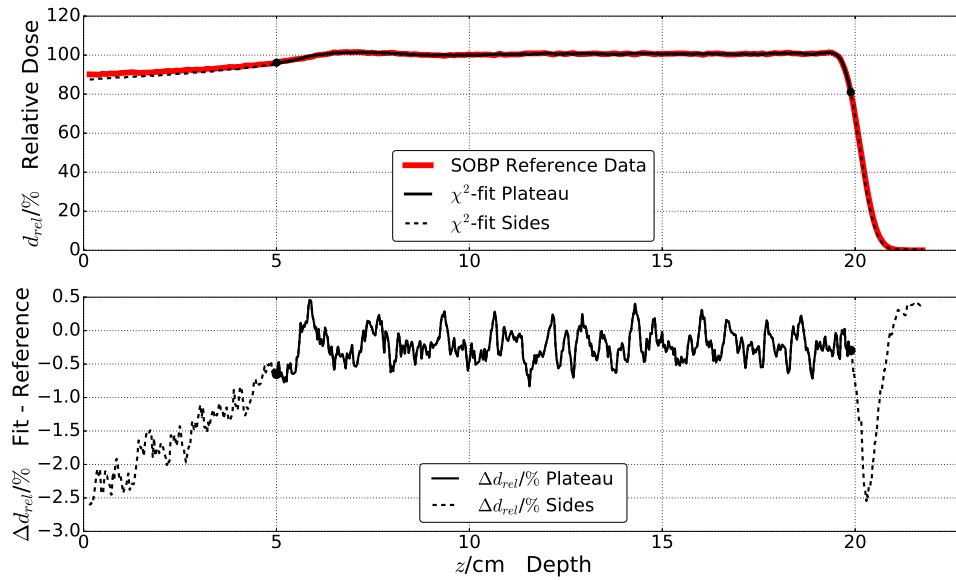


Figure 3.22: χ^2 - fit of reference data SOBP ($R = 19.8$ cm, $M = 17.0$ cm) using the PP of the corresponding TOPAS SOBP as base functions. The fit region is limited to a region of interest, excluding the proximal SOBP shoulder region and the distal fall-off region. The dose deviations between the χ^2 -fit and the reference data SOBP are illustrated in the lower sub-plot.

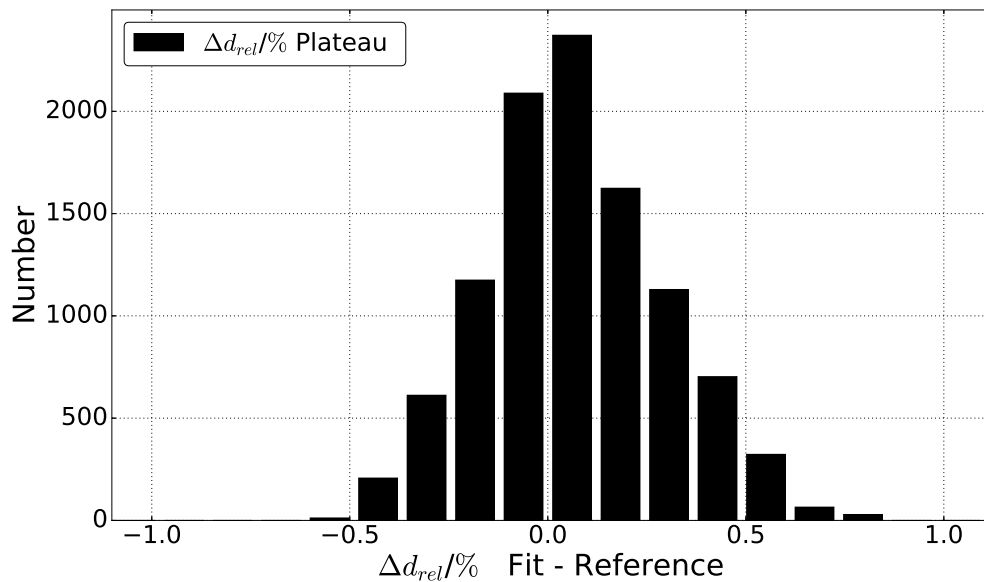


Figure 3.23: Distribution of the relative dose differences Δd_{rel} between χ^2 - fit and reference SOBP ($R = 19.8$ cm, $M = 17.0$ cm).

shows several maximum peaks. The digits digit_{\max} define, which time digit belongs to which PP. At large time digits, the beam is traversing track steps with smaller angular widths. Because of the spatial beam extension, the beam irradiates more than one track step at the same time. Therefore, the peak resolution ($R'_{\text{digit}}(\text{digit})$) decreases with increasing digit number. Nevertheless, for each track the maximum peaks can be distinguished, when simulating at least 10 million primary particles at each time step.

It is not in general possible to derive analytically the optimal weight distribution, which would lead to a flat SOBP, for a given number of PP base functions. Therefore the weights are derived, by fitting the \mathcal{D}_{Ref} SOBPs. The simulated PP are the base functions of the fit. It has to be guaranteed, that the measured and the simulated curves have a similar depth grid. Small depth offsets, can decrease the fit quality, dramatically. Especially, regions with high dose gradients (fall-off region, proximal shoulder region) are sensitive to depth uncertainties. Therefore the fit domain, is limited to dose points in the depth interval $[z_{\min}|z_{\max}]$. z_{\max} has the value of the SOBP range R_{80} and z_{\min} is approximately $(R_{\text{req}} - M_{\text{req}})/M_{\text{req}}$. The derivation of the fit weights is a linear optimization problem. The set of weights has to be calculated, that minimize the modulus difference between the simulated SOBP f_{TOPAS} and the reference data one $f_{\text{reference}}$. Minimizing the square difference instead of the modulus is called χ^2 -fit. χ^2 -fits are used to derive the optimal beam current modulation weights.

$$f_{\text{TOPAS}} = \sum_i^N w_i \cdot PP_i \quad w_i \text{ weights, } PP_i \text{ pristine Bragg peaks} \quad (3.7)$$

$$\min |f_{\text{TOPAS}} - f_{\text{reference}}| \rightarrow \text{optimal } w_i \quad (3.8)$$

Figure 3.19 illustrates the principle of calculation of the weights, which are used to implement a BCM in TOPAS. Figure 3.22 compares the χ^2 -fit to the measured SOBP. In the region of interest the maximum differences between the fit and the measured curve are below 1%. The deviations are further visualized in a histogram-plot (Figure 3.23). The deviation distribution is Gaussian in first approximation with a spread of around 0.3%.

3.1.4 Validating TOPAS Depth-Dose Curves

The accuracy of the adjusted TOPAS beam source settings is validated by using a validation measurement data set \mathcal{D}_{Val} . For every sub-option there is one measured depth-dose distribution available. In addition, there are 54 measured lateral profiles. Both, the depth-dose and the lateral distributions, are simulated and deviations between the simulations and the measurements are systematically analyzed.

The depth-dose distributions are compared in the distal fall-off region by comparing the simulated and measured ranges at three characteristic points (ΔR_{90} , ΔR_{80} , ΔR_{20}). In the proximal shoulder region the relative dose difference distribution is fitted by a Gaussian curve and the mean values and standard deviations are derived. The mean value μ is a benchmark for a systematic deviation in the slope of the plateaus. Both plateaus are normalized to their central plateau regions. The standard deviation σ is a benchmark for the error of the relative dose prediction of TOPAS in the central plateau region. The lateral profiles are compared by analyzing deviations of the lateral field sizes W_{50} and the lateral penumbras of the left P_{left} and the right P_{right} profile flank. r_{20}^{left} , r_{80}^{left}

r_{20}^{right} and r_{80}^{right} define the lateral positions, which corresponds to 20% and 80% dose at the left and the right profile flank, when normalizing the lateral profile to its central plateau region. The plateau regions are compared by fitting the relative dose differences with a Gaussian curve and by deriving μ and σ .

$$W = r_{50}^{\text{right}} - r_{50}^{\text{left}} \quad (3.9)$$

$$P_{\text{left}} = r_{80}^{\text{left}} - r_{20}^{\text{left}} \quad (3.10)$$

$$P_{\text{right}} = r_{80}^{\text{right}} - r_{20}^{\text{right}} \quad (3.11)$$

3.2 Output Factor Simulations for Absolute Dosimetry

So far, the simulated depth-dose distributions have to be normalized to the measurements. In principle, this is not necessary, because Monte-Carlo allows the simulation of absolute doses. Nevertheless, an absolute dose output of a Monte-Carlo simulation has to be benchmarked and validated by using measurements. Therefore simulated output factors are compared to measurements for different independent data sets, with varying complexity. The clinical required accuracy of the prediction of absolute doses at UPTD is 1%. A reference field \mathcal{F}_{Ref} ($R_{\text{req}} = 16$ cm, $M_{\text{req}} = 10$ cm), which is measured in quality assurance (QA) measurements at UPTD is used to benchmark the simulated TOPAS output factors. The validation of the simulated output factors is performed by using further QA (quality assurance) reference measurements \mathcal{M}_{QA} , patient QA measurements $\mathcal{M}_{\text{Patient}}$ and measurements \mathcal{M}_{Res} , which are designed for other research purposes.

3.2.1 Comparison between TOPAS OF Simulations and Reference Measurements

To simulate the output factors, dose scoring geometries are implemented in TOPAS, which represent the monitor unit (MU) counting in the ion chamber. By convention, at UPTD, 100 MU corresponds to the dose of 2 Gy, which is measured at the position $z_{\text{calib}} = 11.72$ cm of this reference field ($R_{\text{req}} = 16$ cm, $M_{\text{req}} = 10$ cm) in a water phantom, whereby two square apertures (10 cm \times 10 cm) are used and the snout position is $d_{\text{Snout}} = 10$ cm. The OF reference measurements \mathcal{M}_{QA} and \mathcal{M}_{Res} are simulated in a water phantom with 0.5 mm resolution in depth. The active scoring volume in the water phantom is visualized in Figure 3.9.

At UPTD a so-called IC23 ion chamber is used to monitor the proton beam during the irradiation and to count the monitor units, which represent a certain treatment field. The IC23 contains two independent components, the IC2 and IC3. Both are separate ion chambers. The IC2 is the one which is routinely used for the measurement of the MU signal. The IC3 is implemented for safety issues. If the measured MU signal in the IC3 is larger compared to the signal, which is expected for a certain treatment field, the proton beam is stopped.

In double-scattering the MU are collected between a pad and a plate in the IC2. Instead of simulating the full charge collection in the TOPAS model of the IC2 precisely, the dose deposition in a representative volume V_{IC23} is simulated. This is justified, because the measured MU signal is proportional to the deposited dose in the area of charge collection. Four representative volumes are implemented, to

study the OF dependency on the V_{IC23} size. The smallest one has a lateral extension in the order of the pad size. The lateral extension of the largest one is around four times higher. The volumes are centered at the border between the IC2 and IC3 and are divided into four bins in depth. Therefore, the dependency of the OF on the lateral and distal V_{IC23} extension is studied. The TOPAS model of the IC23, including the representative volume scorers is visualized in Figure 3.24.

$$\begin{aligned}
 V_{\text{Pad}} &= \frac{\pi}{2} \cdot 23.25^2 \times 29.6 \text{ mm}^3 \\
 V_{\text{IC23}_1} &= V_{\text{IC23}_2} = 7.75 \times 7.75 \times 14.8 \text{ mm}^3 \\
 V_{\text{IC23}_3} &= 23.25 \times 23.25 \times 29.6 \text{ mm}^3 \\
 V_{\text{IC23}_4} &= 93 \times 93 \times 29.6 \text{ mm}^3
 \end{aligned}$$

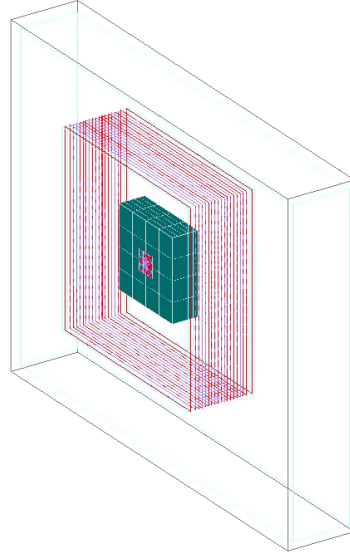


Figure 3.24: TOPAS model of the IC23, based on IBA construction drawings. The model includes three cubic scoring volumes (green) for dose simulations, which are used to derive output factors in TOPAS.

The simulated dose signal is transformed to a MU signal by using the air density and the mean energy to produce an ion pair W_{air} [33].

$$q_{\text{IC23}} = \frac{\rho_{\text{air}} \cdot V_{\text{IC23}}}{W_{\text{air}}} \cdot D_{\text{IC23}} = \alpha_{\text{IC23}} \cdot D_{\text{IC23}} \quad (3.12)$$

By assuming an air temperature of $T = 22^\circ$ and an air pressure of $p = 1013 \text{ hPa}$ the air density lies around $\rho_{\text{air}} = 1.196 \cdot 10^{-3} \text{ gcm}^{-3}$. For the mean energy to produce an ion pair W_{air} , it is taken into account, that W_{air} has a small energy dependence for particles heavier than electrons [44]. Therefore, the dose that is deposited by photons and electrons is scored independently from the dose that is deposited by heavier particles.

$$W_{\text{air}} = \begin{cases} 33.97 \text{ J/C} & \text{for electrons and photons} \\ 34.2 \text{ J/C} & \text{for all other particles heavier than electrons} \end{cases} \quad (3.13)$$

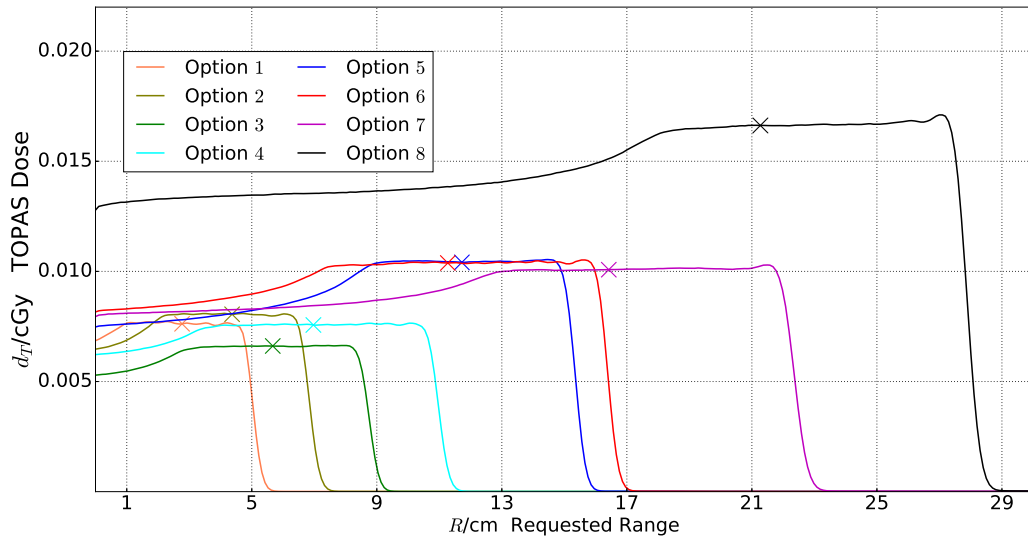


Figure 3.25: Simulated TOPAS SOBPs, that corresponds to the reference measurement data set $Data_2$. For each SOBPs 128,000,000 primary protons are simulated and the binning in depth is 0.5 mm. The requested ranges and modulations are listed in Table H.

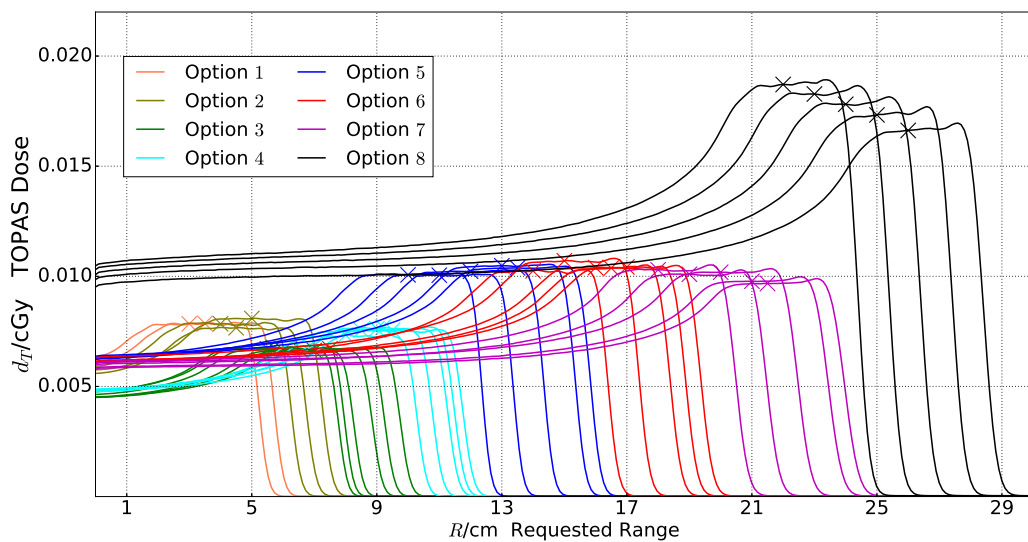


Figure 3.26: Simulated TOPAS SOBPs, that corresponds to the first part of the reference measurement data set $Data_1$ (kindly provided by Dr. Benjamin Lutz), with varying ranges and constant modulation. For each SOBPs 128,000,000 primary protons are simulated and the binning in depth is 0.5 mm. The SOBPs with the same colors belong to the same option. The requested ranges and modulations are listed in Table I.

The simulated depth-dose distributions, which correspond to the reference QA measurements are visualized in Figure 3.25. The corresponding requested ranges, modulations and depth positions of the measured dose calibration points in the water phantom are listed in Table H. The data contains the reference field ($R_{\text{req}} = 16$ cm, $R_{\text{req}} = 10$ cm). The snout position is 10 cm and two square apertures are used (10 cm \times 10 cm) for $R_{\text{req}} \geq 15$ cm. Otherwise, it is one aperture. The OF is calculated by dividing the dose D_{calib} , which is simulated in the water phantom at the calibration depth point, by the simulated deposited dose in the representative IC23 volume D_{IC23} . Therefore, D_{IC23} is transformed into a charge q_{IC23} .

$$\psi = \frac{D_{\text{IC23}}}{q_{\text{IC23}}} \quad (3.14)$$

The reference measurements \mathcal{M}_{Res} , are divided into two parts $\mathcal{M}_{\text{Res}}^1$ and $\mathcal{M}_{\text{Res}}^2$. The first part contains SOBP fields with a constant modulation of $M_{\text{req}} = 4$ cm and varying R_{req} . The second part $\mathcal{M}_{\text{Res}}^2$ contains five different SOBP field series, each with constant R_{req} and varying M_{req} . The snout position is set to 10 cm and two ring apertures (radius $r = 7$ cm) are used. The position of the dose field calibration point in the water phantom corresponds to the requested range reduced by 2 cm. The requested ranges and modulations of $\mathcal{M}_{\text{Res}}^1$ and $\mathcal{M}_{\text{Res}}^2$ are listed in Table J, and in Table I, respectively. To normalize the simulated output factors to the reference field, the ratio α has to be derived, which describes the amount of simulated dose, which corresponds to one MU for each volume, separately. Therefore, one has to equalize the simulated output factors of the volumes to measured one:

$$\psi_{\text{exp}}^{\text{Ref}} = \psi_{\text{sim}}^{\text{Ref}} = \frac{D_{\text{sim}}^{\text{Ref}}}{\text{MU}_{\text{sim}}^{\text{Ref}}} = \frac{D_{\text{sim}}^{\text{Ref}}}{\alpha D_{\text{IC23}}^{\text{Ref}}} = \frac{\psi_{\text{sim},D}^{\text{Ref}}}{\alpha} \rightarrow \alpha = \frac{\psi_{\text{sim},D}^{\text{Ref}}}{\psi_{\text{exp}}^{\text{Ref}}} \quad (3.15)$$

3.2.2 TOPAS Outputfactor Simulations for Patient QA

Patient QA measurements for one patient at UPTD are simulated and the measured output factors are compared to TOPAS simulations. The proton treatment plan contains two treatment fields. Each treatment field is measured at four dose calibration points in the water phantom, which are located at representative field positions. The measurement accuracy of the point determination in depth is $\Delta z \approx 0.3$ mm, and in the lateral dimensions it is $\Delta x|\Delta y \approx 2$ mm. The dose simulations in the IC23 are performed by using the representative volumes, which are described in the previous Sub-section 3.2.1. The parameters of both fields are presented in Table ??.

In the patient QA measurements the same snout position and apertures are used as in the patient treatment. The medical physicists have to apply certain correction factors, to correct uncertainties, which occur due a saturation of the detector k_{S} , the beam polarity k_{P} and the beam quality k_{B} . Those uncertainties do not occur in the Monte-Carlo simulation. In the simulation the air density is assumed to be constant, whereby in reality there are small density fluctuations in the IC2 due air temperature T_{air} and pressure p_{air} changes. Therefore, T_{air} and p_{air} are monitored during each patient QA measurement. The uncertainties of applying the correction factors contribute to the absolute dose measurement uncertainty of 1%. Uncertainties in the determination of the positions of the calibration points contribute to measurement uncertainty, too. The minimal depth uncertainty Δz is 0.2 cm and increases with increasing measurement time, because the on-going vaporization of the water changes

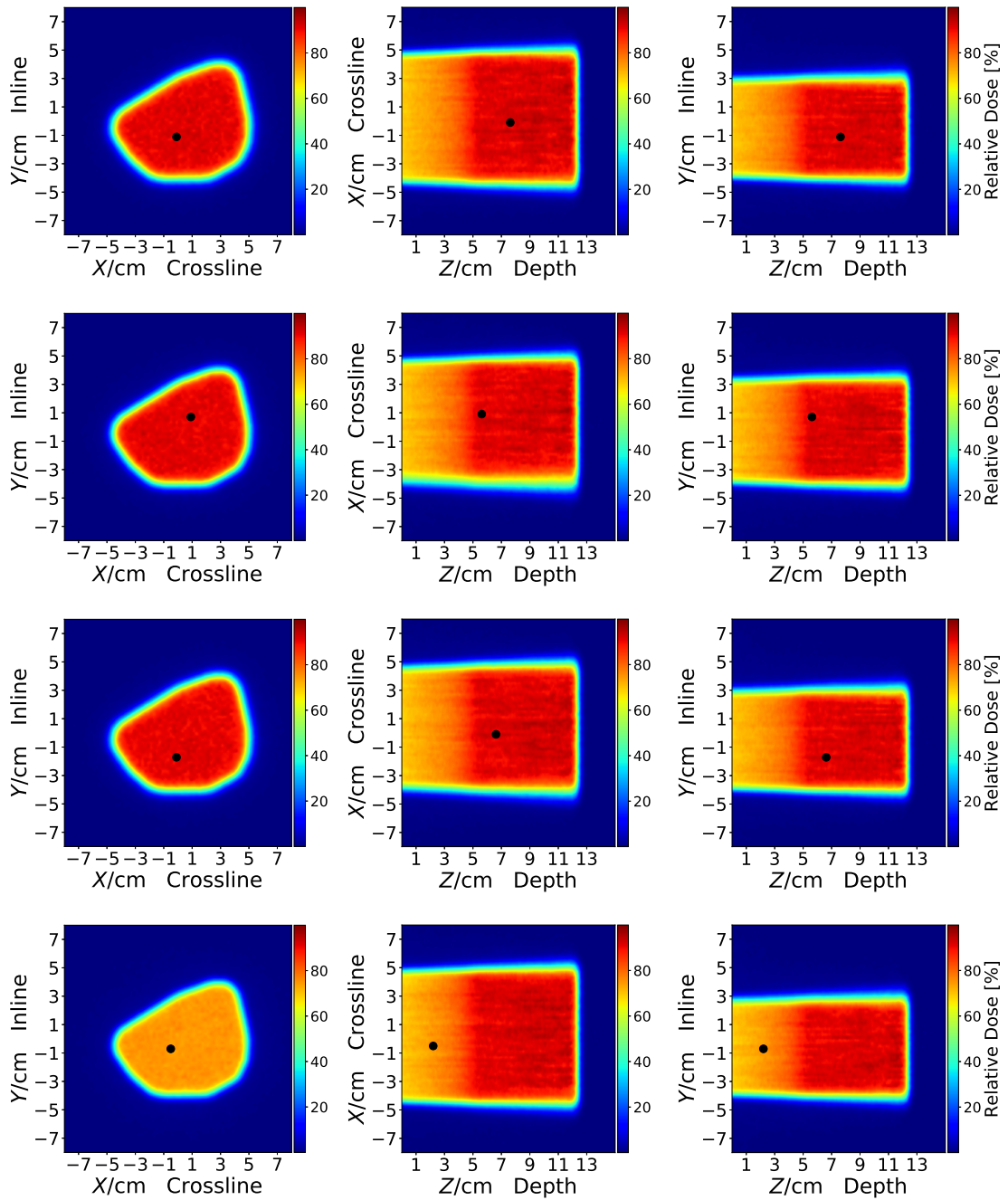


Figure 3.27: Projections XY , XZ , YZ of the four dose distributions in a water phantom, which belong to the measured treatment field Field 1 of Patient1. Each projection contains the position of the dose calibration point, which is used for OF calculations.

the water surface height. The uncertainty of the lateral detector positioning x, y is around 2.5 mm. 1 mm is the accuracy, which a medical physicist is able to position the detector by using control lasers. The other 1.5 mm have to be added, because the lasers are not perfectly in the isocenter. The mean value of the four dose calibration points in the water phantom can be defined as the beam weight W . MU_W describes the mean value of the corresponding monitor units (MU). The field output factor ψ_F is defined as the ratio between W and MU_W .

$$\psi = \frac{W}{MU_W} \quad (3.16)$$

The coordinates of the calibration points are listed in Table 3.4 and visualized in Figure 3.27. The y -axis is also defined as the inline axis, the x -axis is defined as the crossline axis. The isocenter is placed one the water surface. Table 3.4 contains the planned dose, the corresponding MU values and the calculated output factors. The field output factor of each field is derived by calculating the mean value of the two measured output factors, which belong to the central plateau region.

$$\psi_{\text{exp}}^{F_1} = \frac{1}{2} \cdot (\psi_{\text{exp}}^{F_{1.1}} + \psi_{\text{exp}}^{F_{1.2}}) = 8.8822 \text{ cGy/MU} \quad (3.17)$$

$$\psi_{\text{exp}}^{F_2} = \frac{1}{2} \cdot (\psi_{\text{exp}}^{F_{2.1}} + \psi_{\text{exp}}^{F_{2.2}}) = 8.4287 \text{ cGy/MU} \quad (3.18)$$

Table 3.4: Measured parameters of the calibration points, which belong to the two treatment fields of the proton plan of Patient 1.

Field 1	x/cm	y/cm	z_d/cm	z_{eff}/cm	$D_{\text{Plan}}/\text{Gy}$	MU	$\psi_{\text{exp}}/[\text{cGy/MU}]$
	0	-1	8	7.71	0.8700	96.3	9.034
	1	0.8	6	5.71	0.8715	97.3	8.9568
	0	-1.6	7	6.71	0.8508	96.6	8.8075
	-0.5	-0.6	2.5	2.21	0.7483	97.9	7.6435
Field 2	0.5	0	6	5.71	0.8518	100.7	8.4588
	0	-1.4	8	7.71	0.8407	100.1	8.3986
	0	-1	10	9.71	0.8485	99.8	8.5020
	0	-1	2.5	2.21	0.7342	99.4	7.3863

Table 3.5: Requested ranges and modulations and the corresponding snout positions, which belong to the two treatment fields of the proton plan of Patient 1.

	R_{req}/cm	M_{req}/cm	$d_{\text{Snout}}/\text{cm}$
Field 1	12	8	19.1
Field 2	12.7	9.8	23.22

3.3 TOPAS Simulation of a Proton Treatment Plan

The simulation of a full treatment plan in TOPAS requires information, about the CT image geometry, the defined isocenter, the field form ($R_{\text{req}}, M_{\text{req}}$), the snout position, the gantry and table angles and the shape of the patient specific components. The automated reading of a full proton plan is not a

default TOPAS feature yet, and has to be implemented by the user. The medical data is stored in a format, which is called Digital Imaging and COmmunications in Medicine (DICOM). The integration of a proton treatment plan into TOPAS is based on a set of CT image DICOM files (CT-SliceX.dcm) and a plan DICOM file (Plan.dcm). The CT files contain the CT image slices, the plan file contains all plan specific nozzle geometry settings. The simulated dose distribution in the patient is compared with the calculated one, which is stored in a separate DICOM file (Dose.dcm).

3.3.1 Automated Proton Plan Integration into TOPAS

The coordinate systems, which are used in the treatment planning at UPTD are introduced. The CT image integration in TOPAS is described including the accurate positioning of the image in the TOPAS coordinate system. The adjustment of the nozzle settings and the patient specific geometries based on the treatment plan information is further characterized.

There are different coordinate systems at UPTD. The so-called patient coordinate system is the default one, which is used in the DICOM format style. The CT images and the planned dose images are stored in the patient coordinate system. In the treatment planning system (XIO), a so-called planing coordinate system is used. The planning system differs from the patient one (CT system) by a 90° rotation (\mathcal{M}_{Rot}) and is used as the default system in TOPAS. Therefore, the CT image in TOPAS is moved until the isocenter of the proton plan falls together with the origin of ordinates of the TOPAS world. In the so-called gantry coordinate system, the z -axis is always align in negative beam direction. In

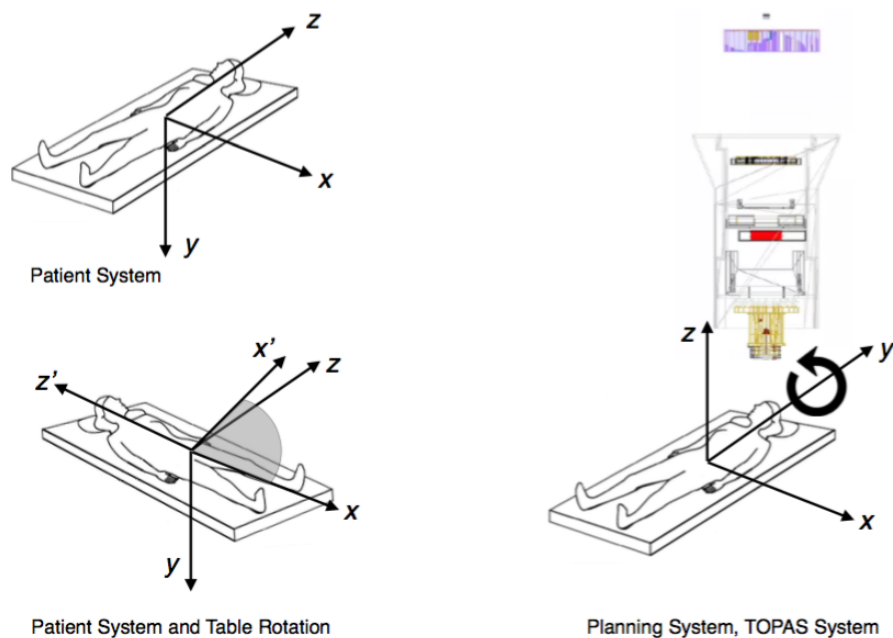


Figure 3.28: Illustration of the patient and planning coordinate system at UPTD. In addition, a table rotation in the patient system is illustrated.

default nozzle position, with the gantry angle equals zero (Θ_{Gantry}). the gantry and patient system are identical. Figure 3.28 visualizes the patient and the planning system. In addition, one table rotation in the patient system is illustrated. The differences of the coordinate systems are summarized in Table 3.6.

The integration of a CT image in a Monte-Carlo simulation requires an accurate transformation of the HU units into electron densities. In TOPAS, the so-called Schneider convention is applied [45]. The CT images are generated by using a dual-energy CT at UPTD [46]. By default the CT box is centered in TOPAS in his own CT coordinate system ($v_{0,CT}$). To adjust the CT box correctly it has to be rotated around the x -axis (which is invariant in CT and patient coordinate system) by a rotation matrix \mathcal{M}_{Rot} and translated by a translation vector \hat{v}_{trans} . In TOPAS, the rotation of the CT box is applied by defining the rotation angles of the box geometry (RotX=90°, RotY=0°, RotZ=0°). The box translation vector $\hat{v}_{Trans, CT} = (TransX, TransY, TransZ)$ has to be set in TOPAS coordinates. Vectors with a hat are defined in TOPAS coordinate system, vectors without a hat are defined in the patient coordinate system. \hat{v}_{HL} is the connection vector from the center of the CT box, to the upper left corner in TOPAS coordinates. First, the CT geometry is shifted to ensure, that the upper left corner of the box is similar to the corner coordinates $v_{CT,Corner} = (ImPosX, ImPosY, SliceLoc0)$. The corner coordinates are stored in each CT file. SliceLoc0 is the slice location of the CT slice, with the smallest z value in patient coordinates. The CT image contains the patient table. The CT image coordinates (ImPosX, ImPosY) do not include the table geometry. Therefore, in TOPAS the box has to be shifted by a table vector v_{Table} . The information about the isocenter of the proton plan is stored in a plan DICOM file ("Plan.dcm") in patient coordinates. Therefore, the CT box has to be shifted in the opposite direction.

$$\mathcal{M}_{Rot} = \begin{pmatrix} 1 & 0 & 0 \\ 0 & \cos(90^\circ) & -\sin(90^\circ) \\ 0 & \sin(90^\circ) & \cos(90^\circ) \end{pmatrix} = \begin{pmatrix} 1 & 0 & 0 \\ 0 & 0 & -1 \\ 0 & 1 & 0 \end{pmatrix} \quad (3.19)$$

$$\hat{v}_1 = \hat{v}_{HL} - \hat{v}_{CT,Corner} = \hat{v}_{HL} - \mathcal{M}_{Rot} \otimes v_{CT,Corner} \quad (3.20)$$

$$\hat{v}_{2,CT} = \hat{v}_{0,CT} + \hat{v}_1 = \mathcal{M}_{Rot} \otimes v_{0,CT} + \hat{v}_1 \quad (3.21)$$

$$\hat{v}_{3,CT} = \hat{v}_{2,CT} + \hat{v}_{Table} = \hat{v}_{2,CT} + \mathcal{M}_{Rot} \otimes v_{Table} \quad (3.22)$$

$$\hat{v}_{4,CT} = \hat{v}_{3,CT} - \hat{v}_{Iso} = \hat{v}_{3,CT} - \mathcal{M}_{Rot} \otimes v_{Iso} \quad (3.23)$$

$$\hat{v}_{Trans, CT} = \hat{v}_{4,CT} - \hat{v}_{0,CT} = \hat{v}_{HL} + \mathcal{M}_{Rot} \otimes [-v_{CT,Corner} - v_{Iso} + v_{Table}] \quad (3.24)$$

Equation (3.25) shows how to define the box translation (TransX, TransY, TransZ) in planning coordinates in TOPAS, based on the initial input parameters, which are defined in patient coordinates. (HLX, HLY, HLZ) define the half lengths of the patient CT box in x, y, z -dimension.

$$\begin{pmatrix} TransX \\ TransY \\ TransZ \end{pmatrix} = \begin{pmatrix} HLX \\ HLY \\ HLZ \end{pmatrix} + \begin{pmatrix} 1 & 0 & 0 \\ 0 & 0 & -1 \\ 0 & 1 & 0 \end{pmatrix} \otimes \left[- \begin{pmatrix} ImPosX \\ ImPosY \\ SliceLoc0 \end{pmatrix} - \begin{pmatrix} IsoX \\ IsoY \\ IsoZ \end{pmatrix} + \begin{pmatrix} 0 \\ -10 \text{ cm} \\ 0 \end{pmatrix} \right] \quad (3.25)$$

Besides the information about the isocenter, the plan DICOM-file contains information about the field shape, the snout position, the gantry and table angles and the aperture and compensator geometries. The snout position is set by a single command in the TOPAS model of the IBA nozzle. The gantry rotation is applied by rotating the nozzle geometry around the y -axis of the world geometry. To apply table rotations in TOPAS a mother volume has to be defined, which has its center at the isocenter position. This is necessary, because TOPAS allows box rotation only relative to the box center. The

table angles are the rotation parameters (RotX, RotY, RotZ) of the mother volume. The aperture and compensator coordinates ($X|Y$) in the plan-DICOM are defined in the isocenter plain. They have to be transformed to their real positions in the snout. Therefore, the information about the virtual source to axis ($VS_x|VS_y$), the aperture-source distance s_{AP} and the compensator-source distance s_{CO} are extracted from the plan DICOM. By using the intercept theorem the new coordinates ($X'|Y'$) of the AP and CP are derived.

$$X'_{AP} = \frac{VS_x - s_{AP}}{VS_x} \cdot X_{AP} \quad Y'_{AP} = \frac{VS_y - s_{AP}}{VS_y} \cdot Y_{AP} \quad (3.26)$$

$$X'_{CO} = \frac{VS_x - s_{CO}}{VS_x} \cdot X_{CO} \quad Y'_{CO} = \frac{VS_y - s_{CO}}{VS_y} \cdot Y_{CO} \quad (3.27)$$

All required information, which are necessary to construct the patient specific components in TOPAS are listed in Table 3.7. The implementation of patient specific components into TOPAS is further described Ref. [39]. For one aperture and compensator the implementation of the corresponding TOPAS models is commissioned [29], by using milling machine input files, which are generated by milling machine software based on the plan DICOM. Those input files are reproduced by the implemented automated DICOM reading software, which is used in this thesis. Table 3.7 summarizes all CT and plan parameters, which are required to implement the simulation of proton treatment plans in TOPAS.

3.3.2 Dose Simulations in a Patient CT

For one proton treatment plan (brain tumor, two treatment fields), the dose distributions are simulated in the patient CT. The TOPAS dose distribution is compared to planned dose distribution, which is stored in the DICOM standard. Deviations, in the spatial shape in the absolute doses are analyzed.

The dose is simulated in the CT image with a spatial resolution of $res_{x|y|z} = 2$ mm. This resolution correspond to the one, which are used in the planned dose grids. A higher TOPAS dose resolution can further increase dose accuracy, but requires more computation time. The coordinate system and the DICOM tags, which contains the information about the grid position are the same as used in the CT DICOM files. In addition, the planned dose DICOM contains a scaling factor, to scale the dose grid values to absolute doses in gray. The brain tumor patient is selected because of the absence of large density gradients in the target volume. Therefore, the dose deviations between Monte-Carlo and the TPS are expected to be small, and the treatment plan can be used to validate TOPAS. If there are deviations between the TOPAS stopping powers of the CT tissue materials and the ones, which are used in the TPS, an unbiased comparison between the simulated and planned dose distributions would be impossible. There are 3996 CT materials (and HU), each corresponds to a specific superposition of 25 tissue base materials. The TPS at UPTD uses a measured stopping power to material conversion function as illustrated in Figure 3.31 [46]. The stopping powers of the CT tissue materials in TOPAS are corrected by slightly adjusting the material densities. The corrected and uncorrected distributions of the stopping powers and relative mass densities of the 3996 CT materials are visualized in Figure 3.31 and Figure 3.32.

Table 3.6: Coordinate Systems, which are used at UPTD.

Coordinate System	x -axis	y -axis	z -axis
Patient/CT System	lateral	dorsal	cranial
Gantry System	angle dependent	cranial	angle dependent
Planning System	lateral	cranial	opposite dorsal

Table 3.7: Parameters, which have to be extracted out of a proton plan and a CT image DICOM file in order to implement an automated proton plan integration in TOPAS.

CT-DICOM	Image Geometry	
	Pixel Array (0020,1041)	Number of Frames (0028,0008)
	Pixel Spacing (0028,0030)	Slice Thickness (0018,0050)
	Rows (0028,0010)	Columns (0028,0011)
	Image Position	
	Image Position (0020,0032)	Image Orientation (0020,0032)
	Slice Location (0020,1041)	
Plan-DICOM	Field Shape	
	Range (300b,1004)	Modulation (300b,100e)
	Positions	
	Snout Position (300a,030d)	Isocenter Position (300a,012c)
	Angles	
	Gantry Angle(300a,011e)	GantryPitchAngle (300a,014a)
	TableTopPitchAngle (300a,0140)	TableTopRollAngle (300a,0144)
	Aperture	
	Thickness (300a,0100)	Number of Points (300a,0104)
	Block Data XY (300a,0106)	Distance to Iso (300a,00f7)
	Compensator	
	Rows (300a,00e7)	Columns (300a,00e8)
	Pixel Spacing (300a,00e9)	Position (300a,00ea)
	Thickness (300a,00ec)	Milling Tool Diameter (300a,02e8)
	Column Offset (300a,02e5)	Distance to Iso (300a,02e4)
Virtual Source		
	Virtual Source (300a,030a)	

Table 3.8: Dose and CT image parameters for Patient 1 (brain). The image position $ImPos$ describes the coordinates of the upper left image corner, which belong to the CT slice with the smallest slice location value.

	XYZ Bins	XYZ Pixel/mm	XYZ Size/mm	XYZ ImPos/mm
CT	(512, 512, 104)	(0.98, 0.98, 2)	(500, 500, 208)	(-249.51, -349.51, -122.0)
PlanDose	(96, 151, 104)	(2, 2, 2)	(192, 302, 208)	(-91.1, -217.3, -122.9)

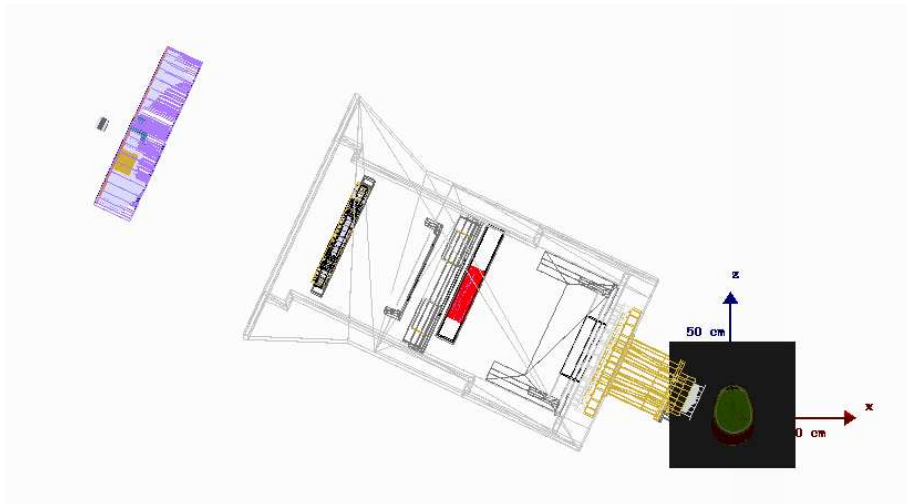


Figure 3.29: Illustration of the geometrical setup in TOPAS, which belong to the first field of the proton plan for Patient1. The gantry angle is $\Theta_{Gantry} = -295^\circ$ and the snout position $d_{pos} = 19.1$ cm.

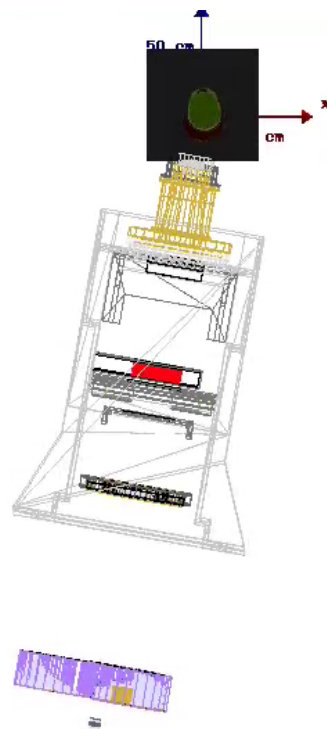


Figure 3.30: Illustration of the geometrical setup in TOPAS, which belong to the first field of the proton plan for Patient1. The gantry angle is $\Theta_{Gantry} = -190^\circ$ and the snout position $d_{pos} = 23.22$ cm.

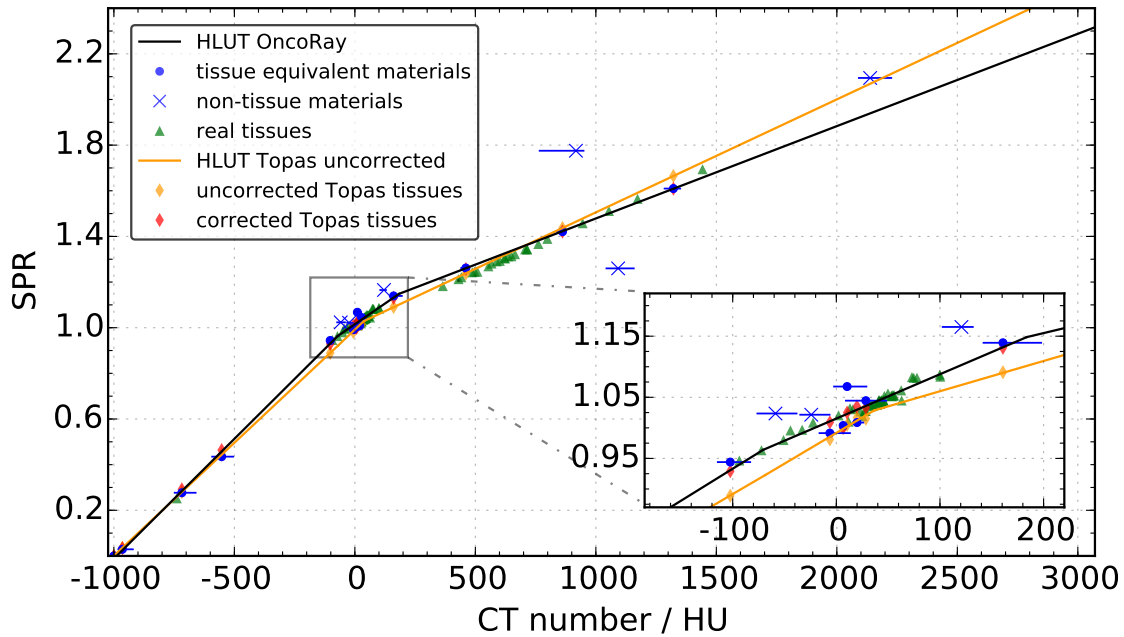


Figure 3.31: Stopping power distribution for the 3996 CT materials (Schneider convention [45]), which is implemented in the treatment planning system at UPTD (HLUT OncoRay) and in TOPAS (corrected TOPAS tissues). The curves are derived in measurements with a dual-energy CT [46].

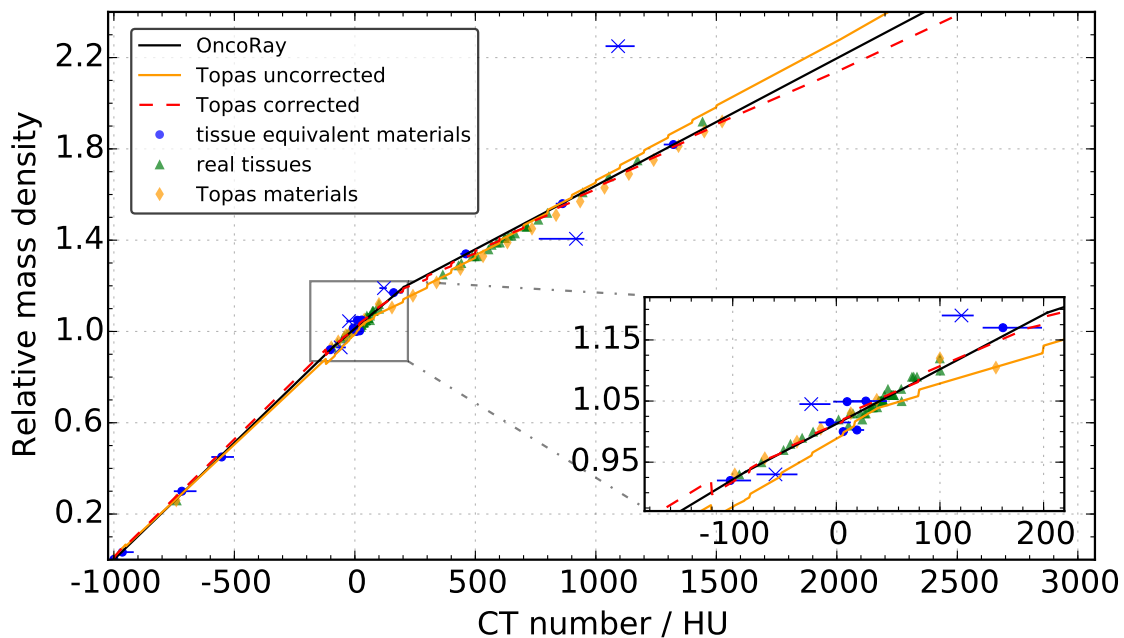


Figure 3.32: Relative mass densities of the 3996 CT materials (Schneider convention [45]), which is used at UPTD (OncoRay) and in TOPAS (TOPAS corrected). The curves are derived in measurements with a dual-energy CT [46].

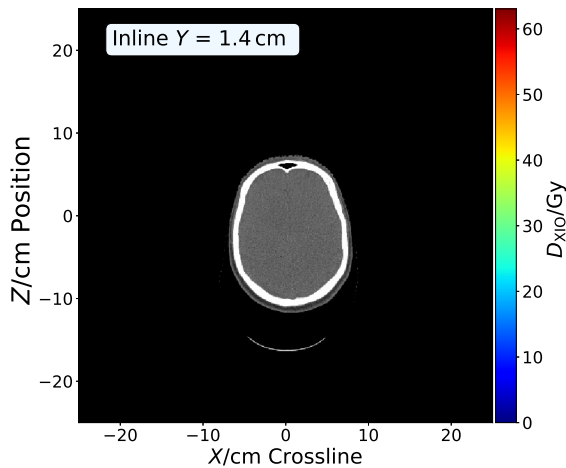


Figure 3.33: One CT image slice, which belongs to Patient 1. The image is generated at UPTD by using a dual energy CT.

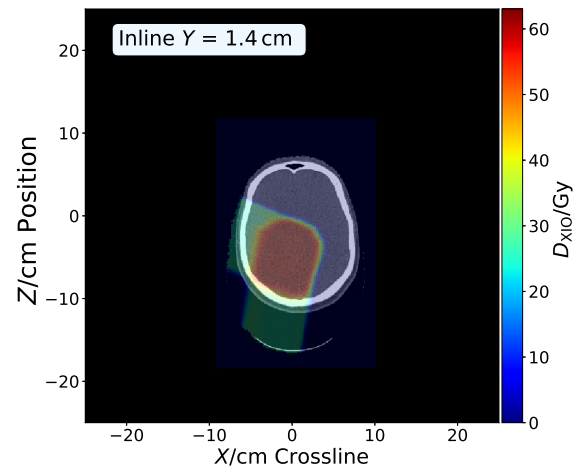


Figure 3.34: One CT image slice and the corresponding planned dose image which belongs to Patient 1. The planned dose is generated by the treatment planning system XIO..

In Radiotherapy, doses are conventionally reported as the water-equivalent dose (dose to water). This can be explained by the fact, that pencil-beam dose calculation algorithms model the human tissue as water with varying density. The physical dose deposition, D_m dose to medium, as modeled using the Monte Carlo method, has to be converted into dose to water D_w .

$$D_w = D_m \frac{\rho_w^2 S_w}{\rho_m^2 S_m} \quad (3.28)$$

TOPAS allows to simulate both, D_m and D_w in a patient CT. The absolute dose is calculated by using the simulated field output factors of the two treatment fields ($\psi_{sim}^{F,1}$, $\psi_{sim}^{F,2}$), which belong to the proton plan of Patient 1. The α ratio of the reference field is used to transform the simulated dose in the TOPAS ion chamber into a MU signal.

By using the parameter α one is able to transform the simulated dose in the TOPAS IC23 from Gy into MU units. Therefore, one can derive the absolute dose of the field F in the high dose region W. To transform the simulated relative dose D_{sim}^{rel} to an absolute dose it has to be normalized to its high dose region by the factor D_{sim}^{norm} .

$$MU_{sim}^F = \alpha \cdot D_{sim,IC23}^F \quad D_{sim}^W = MU_{sim}^F \cdot \psi_{sim}^F \quad D_{sim}^{abs} = D_{sim}^W \cdot \frac{D_{sim}^{rel}}{D_{sim}^{norm}} \quad (3.29)$$

If the treatment plans contains N fields, each with a beam weight w_i , the absolute dose is the weighted sum of the single field doses.

$$D_{abs} = \sum_i^N w_i \cdot D_{sim_i} \quad (3.30)$$

To compare the planned and the simulated dose distributions a technique, which is called gamma analyze, is applied [47]. This technique is widely used in the clinical routine to describe the deviation

of two images in one single parameter, the so called gamma pass rate (GPR). If the GPR is above 95 % the images are considered as similar, within clinical tolerances. A gamma analysis considers geometrical and dose deviations, when comparing two dose distributions. To determine the accuracy of an image voxel the doses of neighboring voxels are taken into account. The geometrical criterion $\lambda_{x,y,z}$, defines, how many neighboring values in the surrounding voxel area are considered. The dose criterion λ_D defines the tolerable voxel dose uncertainties. Usually, a dose threshold criterion λ_{Th} is defined and voxel values below this threshold are not considered in the gamma analysis. Depending on the question of interest, different combinations of $\lambda_{x,y,z}$, λ_D and λ_{Th} are defined as the gamma criteria.

3.3.3 LET Simulation and RBE Calculation in a Patient CT

The dose averaged LET is simulated in Patient 1 . The RBE is calculated in both patients based on the Wendenberg model. Hot spots of the relative biological effectiveness are characterized. TOPAS

Table 3.9: Input parameters of the RBE model, which is used to derive the RBE distribution for Patient 1. α_x and β_x belong to a glioma.

Input Parameter	λ	α_x	β_x
Value	0.0127	0.11	0.06

version 3 provides a dose- and a fluence averaged LET scorer, which scores the LET of primary and secondary protons, including the energy deposited by associated secondary electrons. A step-by-step upper cut-off of 100 MeV/mm/(g/cm³) is set, such that steps contributing greater than this value are not be scored. The electron production threshold is defined as 0.05 mm [39]. In low density materials like air, the mean path length between discrete processes can exceed the voxel size. In those materials the proton LET scorer would give values, which are too high. In addition rare events, that produce low energy protons can cause LET spikes, too. As these are rare events those problems would not occur in a fluence averaged LET scorer. Therefore the TOPAS developers introduced a parameter, that allows to switch from dose-averaged to fluence-averaged LET, if the material density falls below a certain threshold. In both patients the threshold is set to 0.05 g/cm³. If a treatment plan contains N fields, each with a certain weight w_i , the LET has to be averaged by the dose distributions of the single treatment fields.

$$D_{\text{abs}} = \frac{\sum_i^N w_i \cdot D_{\text{sim}_i} \text{LET}_i}{\sum_i^N \lambda_i \cdot D_{\text{sim}_i}} \quad (3.31)$$

The distribution of the relative biological effectiveness is calculated by using a model, which is illustrated in Ref. [22]. The model assumes a constant β parameter. α_p is a function of α_x and the LET.

$$\alpha_p = \alpha_x + \lambda \text{LET} \quad \beta_p = \beta_x \quad (3.32)$$

$$\text{RBE} = \left((\alpha_x^2 + 4\beta_x d_p (\alpha_p + \beta_x d_p))^{1/2} - \alpha_x \right) / (2\beta_x d_p) \quad (3.33)$$

α_x and β_x are the coefficients of the LQ-model, which belong to the reference photon irradiation. d_p is the dose, which is deposited in one single fraction. The values of the model input parameters are presented in Table 3.9. The coefficients α_x and β_x belong to a glioma. By convention [48] the RBE weighted dose is written in the following form:

$$D_{\text{RBE, TOPAS}} / \text{Gy(RBE)} \quad D_{\text{RBE, XiO}} / \text{Gy(RBE)} \quad (3.34)$$

4 Results

The finally adjusted beam source parameters are presented. The simulated depth-dose distributions are visualized, which are generated by using the optimized beam source parameters and beam current modulations. Deviations between the adjusted depth-dose and lateral dose distributions are characterized for different regions, separately. The measured and simulated output factors are compared by describing the distribution of the relative error of the simulated output factors for different measured data sets. The absolute TOPAS dose distribution of the simulated proton plan is compared to the planned dose distribution, by showing dose difference distributions and performing gamma analyzes. Finally, simulated linear energy transfer (LET) distributions are presented together with variable relative biological effectiveness (RBE) distributions in the patient.

4.1 Adjustment and Validation of TOPAS Dose Distributions

In a first step the results of the adjustment of the beam source are presented (beam energy spread and range). Those adjustments are used to derive the optimal beam current modulation weights in TOPAS. In a second step the depth-dose curve simulations with adjusted beam source parameters and beam current modulations are illustrated. The deviations between the simulated and measured depth-dose distributions are characterized for the plateau, distal fall-off and proximal shoulder regions, separately. Besides the validation data depth-dose distributions, the reference data distributions are simulated with the adjustments to quantify correlations between the adjusted parameters. Finally, deviations between the measured and simulated lateral profiles are illustrated. The relative dose deviations are characterized for the lateral plateau region and the profile flanks, separately.

The adjustment of the beam energy spread (BES) distribution $BES(R_{req})$ is presented in Figure 4.1. The BES, which is the relative standard deviation of the beam energy spectrum ($\sigma_{E,rel}$), decreases linearly with increasing range. By using the initial beam energy E one can derive the absolute standard deviation of the energy distribution $\sigma_{E,abs}$. The resulting parameters of the initial beam energy distribution are presented in Figure 4.2 for the full nozzle range interval. Within an option $\sigma_{E,abs}$ stays approximately constant, while E increases linearly and $\sigma_{E,rel}$ decreases linearly. The three jumps, which are observed in the $E(R_{req})$ distribution are present in the $BES(R_{req})$ distribution, too. The sharpness of the initial energy distribution increases with increasing range, but stays approximately constant within an option. $BES(R_{req})$ is linearly interpolated and in TOPAS the optimal BES values are selected from this interpolation line for arbitrary requested ranges. The mean option range offsets between simulated and measured first pristine Bragg peaks are ≤ 2 mm, when using the adjusted first scatterer foil thicknesses from the IBA (ion beam applications) measurements. The offset variances

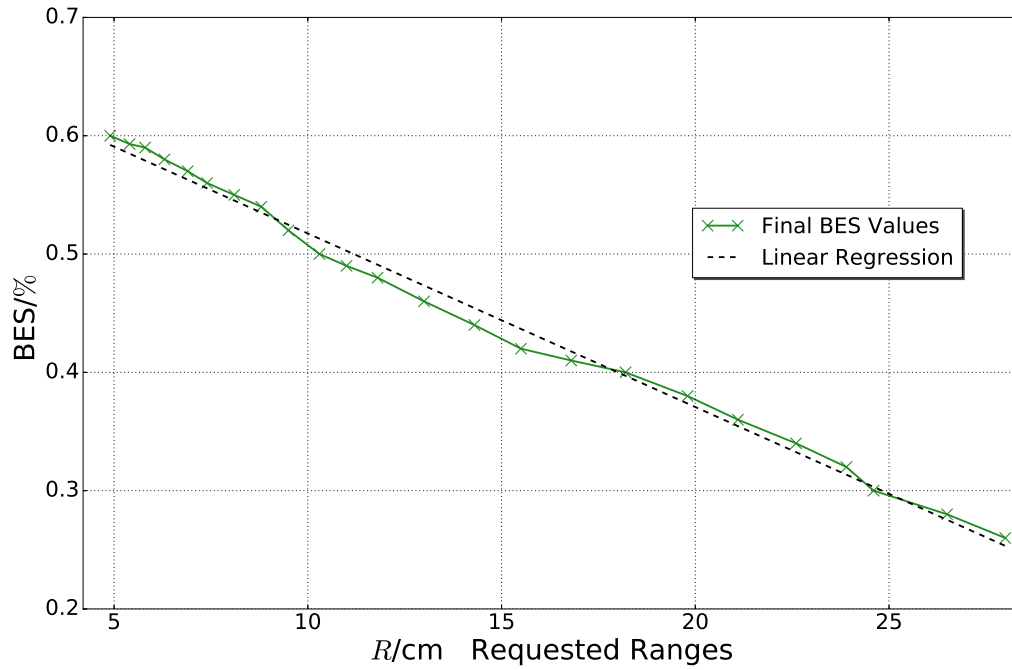


Figure 4.1: Adjusted beam energy spread distribution (green) of the beam source in TOPAS for all nozzle options. The curve is derived by minimizing the deviations between simulated and measured (reference data) fall-off offsets of the first pristine Bragg peaks ΔR_{90} , ΔR_{80} and ΔR_{20} .

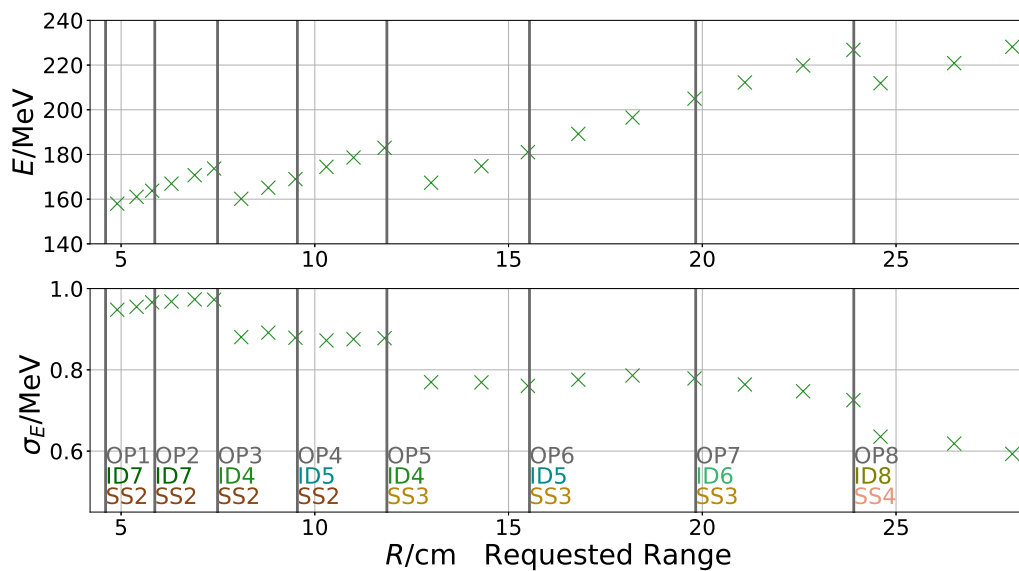


Figure 4.2: Initial beam energy E_{initial} (top) and the absolute standard deviation $\sigma_{E,\text{abs}}$ (bottom) for the full nozzle range interval. The lateral is derived by using the $BES(R_{\text{req}})$ distribution, which is illustrated in Figure 4.1.

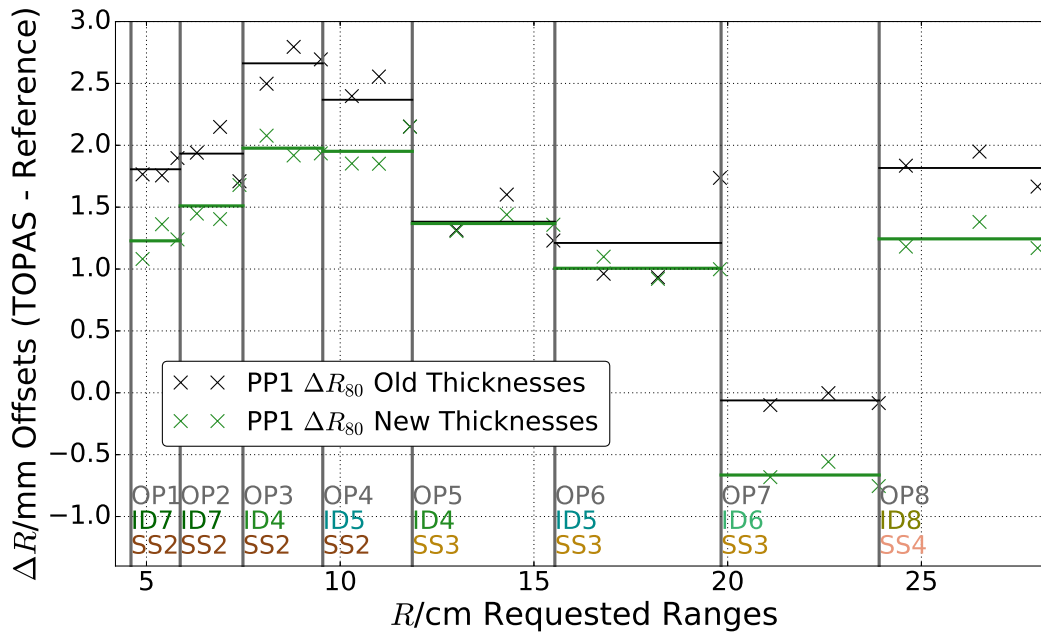


Figure 4.3: Range differences between the simulated and measured (reference data) first pristine Bragg peaks (PP1) for all nozzle options, including the option mean values. The black points are derived by using the first scatterer foil thicknesses from the IBA construction data (old). The green points are calculated by using foil thicknesses, which belong to IBA measurements at UPTD (new).

within an option are ≤ 0.26 mm. This justifies the implementation of an option dependent range offset. IBA applied range corrections in the order of 2 mm during the nozzle commissioning, too. The offsets, which belong to the 24 requested ranges of the reference measurement data \mathcal{D}_{Ref} are visualized in Figure 4.3 including the option mean offsets. Table 4.1 lists the option mean offsets and variances (μ_{new} , ν_{new}) of the data, which is generated by using the adjusted (new) first scatterer foil thicknesses, and the values which are derived by using the foil thicknesses according to the construction drawings (μ_{old} , ν_{old}).

Table 4.1: List of calculated mean option offsets μ and the corresponding standard deviations within an option σ .

Option	μ_{old} [mm]	μ_{new} [mm]	$\Delta\mu$ [mm]	ν_{old} [mm]	ν_{new} [mm]	$\Delta\nu$ [mm]
1	1.8	1.2	0.6	0.114	0.19	-0.076
2	1.9	1.5	0.4	0.333	0.202	0.131
3	2.7	2.0	0.7	0.217	0.13	0.087
4	2.4	1.9	0.5	0.274	0.257	0.017
5	1.4	1.4	0.0	0.283	0.095	0.188
6	1.2	1.0	0.2	0.63	0.126	0.504
7	-0.1	-0.7	-0.6	0.09	0.152	-0.062
8	1.8	1.2	0.6	0.232	0.173	0.059

The derived BES values and option dependent energy shifts are used to optimize the beam current intensity within every nozzle sub-option. The resulting depth-dose curves are compared to the measured

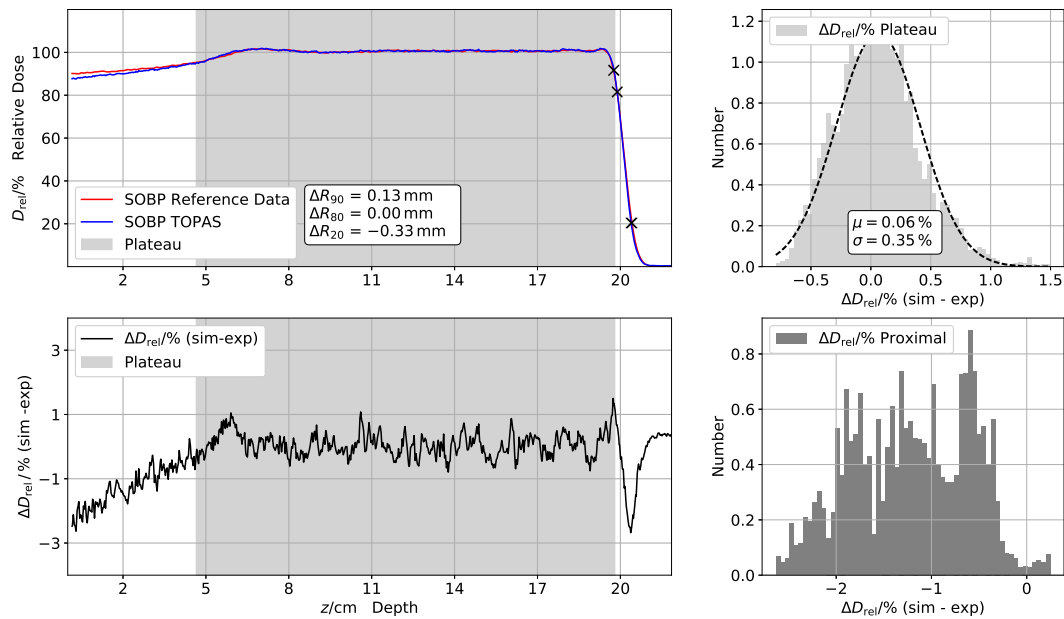


Figure 4.4: Comparison of a simulated (adjusted) and measured (reference) depth-dose curve ($R_{\text{req}} = 19.8$ cm, $M_{\text{req}} = 17.0$ cm, $BES = 0.38$). The range offsets at the distal fall-off region (upper right), the dose difference (sim - exp) distribution (lower right) and two difference histograms at the plateau (upper left) and the proximal shoulder (lower left) region are shown. The plateau histogram is fitted by a Gaussian and the mean value and standard deviation are derived.

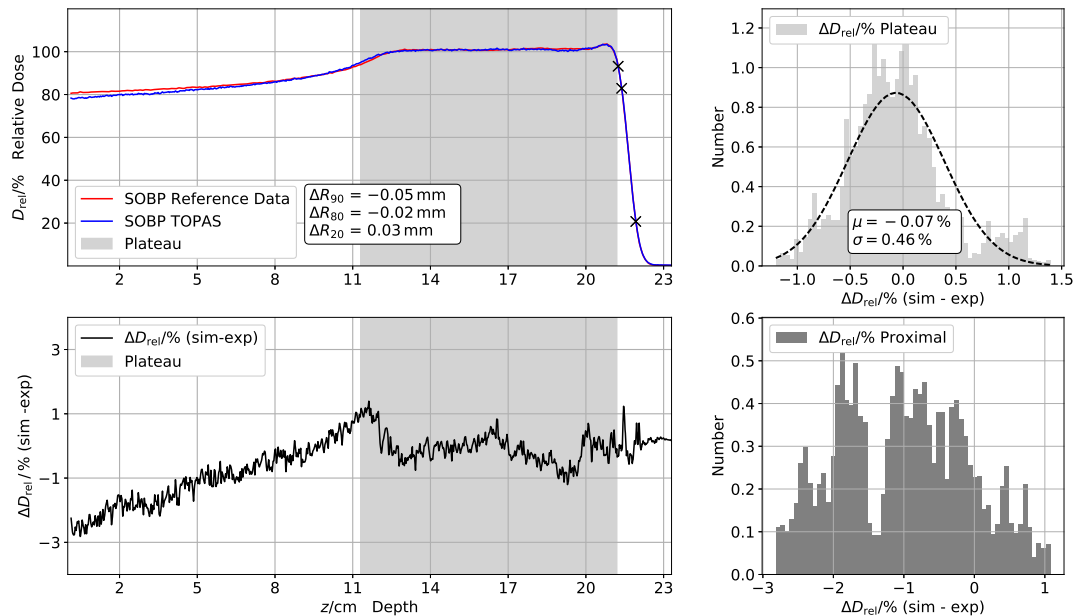


Figure 4.5: Comparison of simulated (adjusted) and measured (validation) depth-dose curve ($R_{\text{req}} = 21.2$ cm, $M_{\text{req}} = 11.5$ cm, $BES = 0.353$). The range offsets at the distal fall-off region (upper right), the dose difference (sim - exp) distribution (lower right) and two difference histograms at the plateau (upper left) and the proximal shoulder (lower left) region are shown. The plateau histogram is fitted by a Gaussian and the mean value and standard deviation are derived.

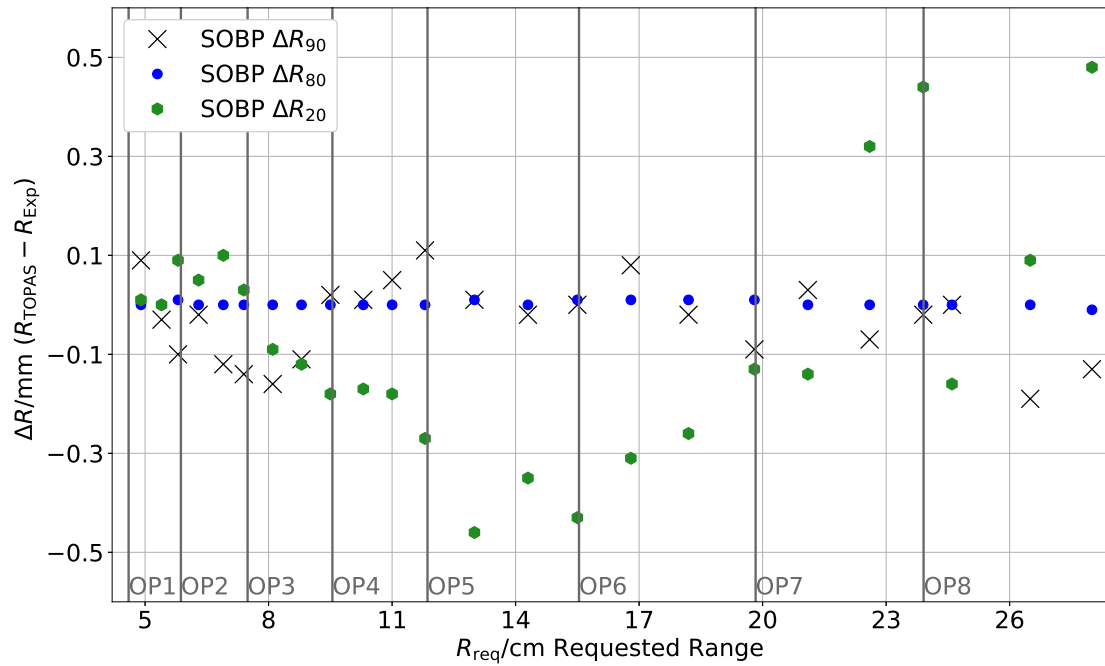


Figure 4.6: SOBP fall-off offsets ΔR_{90} , ΔR_{80} , ΔR_{20} between all reference data SOBPs and TOPAS ones, including all IBA options and mean option offset values.

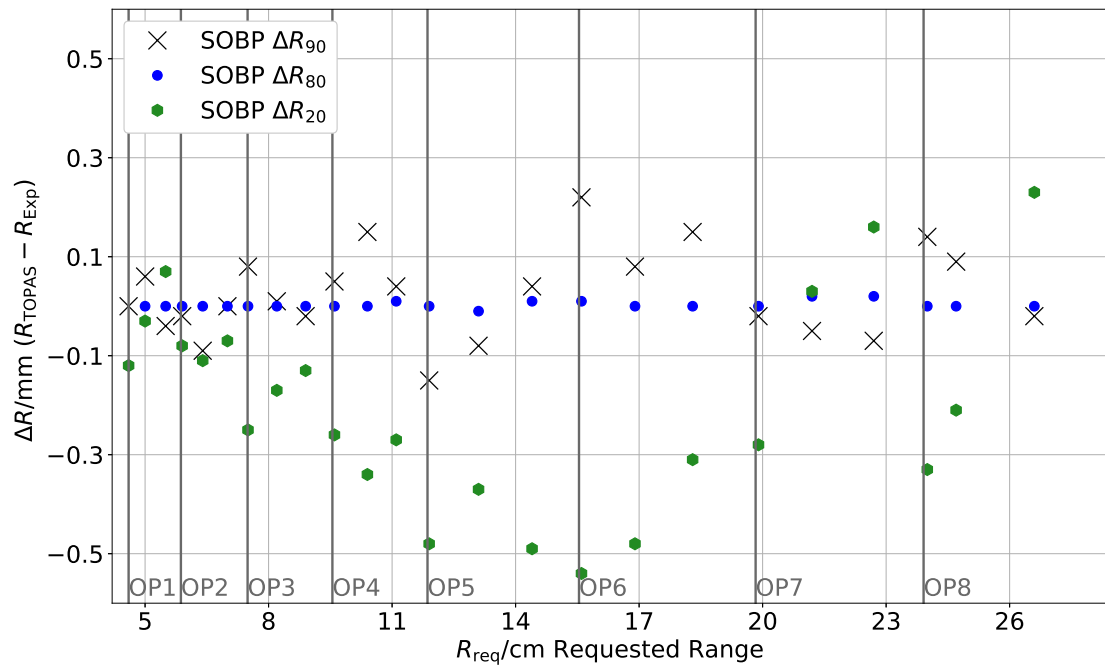


Figure 4.7: SOBP fall-off offsets ΔR_{90} , ΔR_{80} , ΔR_{20} between all validation data SOBPs and TOPAS ones including all IBA options and mean option offset values.

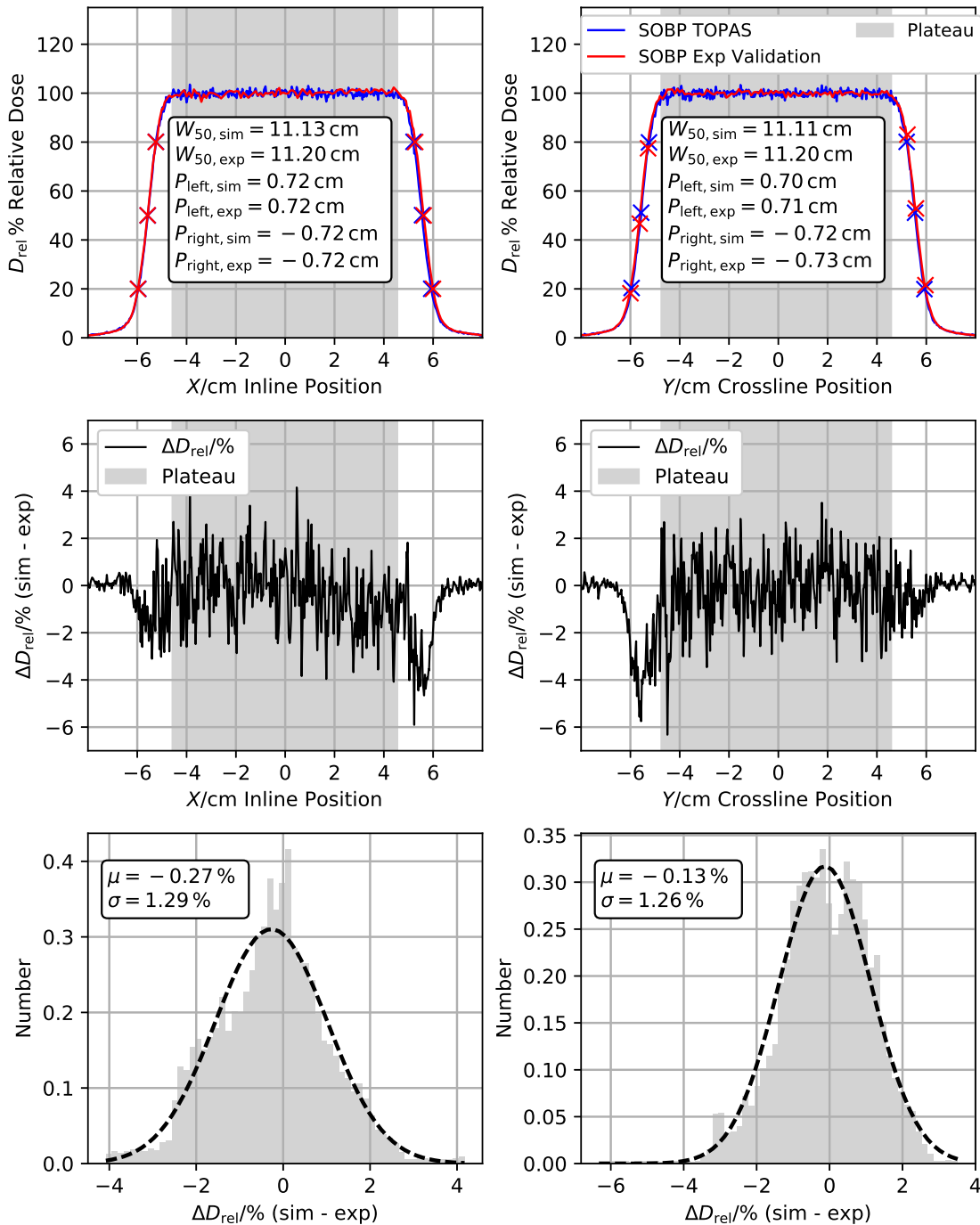


Figure 4.8: Comparison of simulated (adjusted) and measured lateral curves in x-projection (left) and y-projection (right). The profiles belong to SOBP fields ($R_{req} = 21.2 \text{ cm}$, $M_{req} = 11.5 \text{ cm}$, $BES = 0.353$), which are compared at depth position $z_{pos} = 15.5$. The profiles flanks are compared by analyzing the deviations in the lateral widths (W_{50}) and the lateral penumbras ($P_{left} = w_{80, left} - w_{20, left}$, $P_{right} = w_{80, right} - w_{20, right}$). The plateau regions are compared by fitting the relative dose difference distribution with a Gaussian and deriving μ and σ . For the simulations of the lateral profiles two square apertures ($10 \text{ cm} \times 10 \text{ cm}$) are used. The snout position is $d_{pos} = 10 \text{ cm}$.

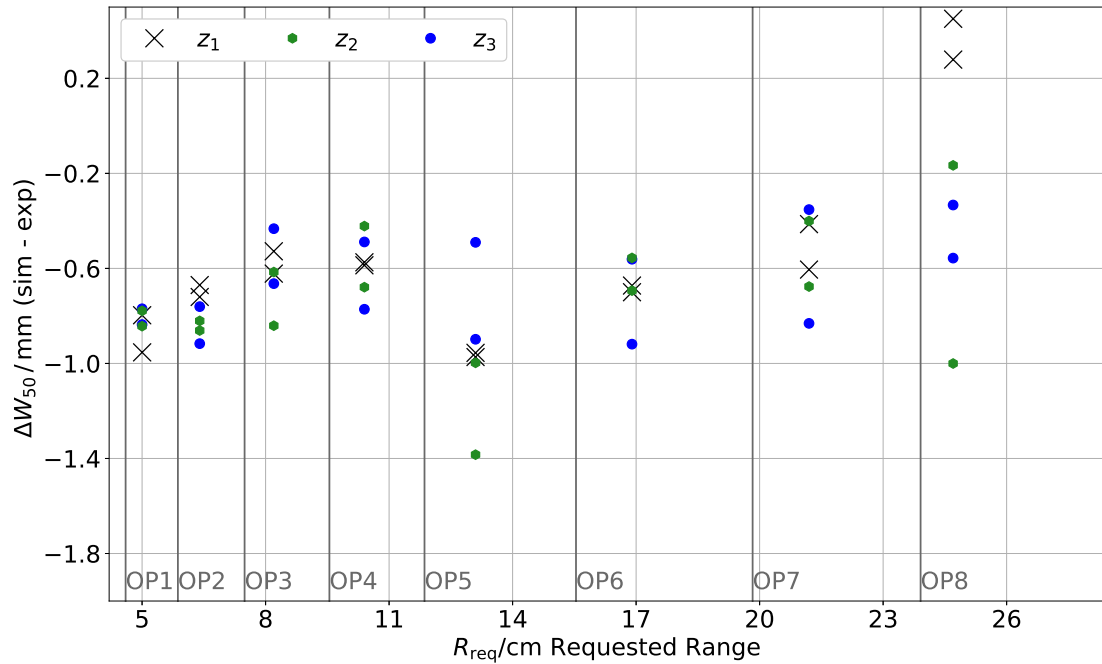


Figure 4.9: Field size deviations of the between the simulated and measured validation data lateral profiles in x-projection. The blue points correspond to the lateral profiles, with the smallest depth position z_1 , the black ones define the profiles with the largest depth position z_3 . The depth positions of the lateral profiles, which belong to the green points, lie in between z_1 and z_2 .

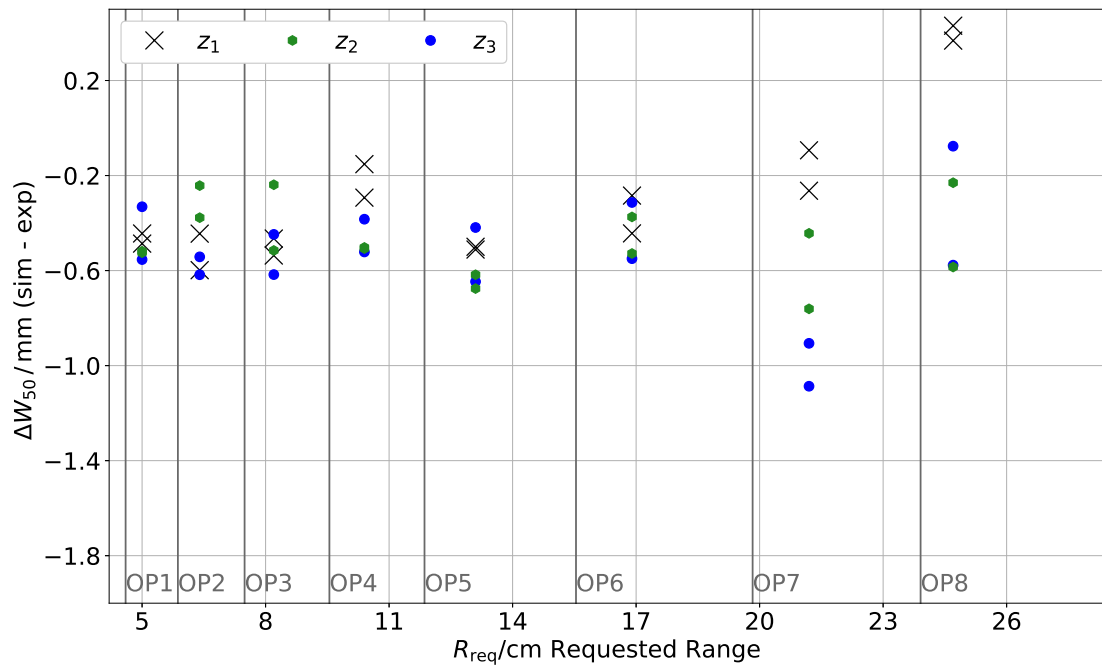


Figure 4.10: Field size deviations of the between the simulated and measured validation data lateral profiles in y-projection. The blue points correspond to the lateral profiles, with the smallest depth position z_1 , the black ones define the profiles with the largest depth position z_3 . The depth positions of the lateral profiles, which belong to the green points, lie in between z_1 and z_2 .

ones by analyzing deviations of the R_{90} , R_{80} and R_{20} at the distal fall-off region and by calculating the dose difference distribution in the central plateau region. The difference distribution is fitted by a Gaussian and the mean value μ_D and the standard deviation σ_D is derived. σ is a benchmark for the error between the simulated and the measured plateau doses. The distal region is not included in the calculation of the difference distribution, because small depth uncertainties contributes largely to uncertainties in the relative dose. The proximal shoulder region is excluded, because in the TOPAS simulations of the depth-dose curves two ring apertures ($R_{\text{inner}} = 8.46$ cm) are implemented, whereby in the reference and validation measurements two square apertures (10 cm \times 10 cm) are used. Near field scattering effects of the apertures have an influence on the proximal shoulder region of a SOBP. Therefore, an unbiased comparison between the simulation and measurement at the proximal shoulder region is not possible.

Figure 4.4 and Figure 4.5 illustrate the comparison of a simulated and measured depth-dose distribution, which belong to the reference data (top) and the valid data (bottom). The adjusted reference data are simulated to quantify the influence of correlations between the adjusted parameters. The validation data are used to finally validate the accuracy of the adjustments. The figures contain the dose difference distributions for the plateau (upper right) and the proximal shoulder (lower right) region. While the distributions show a high symmetry at the plateau region the ones, which correspond to the proximal shoulder are asymmetric and cannot be approximated accurately by a Gaussian.

The simulated and measured distal fall-off regions are compared by analyzing deviations of the range offsets ΔR_{90} , ΔR_{80} , ΔR_{20} (sim - exp). The distribution of those offsets for all requested ranges is presented in Figure 4.6 for the reference data set and in Figure 4.7 for the validation data. While ΔR_{80} is approximately zero in all options, ΔR_{90} and ΔR_{20} changes for every requested range, whereby the absolute ΔR_{20} show the largest differences from zero, especially at the Options 3,4,5,6 and for certain points in Option 7,8. All results of the comparison of adjusted simulated depth-dose distributions to the measurements are listed in Table D (reference) and Table E (validation). Figure A and Figure B present examples of adjusted simulated and measured depth-dose distributions (reference and validation).

Figure 4.8 illustrates the procedure of comparing simulated and measured lateral profiles. For the simulation of the lateral profiles the aperture shape of the apertures is adjusted to the one, which is used in the measurements (10 cm \times 10 cm).

The profiles are compared at the lateral plateau region and at the profile flanks, separately. The plateau regions are compared by fitting the dose difference distribution by a Gaussian, whereby the standard deviation σ_D represents the error between the relative and measured plateau doses. The profile flanks are compared by deriving the lateral penumbras of the left P_{left} and the right profile flank P_{right} . The field sizes are calculated to compare the extension of the profiles. The deviations in the field sizes (sim-exp) are visualized in Figure 4.9 for the lateral x -projections and in Figure 4.10 for the y -projections. There is a systematic difference in the field size for both projections. For the x -projection the offset is approximately $\Delta \bar{W}_{50,x} \approx -0.9$ mm. For the y -projection it is $\Delta \bar{W}_{50,y} \approx -0.5$ mm. All results of the comparison of adjusted simulated lateral profiles and the measurements are summarized in Table F and Table G. Figure C and Figure D present examples of simulated and measured lateral profiles.

4.2 Output Factor Simulations for Absolute Dosimetry

In a first step the simulated and measured output factors, which belong to the reference fields (patient quality assurance), are presented. The data set has to be considered first, because it contains the reference field ($R_{\text{req}} = 16$ cm, $M_{\text{req}} = 10$ cm, $z_{\text{calib}} = 11.72$ cm), which is used to normalize all simulated output factors. In a second step, the results of the output factor prediction, which belong to measurements for research purposes, are illustrated. The distribution of relative errors $\Delta\psi_{\text{rel}}$ of the simulated output factors is described and the dependencies of the errors on the field range and modulation are characterized. The output factors of the reference fields and the research data are merged in one curve by introducing the parameter $r = (R - M)/M$. The dependency of $\Delta\psi_{\text{rel}}$ on the nozzle option is characterized and option dependent calibration factors are applied. Finally, the results of the output factor simulation for two treatment fields, which belong to the proton plan of Patient 1, are presented and the field output factors are derived.

All output factors are normalized to the reference field ($R_{\text{req}} = 16$ cm, $M_{\text{req}} = 10$ cm, $z_{\text{calib}} = 11.72$ cm). Therefore, the simulated output factors are equalized to the measured ones and the corresponding α ratios are derived for each volume, separately (Equation (3.15)). α describes the ratio between the simulated ($D_{\text{sim}}/D_{\text{sim,IC23}}$) and the measured output factor ($D_{\text{exp}}/\text{MU}_{\text{exp,IC23}}$). The results are presented in Table 4.2. The output factors ψ and the corresponding relative errors $\Delta\psi_{\text{rel}}$ of all reference

Table 4.2: Calculated alpha ratios, which are derived by comparing the simulated output factors for the reference field ($R_{\text{req}} = 16$ cm, $M_{\text{req}} = 10$ cm, $z_{\text{calib}} = 11.72$ cm) to the measured one for each TOPAS scoring volume.

Volume	V_{IC23_1}	V_{IC23_2}	V_{IC23_3}	V_{IC23_4}
α	19.742	20.336	1.123	0.541

fields, which are used in the patient quality assurance, are illustrated in Figure 4.11. The mean values μ and variances ν of $\Delta\psi_{\text{rel}}$ are presented in Table K for all volumes. The output factors, which are simulated by using V_{IC23_3} , show the highest accuracy to the measured ones. For all volumes the relative difference of the simulated output factors $\Delta\psi_{\text{rel}}$ decrease linearly in Option 1,2,3,4, whereby in Option 5,6,7,8 the error increases with increasing option number.

Table K summarizes mean values $\mu(\Delta\psi_{\text{rel}})$ and variances $\nu(\Delta\psi_{\text{rel}})$ of the research data \mathcal{M}_{Res} . The output factors, which are simulated by using V_{IC23_3} show the highest accuracy to the measurements. The ψ and $\Delta\psi_{\text{rel}}$ values of the first part of \mathcal{M}_{Res} (constant modulation) are visualized in Figure 4.12. The option mean values μ_{opt} and variances ν_{opt} of the relative output factor error varies for every option. Within each option μ_{opt} and ν_{opt} depend on the representative volume. The dependency of $\Delta\psi_{\text{rel}}$ on the range R_{req} changes for different options. In Option 3,4,5,6 $\Delta\psi_{\text{rel}}$ decreases linearly with a negative slope m_{opt} for increasing R_{req} . In Options 1,2,7 m_{opt} is approximately zero. The option mean values, variances and slopes of $\Delta\psi_{\text{rel}}$, which belong to (\mathcal{M}_{Res} , Part 1) are listed in Table L. The ψ and $\Delta\psi_{\text{rel}}$ values of the second part of \mathcal{M}_{Res} (constant ranges) are visualized in Figure 4.13, H, I, J, K. Each figure shows the output factors and errors for SOBP fields, with a certain constant range and varying modulations. The dependency of $\Delta\psi_{\text{rel}}$ on the modulation \mathcal{M}_{Res} changes for every field range. For one fixed range $\Delta\psi_{\text{rel}}$ decreases linearly with increasing \mathcal{M}_{Res} in first

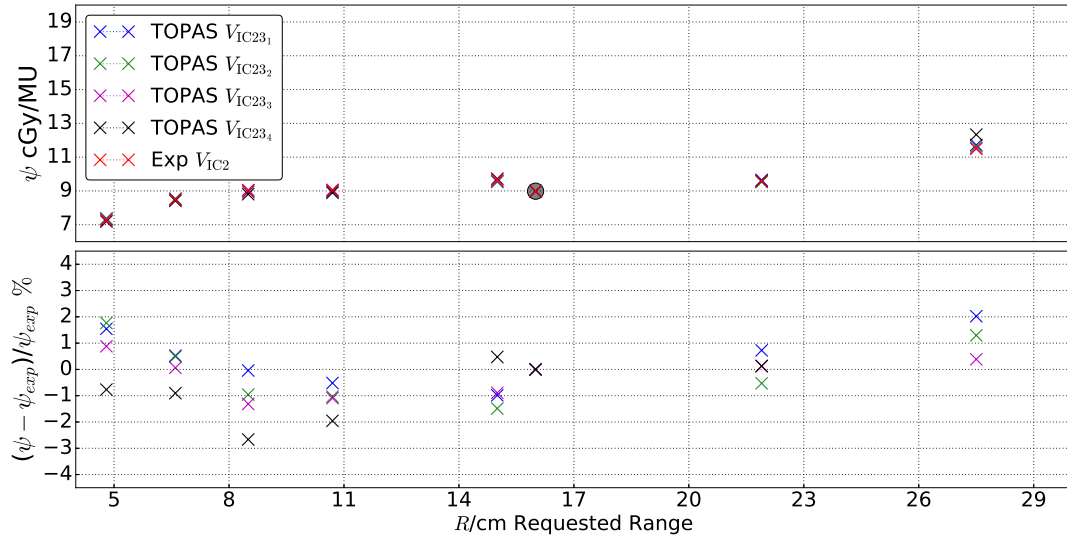


Figure 4.11: Measured and simulated output factors ψ (upper sub-plot), which belong to the reference fields, which are used in the patient quality assurance measurements at UPTD. The lower sub-plot visualizes the relative differences $\Delta\psi_{\text{rel}}$ between the simulations and the measurements. The simulated ψ are normalized to the standard field with $R_{\text{req}} = 16$ cm and $M_{\text{req}} = 11$ cm.

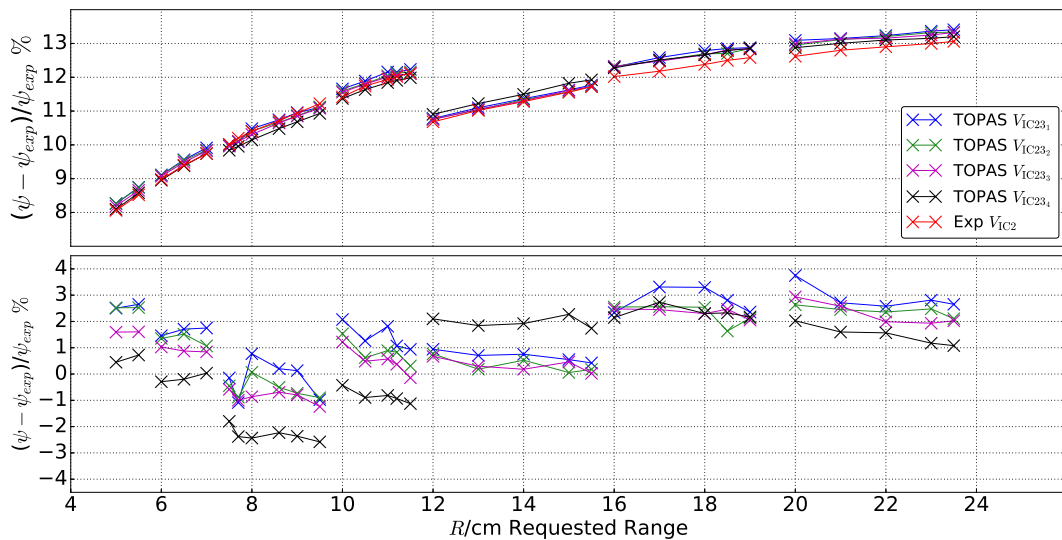


Figure 4.12: $\psi_{\text{rel}}(R_{\text{req}})$ and $\Delta\psi_{\text{rel}}(R_{\text{req}})$ distributions, which are derived by comparing TOPAS simulations to the first part of measured data set \mathcal{M}_{Res} , with constant modulation $M_{\text{req}} = 4$ cm. Four different volumes are used to compare the accuracy of the mapping of the MU charge collection. All output factors are normalized to the reference field ($R_{\text{req}} = 16$ cm and $M_{\text{req}} = 11$ cm).

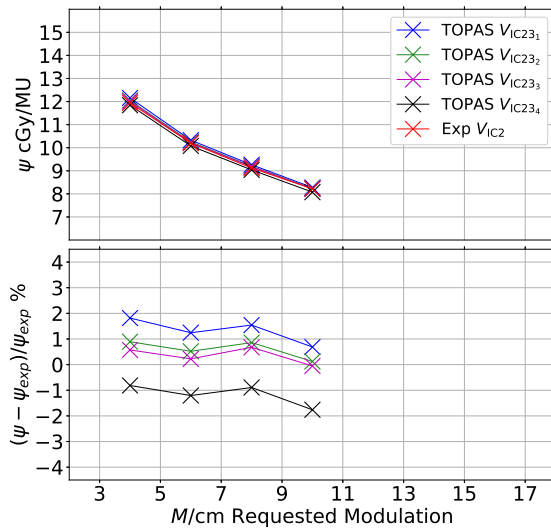


Figure 4.13: $\psi_{\text{rel}}(M_{\text{req}})$ and $\Delta\psi_{\text{rel}}(M_{\text{req}})$ distributions, which are derived by comparing TOPAS simulations to the second part of \mathcal{M}_{Res} , with constant range $R_{\text{req}} = 11$ cm. Four different volumes are used to compare the accuracy of the mapping of the MU charge collection. All output factors are normalized to the reference field ($R_{\text{req}} = 16$ cm and $M_{\text{req}} = 11$ cm).

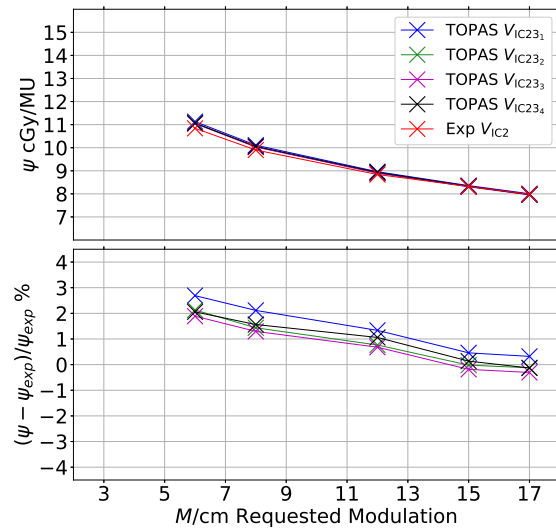


Figure 4.14: $\psi_{\text{rel}}(M_{\text{req}})$ and $\Delta\psi_{\text{rel}}(M_{\text{req}})$ distributions, which are derived by comparing TOPAS simulations to the second part of \mathcal{M}_{Res} , with constant range $R_{\text{req}} = 18$ cm. Four different volumes are used to compare the accuracy of the mapping of the MU charge collection. All output factors are normalized to the reference field ($R_{\text{req}} = 16$ cm and $M_{\text{req}} = 11$ cm).

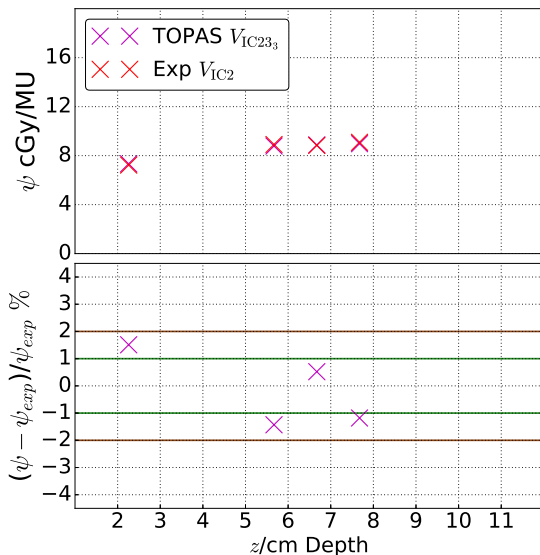


Figure 4.15: $\psi_{\text{rel}}(z)$ and $\Delta\psi_{\text{rel}}(z)$ distributions, which are derived by comparing TOPAS simulations to the ($\mathcal{M}_{\text{Patient}}$, Field 1) measurement. V_{IC23_3} is used to map the MU charge collection in TOPAS. All output factors are normalized to the reference field ($R_{\text{req}} = 16$ cm and $M_{\text{req}} = 11$ cm).

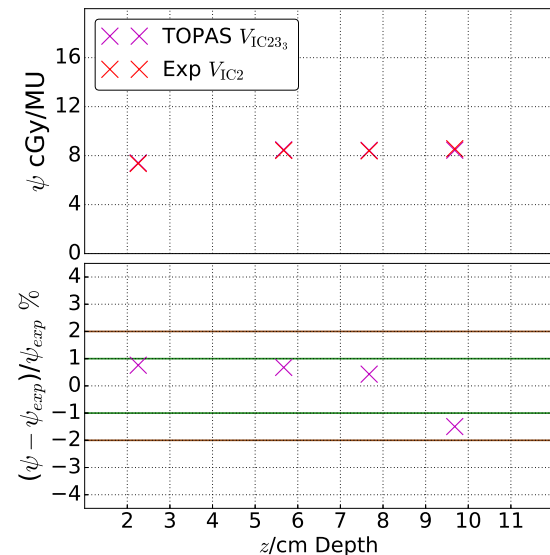


Figure 4.16: $\psi_{\text{rel}}(z)$ and $\Delta\psi_{\text{rel}}(z)$ distributions, which are derived by comparing TOPAS simulations to the ($\mathcal{M}_{\text{Patient}}$, Field 2) measurement. V_{IC23_3} is used to map the MU charge collection in TOPAS. All output factors are normalized to the reference field ($R_{\text{req}} = 16$ cm and $M_{\text{req}} = 11$ cm).

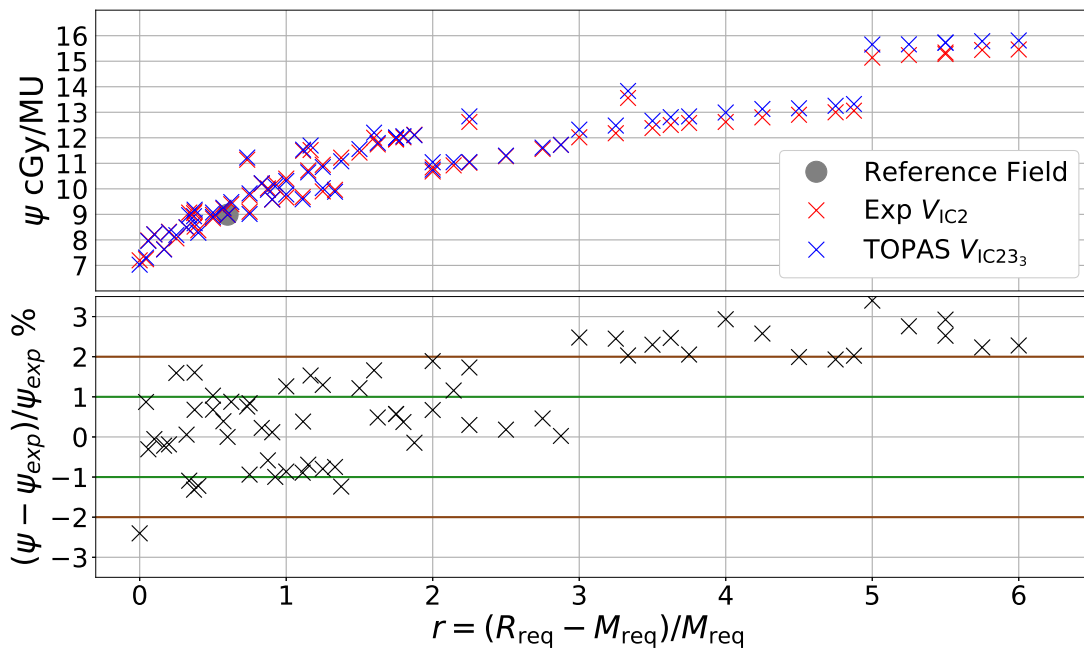


Figure 4.17: $\psi_{\text{rel}}(r)$ and $\Delta\psi_{\text{rel}}(r)$ distributions, which are derived by comparing TOPAS simulations to the measured data sets \mathcal{M}_{Ref} and \mathcal{M}_{Res} . V_{IC233} is used to map the MU charge collection in TOPAS. All output factors are normalized to the reference field ($R_{\text{req}} = 16$ cm and $M_{\text{req}} = 11$ cm).

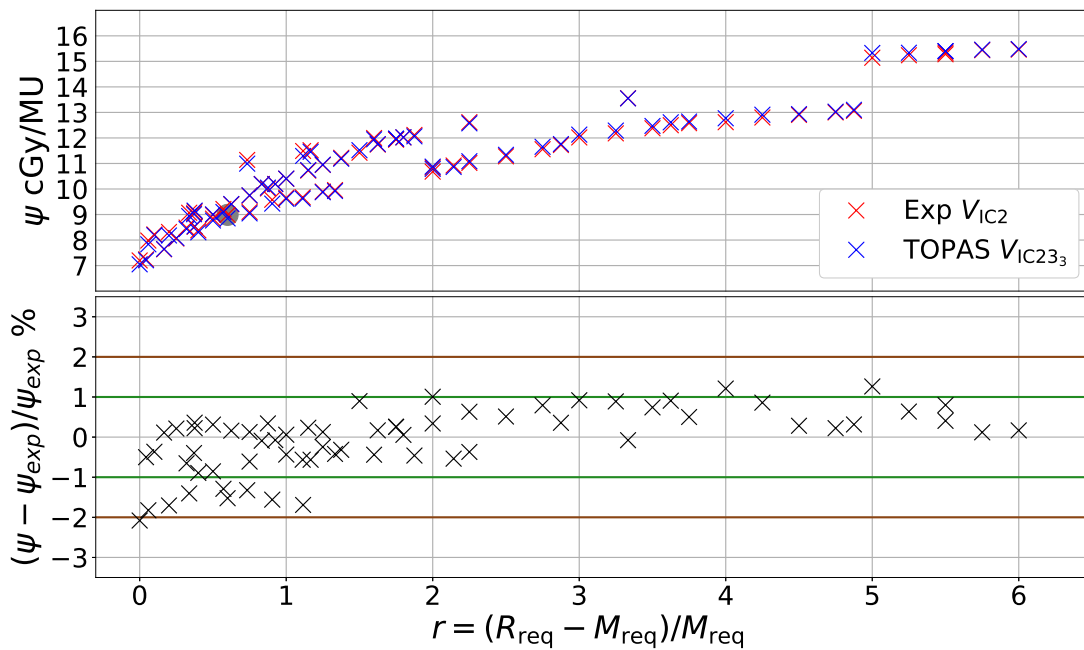


Figure 4.18: $\psi_{\text{rel}}(r)$ and $\Delta\psi_{\text{rel}}(r)$ distributions, which are derived by comparing TOPAS simulations to the measured data sets \mathcal{M}_{Ref} and \mathcal{M}_{Res} . The simulated output factors are adjusted with an option dependent calibration factor. V_{IC233} is used to map the MU charge collection in TOPAS.

approximation with the negative slope m_M . The slope is similar for all volumes. The mean values and variances and the slopes m_M , which belong to the five requested ranges $\mathcal{R}_{\text{Res}} = 11, 14, 18, 22, 26$ cm, are listed in Table M.

To merge the derived $\Delta\psi_{\text{rel}}$ values, which corresponds to SOBPs fields with varying ranges and modulations in one curve (one dimensional), they are visualized of the parameter $r = (R_{\text{req}} - M_{\text{req}})/M_{\text{req}}$, which is motivated in Sub-section 2.3.2. The $\psi_{\text{rel}}(r)$ and the $\Delta\psi_{\text{rel}}(r)$ distribution, which belongs to V_{IC23_3} is visualized in Figure 4.17. A jump of the relative errors at $r = 3$ is observed. When applying option dependent calibration factors, the accuracy of the $\Delta\psi_{\text{rel}}$ is increased by 1%. The $\psi_{\text{rel}}(r)$ and $\Delta\psi_{\text{rel}}(r)$ distributions with option calibrations are illustrated in Figure 4.18.

According to the previous results, the volume V_{IC23_3} is selected as the one, which represents the area of the measured MU charge collection in the TOPAS simulation with the highest precision. Therefore, V_{IC23_3} is used in the output factor simulations, which belong to the patient QA measurements of Patient 1. The output factors and relative errors for both treatment fields are visualized in Figure 4.15 and Figure 4.16. At each treatment field the output factors are measured and simulated at four representative calibration points in the SOBPs field. In first approximation a linear decrease of $\Delta\psi_{\text{rel}}$ with increasing depth z_{calib} of the calibration points is observed. The field output factors ψ_W are predicted within 1% accuracy.

4.3 TOPAS Simulation of a Proton Treatment Plan

The planned and the simulated dose distributions for the proton plan of Patient 1 are compared by studying the dose differences for different computed tomography (CT) image slices. The accuracy of the positioning of the simulated dose grid is analyzed by studying the influence of a spatial TOPAS dose grid shift (relative to the planned dose grid) on the differences between the simulated and planned dose distributions. To ensure that, the statistical uncertainty of the Monte-Carlo dose simulation is negligible a convergence analyze is performed for one treatment field. Deviations between planned and simulated dose distributions are characterized by performing gamma analyzes with varying gamma criteria. The simulated linear energy transfer distribution is visualized and described. The distribution of the corresponding variable relative biological effectiveness (RBE) is illustrated and differences between the doses, which are weighted by a variable and a constant RBE are characterized.

Figure 4.19 shows the planned and the simulated dose distributions including the corresponding differences for three inline Y positions (three computed tomography slices). Only dose values above the threshold d_{th} are visualized. d_{th} corresponds to 3% of the mean value D_{XiO}^W of the high dose region W of the planned dose distribution.

$$d_{\text{th}} = 0.03 \cdot D_{\text{XiO}}^W \quad (4.1)$$

At inline position $Y = 1.4$ cm, the deviations between the simulated and planned doses at the high dose region are below 3% (D_{XiO}^W corresponds to 100%). At the field edges they increase up to 8%. The simulated dose at the proximal shoulder region of the first treatment field (snout angle 295°) is about 1% larger compared to the planned one. For the second treatment field the simulated proximal doses are smaller by about 1%, compared to the planned distribution.

At the inline position $Y = 3.4$ cm, the deviations between the simulated and planned doses at the high dose region remains within the 3% tolerance. The deviations at the field edges become larger compared to inline position $Y = 1.4$ cm. At the lower right corner of the image, there is a planned overshoot, which is reproduced in TOPAS. Dose deviations up to eight gray are obtained in the overshoot region. At inline position $Y = 5.6$ cm, the dose deviations further increase, especially at regions with high material density gradients like between bone, tissue, pillow or air material.

The accuracy of the positioning of the patient dose scorer in TOPAS is validated by varying the TOPAS grid by one voxel in any spatial dimension relative to the planned grid. Each shift leads to an increase in the dose difference, which can be observed in Figure 4.20. As the selected image slice is within the homogeneous high field dose region (inline position $Y = 1.4$ cm) the voxel variation mainly effect the dose differences at the plateau edges, whereby the plateau dose remains approximately constant.

Especially at the high field dose regions, dose fluctuations up to 2% are observed. To validate, that these dose stripes are not purely statistical (Monte-Carlo) a convergence analyze is performed for one treatment field (Figure 4.21). One dimensional profiles slices are compared for simulated fields, with 10^6 , 10^7 and 10^8 protons reaching the patient. While an increase of the proton number from 10^6 to 10^7 reduce the dose fluctuations from about 8% to 2%, a further increasing of the proton number to 10^8 do not reduce the fluctuations.

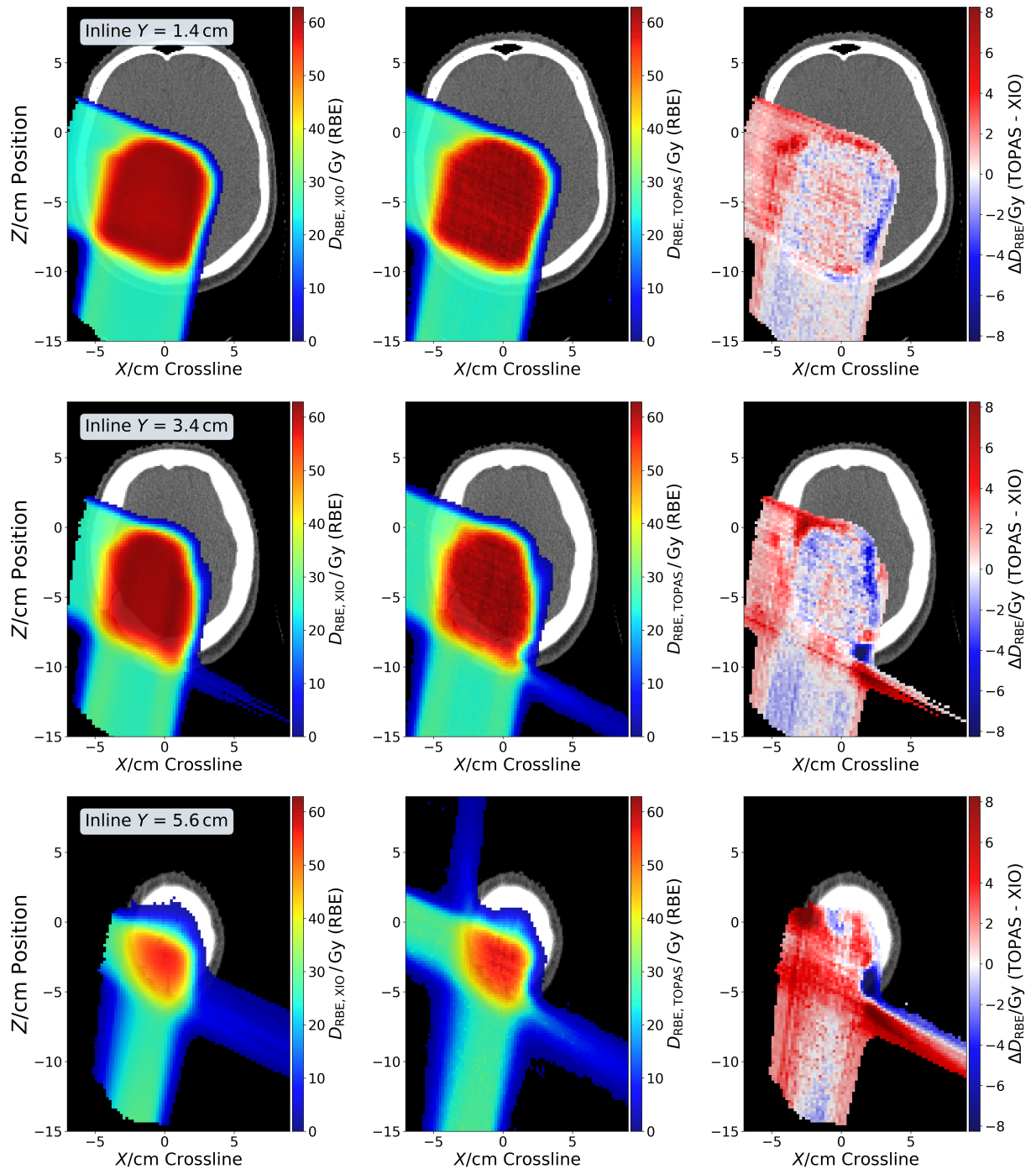


Figure 4.19: Planned (XiO , left) and simulated ($TOPAS$, center) dose distributions, which correspond to the proton plan of Patient 1. The dose differences ($TOPAS - XiO$) are visualized on the right. Only doses above 3% of the mean dose value at the central high dose region of the planned distribution, are visualized. The dose distributions are shown for three different computed tomography slices, with the inline positions $Y = 1.4$ cm (upper subplots), $Y = 3.4$ cm (center subplots) and $Y = 5.6$ cm (lower subplots). All doses are given in the units of RBE, whereby a constant RBE of 1.1 is applied.

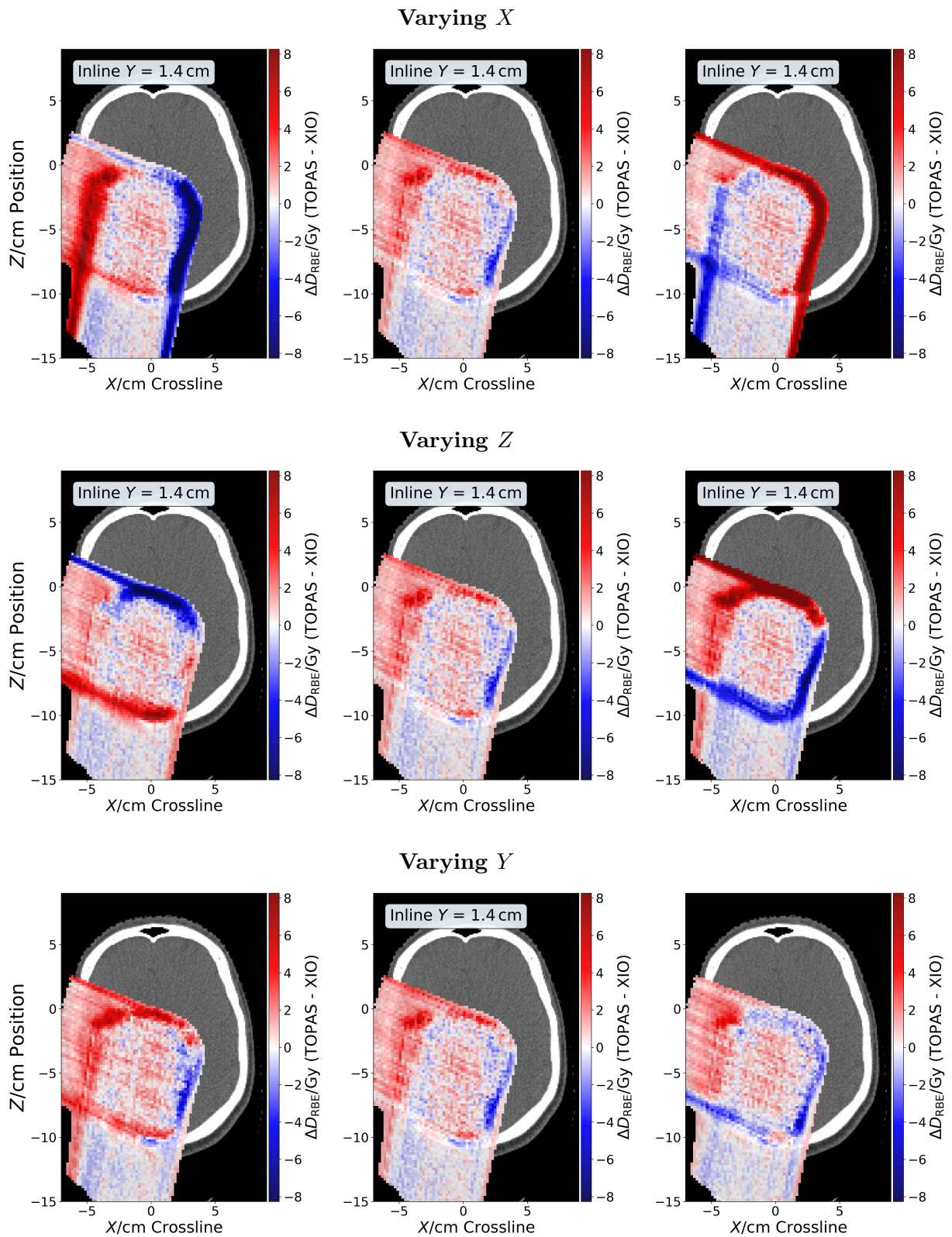


Figure 4.20: Dose differences between the planned (XiO) and the simulated (TOPAS) dose distributions. The simulated dose grid is shifted by one voxel in negative (left) and positive (right) crossline (varying X, upper subplots), depth (varying Z, center subplots) and inline (varying Y, lower subplots) direction. This allows to study the accuracy of the grid positioning in TOPAS.

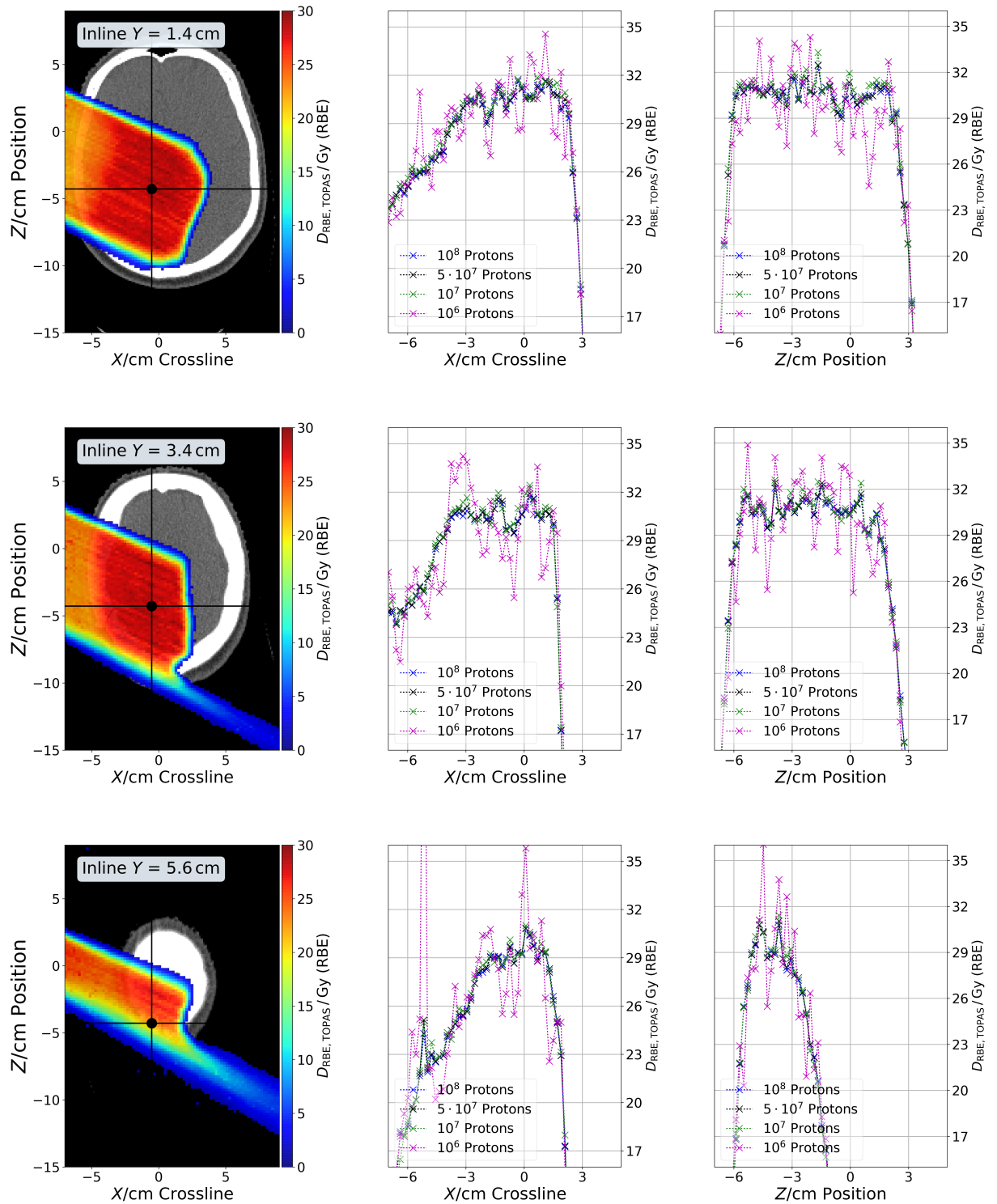


Figure 4.21: Convergence analyze, for the first simulated treatment field, which belong to the proton plan of Patient 1. The distal (center, $D(x)$) and the lateral (right, $D(z)$) dose distributions are illustrated for three inline positions. Approximately 10^7 , 10^8 and 10^9 protons reaching the patient. The dose distribution, which belong to the highest simulation statistics is illustrated on the left..

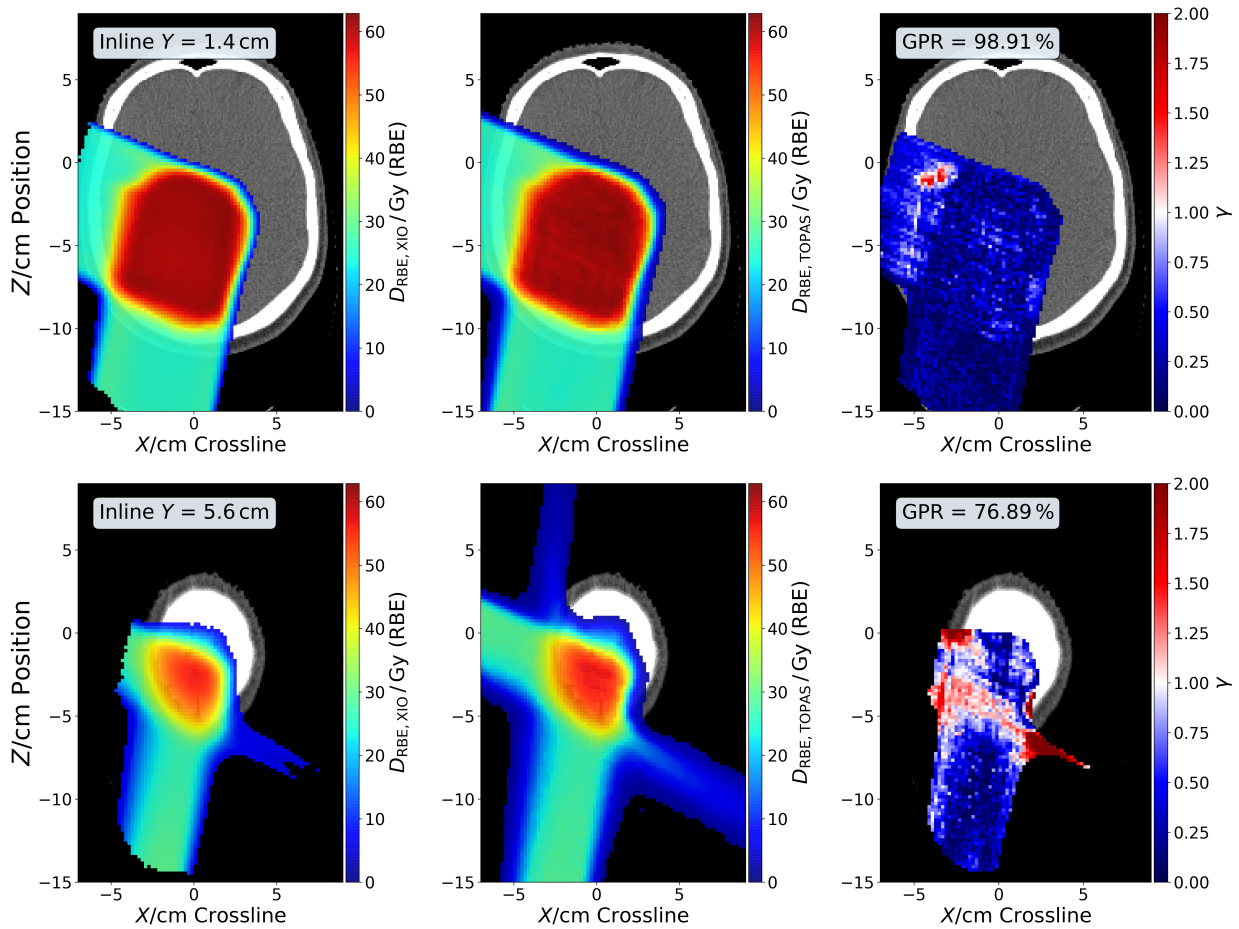


Figure 4.22: Planned (XiO, left) and simulated (TOPAS, center) dose distributions, which correspond to the proton plan of Patient 1. On the right the corresponding voxel gamma values are visualized and the GPR is shown. The applied gamma criteria are: $\lambda_{x,y,z} = 1/\text{mm}$, $\lambda_D = 3\%$ and $\lambda_{th} = 50\%$. The distributions are shown for three different computed tomography slices, with the inline positions $Y = 1.4\text{ cm}$ (upper subplots), $Y = 3.4\text{ cm}$ (center subplots). A median filter is applied (two dimensional, only next voxels) to the dose images to show the effect of applying image smoothing techniques.

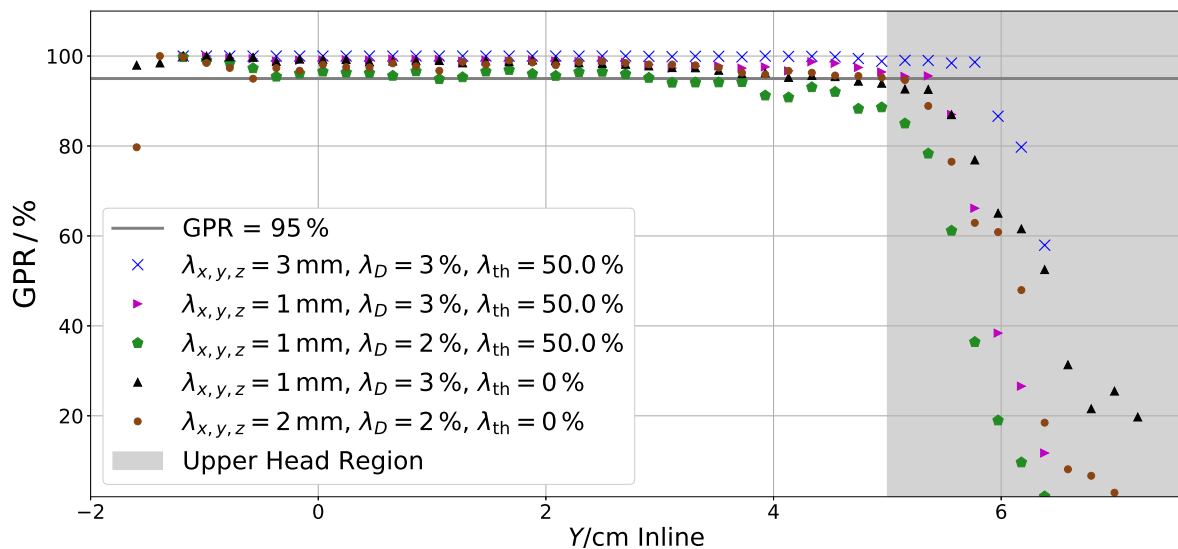


Figure 4.23: Gamma pass rate (GPR) for all slices, which correspond to the inline positions of the planned dose grid. In addition Region 2 is visualized, which is defined as the upper head region.

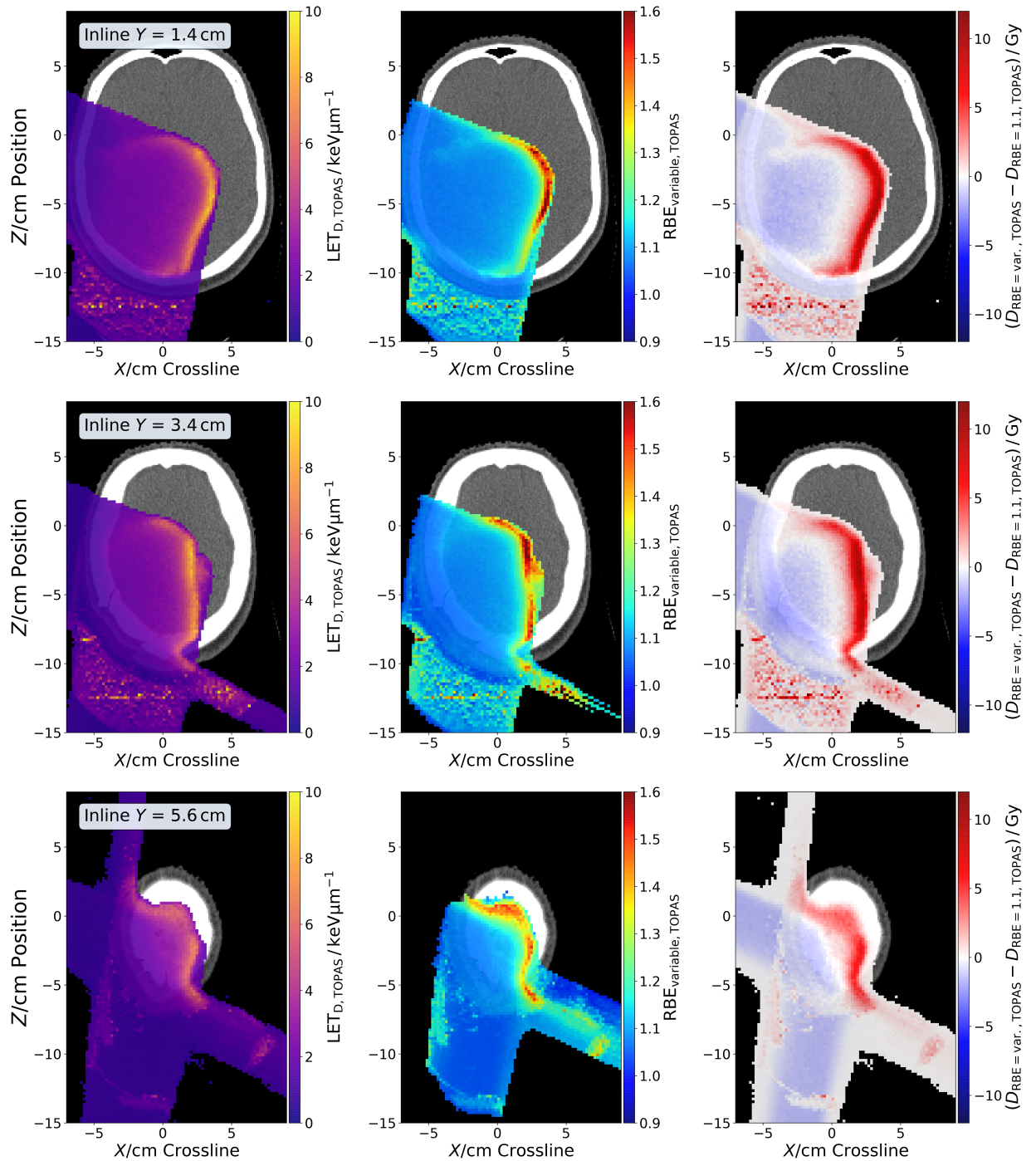


Figure 4.24: Simulated linear energy transfer (left), RBE (center) and RBE weighted dose distribution (right). The linear energy transfer is dose averaged. The RBE is calculated based on the model, which is presented in Ref. [22]. The variable RBE is applied to weight the simulated dose distribution. The distributions are shown for three different computed tomography slices, with the inline positions $Y = 1.4$ cm (upper subplots), $Y = 3.4$ cm (center subplots) and $Y = 5.6$ cm (lower subplots).

Table 4.3: Results of the gamma analyze for the proton plan of Patient 1, whereby the gamma pass rates are listed for different conditions. They are derived for two different inline field regions separately.

	criteria	$\lambda_{x,y,z}/\text{mm}$	$\lambda_D/\%$	$\lambda_{\text{th}}/\%$	$\lambda_{\text{th}}/\text{Gy}$	GPR/%
Region 1	GC ₁	3	3	50	30	≥ 99
Center Brain	GC ₂	1	3	50	30	≥ 96
$Y \in [-2 5] \text{ cm}$	GC ₃	1	2	50	30	≥ 85
	GC ₄	3	3	0	0	≥ 94
	GC ₅	2	2	0	0	≥ 95
Region 2	GC ₁	3	3	50	30	≥ 50
Upper Head	GC ₂	1	3	50	30	≥ 10
$Y \in [5.2 7.7] \text{ cm}$	GC ₃	1	2	50	30	≥ 0
	GC ₄	3	3	0	0	≥ 15
	GC ₅	2	2	0	0	≥ 0

The stripes disappear when applying a median filter which only counts the next neighbors. This effect is illustrated in the left sub-plots of Figure 4.22. Figure 4.23 illustrates the distribution of the gamma pass rates (GPR) over all CT slices, which contain planned dose values. Different gamma criteria are applied. The criteria and the corresponding GPR are listed in Table 4.3. For all criteria the GPR stays approximately constant at inline positions Y between -2 cm and 5 cm (Region 1) and drops down for inline positions above 5 cm (Region 2). The highest GPR are achieved, when applying the criteria GC₁. A stronger local condition (GC₂) do not lead to GPR values below 95 % in Region 1. A reduction of the dose threshold to zero, do not change the results dramatically. Figure 4.22 illustrates the γ distribution for criteria GC₄, whereby one slice corresponds to Region 1 and the other one to Region 2.

In the left sub-plots of Figure 4.24 simulated linear energy transfer distributions are visualized. The highest LET values are observed at the distal field edges. In addition LET hot spots are obtained in the pillow and at the distal end of the simulated overshoots.

The distribution of the variable relative biological effectiveness is visualized in the center sub-plots of Figure 4.24. RBE hot spots are observed at high LET regions. At the center region of the treatment field the variable RBE stays approximately constant (1.1). It increases to values up to 1.6 at the distal field edges. The dose (RBE), which is predicted by using the variable RBE model is up to 15 % larger compared to the predicted dose (RBE) of the constant RBE model (Figure 4.24, right sub-plots).

-

5 Discussion

In a first step, the results of the adjustment and validation of TOPAS in predicting therapeutic dose distributions in water phantom are summarized. Deviations between simulated and measured depth-dose distributions are compared at the distal fall-off, plateau and proximal shoulder region. For the simulated lateral profiles the deviations in the plateau region and at the profile flanks are characterized. The deviations are compared to the measurement uncertainties and the clinical tolerances, which are listed in Table 3.2.

In a second step, the achieved accuracies of the prediction of measured output factors ψ_{exp} in TOPAS are summarized. Therefore, the absolute relative difference $|\Delta\psi_{\text{rel}}|$ of the simulated output factors ψ_{sim} to the measured ones is compared to the measurement uncertainty of the absolute dose at UPTD, which is 1%. For different data sets the dependency of $|\Delta\psi_{\text{rel}}|$ on the field range, modulation and the TOPAS scoring volume, which is used to map the charge collection in the IC2, is analyzed.

Finally, the deviations between the simulated and the planned absolute dose distribution, which belong to the proton plan of Patient 1, are characterized. The results of the gamma analyze of the simulated and planned dose images are summarized and the dependency of the gamma pass rates (GPR) on the inline image position (compute tomography slice) and the applied gamma criteria is discussed. The simulated distribution of the linear energy transfer and the calculated variable RBE (relative biological effectiveness) in the patient are discussed and compared to the literature.

5.1 Adjustment and Validation of TOPAS Dose Distributions

The validation data depth-dose curves are predicted within the measurement uncertainty at the plateau and distal fall-off region. The lateral widths and penumbras are predicted within the clinical tolerances. The results of the comparison of the adjusted simulations and the measurements in a water phantom are presented in Table 5.1.

Plateau and Proximal Region The plateau regions are predicted within the measurement uncertainty of 1%. Systematic dose deviations at the proximal shoulder region are an indicative, that the square apertures, which are used in the measurements, have a non-negligible impact on the shape of the depth-dose curves, even if they are scored in volumes along the beam axis with small lateral extensions. In the simulation of the depth-dose curves two ring apertures are used, with an inner radius of $R_{\text{inner}} = 8.46$ cm. They generate beams with parabolic lateral shapes that differ from the rectangle shaped profiles that are generated by the 10 cm \times 10 cm square apertures that are used in the measurements. For lateral positions close to the beam axis the dose profiles are similar. Nevertheless, there is a small uncertainty, which is in particular relevant at low depths in the water phantom.

Table 5.1: Results of the comparison between simulated (adjusted) and measured (validation and reference) dose distributions.

Depth-Dose	$ \mu_D \%$	$\sigma_D \%$	$ \Delta R_{90} \text{ mm}$	$ \Delta R_{80} \text{ mm}$	$ \Delta R_{20} \text{ mm}$
Reference	≤ 0.17	≤ 0.34	≤ 0.19	≤ 0.01	≤ 0.48
Validation	≤ 0.26	≤ 0.98	≤ 0.15	≤ 0.12	≤ 0.54
Lateral	$ \mu_D \%$	$\sigma_D \%$	$ \Delta W_{50} \text{ mm}$	$ \Delta P_{\text{left}} \text{ mm}$	$ \Delta P_{\text{right}} \text{ mm}$
Validation	≤ 0.38	≤ 1.92	≤ 0.95	≤ 0.56	≤ 0.55

At higher depths in the water phantom, the lateral parabolic profile flattens and becomes more comparable to the rectangle one at regions close to the beam axis. Therefore, the impact of using different apertures is in particular high at regions close to the apertures, where scattering effects at the aperture edges have the largest influence on the dose profile in the water phantom. This is the reason, why the χ^2 -fit has difficulties to determine the optimal beam current weights especially at the proximal shoulder regions and fit instabilities are observed, when including the proximal shoulder in the domain (Figure G). This can be avoided by restricting the domain to the plateau region, but weight uncertainties still remain.

The derived current weights do not fully represent the experimental situation and systematic dose deviations are induced by those weight uncertainties in the plateau regions, too, especially for depth-dose distributions with low ranges and a the plateau regions close to the proximal shoulder. Therefore, the μ_D values of the Gaussian fits of the dose difference distributions in the plateau region can increase to absolute values up to 0.26 % as shown in Table 5.1. For certain low range depth-dose distributions small dose ripples are observed, which do not occur in the measurements. They correspond to the number of underlying base functions and illustrates the weight uncertainties. In order to increase the accuracy of the plateau region of the depth-dose curves the beam current modulation weights should be recalculated by using the same apertures in the simulation as used in the measurements.

Distal Fall-Off Region The ranges R_{90} and R_{80} at the distal fall-off regions of the measured depth-dose curves are reproduced within the measurement uncertainty for all validation data depth-dose curves. The R_{20} is not predicted within the measurement uncertainty, which is an indication that the beam energy spread (BES) should be further optimized. The dependency on the uncertainty of the BES on the requested range can be clearly observed in Figure 4.6 and in Figure 4.7. Especially for the nozzle Options 3,4,5,6 and for certain points in Option 7,8 the initial beam energy distribution should be further fine-tuned. One fact, which contributes to the BES uncertainty is the order of the applied adjustments. The option dependent energy shift is applied after the adjustment of the beam energy spread (BES). As the BES is defined relative to the mean beam energy, there is a small change of the BES values after the option dependent range adjustment. The energy shifts are in the order of 1 MeV. When assuming the absolute standard deviation to stay constant within an option one can derive the change in BES.

$$\text{BES} = \frac{\sigma_{E,\text{abs}}}{\bar{E}} \quad \Delta\text{BES} = \sigma_{E,\text{abs}} \left(\frac{1}{\bar{E}} - \frac{1}{\bar{E} - \Delta\bar{E}} \right) \quad (5.1)$$

The BES shifts are in the order of 0.01 % as illustrated in Figure F. Those shifts are small, but add an uncertainty to the range straggling of every pristine Bargg peak (PP). Nevertheless, the

influence on the BES shift on the accuracy of the beam current modulation is small. Otherwise the standard deviations of the dose difference distributions σ_D , which correspond to the plateau regions of the reference data depth-dose distributions would not be similar to the ones of the χ^2 -fits (Table 5.1).

Lateral Profiles The widths and the penumbras of the lateral profiles are predicted within the clinical tolerances. In the x -projection a systematic underestimation of lateral width of about 0.9 mm is observed (Figure 4.9). In the y -projection it is about 0.6 mm (Figure 4.10). The binning size, which is used in the Monte-Carlo simulation should be further increased to exclude that these deviations are dominated by binning effects. An uncertainty of the lateral field prediction can be related to an uncertainty of the mapping of the overall nozzle scattering angle. Nevertheless, an adjustment of this angle is difficult as it depends on a large amount of scattering geometries and their relative positions. The relative dose in the lateral plateau region is predicted with a standard deviation of $\sigma_D \leq 1.92\%$. Dose fluctuations up to 2% are observed in the simulations and in the measurements. To reduce the simulated dose fluctuations the Monte-Carlo statistics has to be further increased and a convergence analyze should be performed. The measured fluctuations might occur, because the lateral profiles are measured with a small active detector volume, which is sensitive to dose fluctuations. A small detector is chosen to accurately determine the profile flanks. For practical concerns, the statistical dose fluctuations at the plateau region are usually not considered as problematical and are smoothed by the treatment planning system in order to generate the proton beam model. Nevertheless, the comparison of simulated and measured lateral profiles would benefit from a precise experimental characterization of the dose fluctuations at the lateral plateau region.

The 1D lateral profiles are compared by normalizing both curves to the central lateral plateau region. If the profiles differ in height, they get stretched differently which induces an error particularly for the lateral penumbras. The accordance in height depends on the accuracy of the beam current modulation. Therefore, the accuracy of the prediction of lateral profiles in TOPAS will benefit from any further improvements of the beam current modulation weights.

5.2 Output Factor Simulations for Absolute Dosimetry

All measured output factors are predicted with an accuracy of 3%, when normalized to the reference field ($R_{\text{req}} = 16$ cm, $M_{\text{req}} = 10$ cm). This accuracy is achieved, when simulating the MU signal in TOPAS in the representative volume $V_{\text{IC}23_3}$. When applying nozzle option calibration factors the uncertainty can be improved to 2%. A dependency of the relative error ψ_{rel} of the simulated output factors on the representative scoring volume $V_{\text{IC}23}$, on the field range and modulation, and on the depth of the calibration point z_{calib} in the water phantom is observed. The results of the output factor prediction in TOPAS are listed in Table 5.2 for all data sets and $V_{\text{IC}23_3}$.

The current model of the IBA nozzle in TOPAS, including beam source adjustments, is not able to predict the output factors within the measurement uncertainty of 1%. Improvements of the beam current modulation and the mapping of the MU charge collection in TOPAS have the potential to further reduce the current uncertainty of 3%. The uncertainties and the potential improvements of the beam current modulation is discussed in the previous section. The output factor represents approximately the ratio of the SOBP plateau dose to the entrance dose. Therefore, it is sensitive to

Table 5.2: Results of the absolute relative error of simulated output factors for different measurement data sets.

Data	Label	Volume	$ \Delta\psi $
Reference Fields, Patient QA	\mathcal{M}_{QA}	V_{IC233}	$\leq 1.5\%$
Research Data, Varying R_{req}	\mathcal{M}_{Res} , Part 1	V_{IC233}	$\leq 3\%$
Research Data, Varying M_{req}	\mathcal{M}_{Res} , Part 2	V_{IC233}	$\leq 3\%$
\mathcal{M}_{QA} , \mathcal{M}_{Res} + option calibrations	$\mathcal{M}_{\text{Calib}}$	V_{IC233}	$\leq 2\%$
Patient QA, Patient 1, Field 1	$\mathcal{M}_{\text{Patient}}$, Field 1	V_{IC233}	$\leq 2\%$
Patient QA, Patient 1, Field 2	$\mathcal{M}_{\text{Patient}}$, Field 2	V_{IC233}	$\leq 2\%$

uncertainties of the dose prediction and the accuracy of the output factor prediction in TOPAS will benefit from improvements of the beam current modulation.

The current mapping of the MU charge collection in TOPAS should be considered as a first iteration step. The real measuring volume for the MU charge collection in the IC2 is very small. A dose scorer with similar extensions would require a high Monte-Carlo statistics. In order to limit the simulation effort, larger scoring volumes are implemented in TOPAS. They are placed in the surrounding area of the measurement volume, including the ion chamber IC3. The precision of a selected volume is assessed based on the accuracy of the corresponding output factor prediction. The achievable accuracy of the simulation of the output factors by following this pragmatic approach is limited. Nevertheless, has its benefit in illustrating the potential of TOPAS in predicting absolute doses within the measurement uncertainty.

A volume uncertainty contributes to an uncertainty of the MU signal prediction mainly for two reasons. First, the particle fluence in the area of charge collection is not mapped accurately. This includes primary particles and secondary particles. Second, the energy and therefore the stopping power of the protons, which are traversing the volume differ if placed at different position along the beam axis. Next to the volume shape itself the output factor, depends on the measured calibration point in the water phantom. It is a value, which summarizes the efficiency of a specific setup of the full double-scattering system and depends on the field size (range and modulation), the apertures and the snout position.

Different measurements are used to study the accuracy of the output factor prediction in TOPAS. The data set contains different variations of field sizes, apertures and calibration points in the water phantom. They allow to draw different conclusions about the output factor dependencies. Therefore, they are discussed separately.

Research Reference Data with Varying Ranges The output factors ψ_{exp} , which belong to the research reference measurements \mathcal{M}_{Res} , are predicted within 3% accuracy. Systematic deviations between the simulated and the measured output factors are observed. In the first part of \mathcal{M}_{Res} (varying R_{req} , constant $M_{\text{req}} = 4$ cm) a linear decrease of $\Delta\psi_{\text{rel}}$ with increasing R_{req} is observed at the Options 3,4,7. At Options 1,2,5,6, $\Delta\psi_{\text{rel}}$ stays approximately constant with increasing R_{req} . For different field ranges R_{req} , the simulated MU in the IC23 volume MU_{sim} and the calibration dose in

the water phantom changes D_{sim} .

$$\psi_{\text{sim}} = \frac{D_{\text{sim}}}{\text{MU}_{\text{sim}}} \quad R_{\text{req}} = \text{varying} \wedge M_{\text{req}} = \text{const.} \iff D_{\text{sim}} \neq \text{const.} \wedge \text{MU}_{\text{sim}} \neq \text{const.} \quad (5.2)$$

Therefore, it is impossible to distinguish, whether an uncertainty in the prediction of D_{sim} or of MU_{sim} contributes more to $\Delta\psi_{\text{rel}}$. Both parameters are influenced by the beam current modulation (BCM). Uncertainties in the IC23 TOPAS scoring volume only effect MU_{sim} . The absence of a linear decreasing $\Delta\psi_{\text{rel}}$ with increasing R_{req} in Options 1,2,5,6, can be caused, because the proton scattering is mapped more precisely in those options. Another possibility is, that the uncertainties of D_{sim} and MU_{sim} superimpose and neutralize each other. The fluctuations of the $\Delta\psi_{\text{rel}}$ values, which belong to the representative volumes V_{IC23_1} and V_{IC23_2} illustrate the requirement of applying a higher Monte-Carlo statistics, when simulating MU values for those volumes and fields.

Research Reference Data with Varying Modulations In the second part of \mathcal{M}_{Res} (varying M_{req} , constant R_{req}) a linear decrease of $\Delta\psi_{\text{rel}}$ is observed. This effect is obtained at different ranges R_{req} (Figure 4.13, H, I, J, K). For a data set with constant R_{req} and varying M_{req} , D_{sim} stays approximately constant. Therefore, the decrease in ψ_{rel} has to be explained with an uncertainty in the derivation of MU_{sim} .

$$\psi_{\text{sim}} = \frac{D_{\text{sim}}}{\text{MU}_{\text{sim}}} \quad M_{\text{req}} = \text{varying} \wedge R_{\text{req}} = \text{const.} \iff D_{\text{sim}} \approx \text{const.} \wedge \text{MU}_{\text{sim}} \neq \text{const.} \quad (5.3)$$

A systematically increasing error of the predicting of the MU signal in TOPAS, can be induced by an increasing uncertainty of the beam current modulation or an error in the mapping of the charge collection, which changes for different beam energies.

The beam current modulation compensates scattering effects from the square apertures, which have a larger impact on the dose distribution as the modulation decreases. Therefore, the accuracy of the simulated particle fluence in the scoring volume might decrease for small modulations.

An error in the mapping of the MU charge collection in TOPAS could change with increasing M_{req} , because the mean field scattering angle Θ_0 depends on the range modulation wheel time digit t_{digit} . The low-range PP have to be scattered with higher angles in order to deposit dose profiles in the water phantom, with similar lateral extensions, as the high-range PP. Therefore, the fluence per surface ϕ_A changes within the distal extension of the scoring volume, time dependently. Θ_0 , and therefore ϕ_A , depends on R_{req} , M_{req} and t_{digit} . The change of ϕ_A in a scorer with the distal extension $\Delta z = z_2 - z_1$ is derived in Equation (5.4). A change of Θ_0 within the scorer due multiple Coulomb scattering (MCS) is negligible because of low density of the air in the ion chamber.

$$\Delta\phi_A = \phi_A^{z_2} - \phi_A^{z_1} = \phi \left(\frac{1}{A_2} - \frac{1}{A_1} \right) = \phi \left(\frac{1}{\pi r_2^2} - \frac{1}{\pi r_1^2} \right) = \frac{\phi}{\pi \tan^2(\Theta_0)} \left(\frac{1}{z_2^2} - \frac{1}{z_1^2} \right) \quad (5.4)$$

If the distal extension of the IC23 scorer is small enough, the proton stopping power can be approximated as to be constant. Therefore, the change in the dose per surface D_A can be derived.

$$S \approx \text{const.} \iff \Delta D_A \approx \frac{S}{\rho} \cdot \Delta\phi_A \quad (5.5)$$

The assumption of a constant stopping power becomes worst with increasing distal scorer extension.

In addition the fluence loss due nuclear interactions get inhomogeneous if the distal energy distribution is no longer mono-energetic. The depth-dose distribution in the scorer has a negative slope, which increases with increasing modulation. Therefore, MU_{sim} depends on the distal scorer extension and M_{req} . The lateral size of the IC23 volume should be small enough to ensure, that the lateral fluence distribution is homogeneous. Therefore, one has to keep in mind, that the spatial spread of the beam profile, which is measured in the IC23 decreases with increasing requested field range. In addition, a cylindrical shaped scorer would better map the cylindrical beam symmetry, and therefore the charge collection, as a cubic one.

There is an option dependency of the relative errors $\Delta\psi_{rel}$, which belong to \mathcal{M}_{Ref} and \mathcal{M}_{Res} . The application of option dependent calibrations improves the accuracy of the output factor prediction by 1%. It is difficult to exactly determine the origin of this option dependency. Nevertheless, it is important to have a strong argument to implement any option corrections in the Monte-Carlo model. If the ion chamber gets calibrated within every nozzle option separately, this would be a justification for the implementation of option dependent correction factors.

Patient Quality Assurance Reference Data The field output factors, which belong to the patient QA measurements for Patient 1, are predicted within the measurement uncertainty of 1%. As small linear slope of ψ_{rel} with increasing z_{calib} is observed. As the simulated dose in the ion chamber is similar for all the four output factors, the slope is related to a small uncertainty of the simulated dose distribution in the water.

5.3 TOPAS Simulation of a Proton Treatment Plan

The absolute dose of the planned dose distribution for Patient 1 is predicted with gamma pass rates above 95% at the high dose regions when applying a local gamma criteria of 1 mm and a dose criteria of 3%. This accuracy is achieved for the majority of the compared dose image slices ($\geq 75\%$). A drop of the gamma pass rates is observed at the upper head region, where large material density gradients (bone-tissue, bone-air, bone-pillow) dominate. At the distal and lateral field edges systematic deviations are observed. The simulated dose profiles show stripes, which correspond to dose fluctuations in the order of 2%. They appear too large to be solely explained with statistical dose fluctuations of the Monte-Carlo simulations. Simulated distributions of the linear energy transfer (LET) and calculated variable relative biological effectiveness (RBE) distributions in the patient show accurate agreement with the literature.

Planned Dose Distribution The planned dose distribution in the patient is used to characterize the results of the Monte-Carlo simulation, because no data exists on the measured dose in the patient. The beam model in the treatment planning system (TPS), which generates the planned dose distribution, contains assumptions, especially for the lateral penumbras, where multiple Coulomb scattering effects dominate. Those assumptions generate uncertainties in the prediction of the lateral penumbras. In addition, deterministic algorithms model scattering effects less accurately, which occur in regions that contain high material density gradients.

A systematic deviation between the planned and the Monte-Carlo simulated dose distributions at the

lateral field edges is observed on all image slices for the proton plan of Patient 1 (Figure 4.19). Such deviations also show up in a second simulated prostate boost plan that is visualized in the appendix (Figure P). For the plan of Patient 1, in particular at the upper head region, systematic deviations at high density gradients between bone, tissue, pillow and air material occur. The differences between deterministic and Monte-Carlo algorithms in predicting dose distributions for proton therapy, are discussed in Ref. [2] in more detail. The planned distribution cannot be used to validate the simulated dose distribution in the patient. Nevertheless, the comparison of the overall shape of the planned and the simulated dose distribution serves as a test of the functioning of the automated proton plan integration in TOPAS. In Figure 4.20 it is shown, that a shift of the TOPAS dose grid by one voxel in any spatial direction would systematically increase the dose differences. Therefore, the patient positioning in the simulation relative to the treatment field appears to be correct, within the resolution of one voxel, which is 2 mm.

The planned dose distribution by the TPS is a reasonable reference to compare the absolute simulated doses in the central high field dose region. In the high field dose region of the proton plan of Patient 1, there are no large tissue density gradients. In addition, generic uncertainties of the TPS beam model in the prediction of the proton scattering have a small influence on the accuracy of the predicted doses in the central field plateau region.

Gamma Analysis To quantify the difference between the planned and the simulated dose distributions, gamma analyzes are performed. The gamma analysis is a tool is widely used in daily clinical routine [47] and is applied to asses the simulated dose distributions from a clinical point of view. When applying a geometrical gamma criteria of 1 mm and a dose criteria of 3%, gamma pass rates above 95 % are achieved for all images, which correspond to the central high dose region (dose threshold criteria of 50 %). This accuracy is still achieved, when including the proximal regions of the field in the gamma analysis (dose threshold of 0 %). Therefore, TOPAS reproduces the planned dose distribution of the proton plan of Patient 1 within the tolerances ($\lambda_{x,y,z} = 1 \text{ mm} \mid \lambda_D = 3 \% \mid \lambda_{\text{th}} = 0\%$) when excluding images which belong to the upper head region. In the upper head region there are large material density gradients between bone, tissue, pillow and air materials. For this region an accurate comparison between the planned and simulated dose is not possible. For all applied gamma criteria the gamma pass rates for images, which belong to the upper head region drop down dramatically (Figure 4.23). A further reduction of the geometrical criteria below 1 mm leads to gamma pass rates below 95 % for all image slices. Spatial uncertainties at the plateau edges contribute more to the gamma pass rate for strict local criteria. Besides the deviations between Monte-Carlo and the TPS, uncertainties of the simulation itself are resolved at higher spatial resolution. The field sizes of the measured lateral profiles in the water phantom are predicted in TOPAS to be within 0.9 mm. In the patient, the lateral uncertainty is expected to be similar. An uncertainty in the implemented TOPAS stopping powers for different materials might even increase the geometrical uncertainty. Nevertheless, the deviations between the adopted TOPAS stopping powers and relative mass densities and the values that are implemented in the TPS are small, at least for the majority of the tissue materials in the planned target volume of Patient 1 (Figure 3.31, 3.32). The angle between the two treatment fields is close to 90°. Therefore, it is difficult to decide, whether a dose difference originates from a deviation in the lateral profiles or in the range. To distinguish between the influences of lateral and range uncertainties, the simulated treatment fields have to be compared

to the planned ones separately in a further study. In a water phantom the treatment planning system models the range more precisely compared to the lateral profiles edges. In the homogenous glioma tissue this relation can be assumed to be similar, at least in first approximation. In the current TOPAS model (Table 3.2), the range is predicted with higher accuracy to compared to the lateral field sizes and lateral penumbras. Because the stopping powers of the TPS and TOPAS are similar, the range uncertainty can be expected to be smaller compared to the lateral one.

When further reducing the dose criterion λ_D of the gamma analysis, the gamma pass rate drops dramatically. First, dose uncertainties at the plateau edges contribute more for small λ_D . Second, systematic dose fluctuations occur in the simulated dose distribution with amplitudes of about 2%. A convergence analysis for the first treatment field is performed, to test whether these fluctuations are purely statistical (Figure 4.21). 1D curves are compared for 10^6 , 10^7 , $5 \cdot 10^7$ and 10^8 protons, which are reaching the patient. An increase of the proton number from 10^6 to 10^7 reduces the dose fluctuations from about 8% to 2%. An increase of the proton number by a factor five reduces the uncertainty to 1.5%. Further enlarging (to 10^8) reduces the uncertainty by 0.05%. Therefore, the simulation is considered as converged for 10^8 proton, which are reaching the patient. To test the dependency of the fluctuations on the binning size, the simulations should be repeated by using smaller dose bins in the patient dose scoring component in TOPAS. Currently, the dose grid, which is used in the simulation is similar to that of the TPS. In addition, a higher Monte-Carlo resolution have a benefit in characterizing spatial deviations between the simulated and planned dose distributions more precisely. The obtained dose stripes in the Monte-Carlo might have a physical origin. To quantify this hypothesis, the dose fluctuations of the measured lateral profiles have to be characterized more precisely. The absence of such dose stripes in the planned dose distribution can be explained by the fact, that the TPS flattens the plateau region of the measured lateral input data, in order to generate its beam model. This would justify the application of image filters, when comparing the simulated distributions to planned ones as illustrated in Figure 4.22. The lateral profile of a spread-out Bragg peak is generated in double-scattering by superimposing various Gaussian profiles. The observed fluctuations might correspond to the maximum achievable flatness of this procedure, for the double-scattering system at UPTD. In Ref.[49] a simulated double-scattering proton plan (Monte-Carlo) is compared to a planned one (XiO) and similar dose stripes are observed in the central high-dose region of the simulated profiles. The simulated double-scattering system is comparable to the one, which is used at UPTD (Ion Beam Applications universal nozzle in double-scattering mode). Another possible origin of the stripes could be the compensator. Nevertheless, this can not explain the stripes which are obtained in Figure 3.27 for the patient QA simulations, where no compensator is used.

For the first treatment field, the simulated absolute dose overestimates the planned absolute dose in the proximal shoulder region by 1%. For the second field, the absolute planned dose at the proximal shoulder region is underestimated by about 1%. It is difficult to decide, whether these deviations correspond to an uncertainty of the beam weights or to an uncertainty of the beam current modulation. A separate comparison of the dose distributions of the single planned and simulated fields should be performed to distinguish between those two uncertainties.

The gamma analysis has its benefit in order to judge the simulated dose distribution in the patient from a clinical point of view. However, the information that can be extracted from a gamma

analysis is limited, because a lot of different effects are merged in one parameter. To further study spatial and dose uncertainties in more detail planned and simulated lateral and depth-dose distributions has to be compared for each treatment field, separately. In a first step, the absolute dose distribution should be compared in the water phantom in order to quantify the impact of the patient anatomy on the dose deviations.

LET and RBE Distributions The values of the simulated dose-averaged linear energy transfer (LET) and calculated relative biological effectiveness distributions show accurate agreement when compared to similar treatment fields in the literature [6]. The LET increases up to values of $10 \text{ keV}/\mu\text{m}$ and the distribution shows spikes at the profiles edges (Figure 4.24, left sub-plots). The highest LET values are observed in regions where high-LET areas of the single treatment fields superimpose. LET hot spots are produced, by low-energy protons stopping in the patient pillow and protons at the distal end of the overshoots. To validate the accuracy of the simulated LET distributions in patients one can simulate and compare proton plans from other proton therapy facilities, which use a similar Monte-Carlo simulation model of the beam source and the treatment head.

Hot spots of the calculated variable RBE distribution are observed in regions with high LET spikes (Figure 4.24, center sub-plots). At the central region of the treatment field the variable RBE stays approximately constant (1.1). It increases to values up to 1.6 at the distal field edges. In addition, RBE values below 1.1 are obtained in the target volume. The dose (RBE), which is predicted by using the variable RBE model is up to 15% larger compared to the predicted dose (RBE) of the constant RBE model in the distal-edges of the high-dose region. Therefore, the usage of a variable RBE induces a small shift in the field range. Besides the physical uncertainty of the simulated LET distribution, the RBE model itself introduces uncertainties. For the applied model the biological data originates from in vitro cell experiments of glioma cells. The accuracy of the description of full tumor biology based on single cell experiments is limited. However, the variability of the RBE with LET (and dose) is a systematic effect and is also expected to occur in the patient. The question remains how large the RBE depends on the absolute dose and the LET in the patient. This depends of course also very much on the end point for the effect of interest (organ, tumor, ...). This simulation tool represents a solid basis for future RBE studies in patients by providing spatial distributions of the physical quantities that determine the radiobiological effect of proton irradiation.

6 Summary and Conclusion

The commissioned Monte-Carlo model of the treatment head at the University Proton Therapy Dresden (UPTD) predicts measured relative dose distributions in a water phantom within the clinical tolerances. Therefore, an adjustment of the initial beam energy distribution, single scatter foils and the time-dependent modulation of the beam current is sufficient. No further adjustments of the nozzle geometries have to be applied. The plateau regions and the ranges of the measured depth-dose distributions are predicted within the measurement uncertainty. Systematic dose deviations at the proximal shoulder region are an indicative, that the square apertures, which are used in the measurements, have a non-negligible impact on the shape of the depth-dose curves, even if they are scored in volumes along the beam axis with small lateral extensions. The deviations in the proximal shoulder regions are generating uncertainties in the calculation of the Monte-Carlo specific beam current modulation functions. Those uncertainties can be reduced by limiting the domain of the fit that is used to derive the beam current modulation weights to a central plateau region. Nevertheless, the derived current weights do not fully represent the experimental situation and systematic dose deviations are induced by those weight uncertainties in the plateau regions, too, especially for depth-dose distributions with low ranges.

Deviations of the ranges R_{90} and R_{20} at the distal fall-off region up to 0.54 mm are an indicative, that the initial beam energy distribution has to be further optimized in order to predict the complete distal fall-off region within the measurement uncertainty in all nozzle options. To increase the accuracy of the prediction of the full depth-dose curves in a water phantom, the calculation of the beam current modulation functions have to be repeated by using the same apertures that are used in the measurements. Before that, the initial beam energy distribution has to be further optimized to increase the accuracy in the distal-fall region for each simulated pristine Bragg peak, which is used as a base function of the fit in order to determine the optimal beam current weights.

An improvement of the accuracy of the beam current modulation will increase the accuracy of the output factor prediction in the the simulation, which is currently in the order of 3%. It can be improved to 2%, when applying nozzle option-dependent calibration factors. Nevertheless, the application of option-dependent corrections in the Monte-Carlo model has to be justified. An sufficient argument would be if the ion chamber IC2 is calibrated separately within every option during the quality assurance of the nozzle machine. Dependencies of the relative error of the simulated output factors on the shape and position of the active scoring volume in the Monte-Carlo ion chamber model are observed. In addition, the relative errors show a dependency on the field size. In order to improve the output factor prediction in the simulation, the shape and the position of the active volume has to be further optimized. The combined optimization of the beam current modulation and the active Monte-Carlo scoring volume might have the potential to increase the accuracy of the absolute dose simulation in order to be able to predict the output factors within the clinical tolerance

of 1%. This would have a large clinical benefit, because currently the output factors have to be measured for each treatment field and those measurements require up to 20% of the full treatment time at UPTD. Even, if a stand alone Monte-Carlo solution will not be able to predict the output factors accurately, it can evolve its benefit when combined with theoretical models. Those models are already applied at different facilities [30, 50] and allow to obtain output factors within 1.5% accuracy for a majority of the treatment fields. Monte-Carlo simulations can improve those models in predicting essential dependencies of the model parameters. Especially, the output factor dependency on near-field scattering effects from the apertures has to be better understood.

The position of the simulated dose distribution relative to planned one of the treatment planning system (TPS), is predicted in the Monte-Carlo model within the accuracy of one dose image voxel, which is 2 mm. Therefore, the automated patient positioning and integration of patient specific components in the Monte-Carlo simulation is accurate, at least within 2 mm accuracy. The absolute planned dose at the high dose region of the treatment field is predicted within the clinical tolerances, which is validated based on a gamma analysis. A gamma analysis is a sufficient method to judge the simulated dose distribution from a clinical point of view. The central field plateau region of the absolute planned dose distribution is predicted with gamma pass rates above 95%, when applying a local gamma criterion of 1 mm and a dose criterion of 3%.

At the lateral and distal field edges and at regions with high material density gradients, systematic deviations between the simulated and the planned dose distributions are obtained. Those effects occur basically due to differences in the modeling of the proton scattering and emphasizes the benefit of using Monte-Carlo simulations in the daily clinical routine to monitor the influence of the scattering on the dose deposition in the patient more precisely. To systematically analyze lateral and distal deviations between the simulated and planned dose distributions, the single treatment fields should be compared separately, first in a water phantom and second in the patient.

Systematic dose fluctuations up to 2% occur in the simulated dose profiles in the patient. They appear too large to be solely explained with statistical dose fluctuations of the Monte-Carlo simulations. To determine if those fluctuations have a physical origin, a more precise characterization of the dose fluctuations of the measured lateral profiles is required. When comparing Monte-Carlo and the TPS, it is justified to apply smoothing filters to the simulated distributions, because they are used in the TPS, too, in order to generate its beam model. The adequacy of this comparison will benefit from a further improvement of the accuracy of the implemented TOPAS stopping powers and relative mass densities.

For one proton plan the simulated distribution of the linear energy transfer (LET) and the corresponding variable relative biological effectivenesses (RBE) show accurate agreement to similar treatment fields in the literature. When using biological data, which originates from in-vitro cell experiments, RBE hot spots up to 1.6 are obtained at the distal plateau edges and values below 1.1 occur in the target volume. In summary, this simulation tool represents a solid basis for future RBE studies in patients by providing spatial distributions of the physical quantities that determine the radiobiological effect of proton irradiation.

Bibliography

- [1] Michael Baumann, Mechthild Krause, Jens Overgaard, M. Debus Juergen and Soren, M. Bentzen, Juliane Daartz, Christian Richter, Daniel Zips, and Thomas Bortfeld. “Radiation oncology in the era of precision medicine”. In: *Nature Reviews Cancer* (2016).
- [2] Harald Paganetti. “Range uncertainties in proton therapy and the role of Monte Carlo simulations.” In: *Physics in Medicine and Biology* 57 (2012).
- [3] Joost M. Verburg. “Reducing Range Uncertainty in Proton Therapy”. PhD thesis. Technische Universiteit Eindhoven, 2015.
- [4] Fernando Hueso-González, Fine Fiedler, Christian Golnik, Thomas Kormoll, Guntram Pausch, Johannes Petzoldt, Katja E. Römer, and Wolfgang Enghardt. “Compton Camera and Prompt Gamma Ray Timing: Two Methods for In Vivo Range Assessment in Proton Therapy”. In: *Frontiers in Oncology* 80 (2016).
- [5] Sonja M Schellhammer and Aswin L Hoffmann. “Prediction and compensation of magnetic beam deflection in MR-integrated proton therapy: a method optimized regarding accuracy, versatility and speed.” In: *Physics in Medicine and Biology* 62 (2017).
- [6] Paganetti Harald. “Relative biological effectiveness (RBE) values for proton beam therapy. Variations as a function of biological endpoint, dose, and linear energy transfer.” In: *Physics in Medicine and Biology* 59 (2014).
- [7] J. Perl, J. Shin, Schumann J., Faddegon B., and Paganetti H. “TOPAS: an innovative proton Monte Carlo platform for research and clinical applications”. In: *Medical Physics* 39 (2012).
- [8] C. Patrignani. “The Review of Particle Physics”. In: *Journal of Physics* 40 (2016).
- [9] F. Bethe. “Zur Bremsung rasch bewegter Teilchen beim Durchgang durch Materie”. In: *Annalen der Physik* 408 (1933).
- [10] ICRU. *Stopping Power and Ranges for Protons and Alpha Particles*. 1984.
- [11] Harald Paganetti. *Proton Therapy Physics*. 2012.
- [12] G. Molière. “Theorie der Streuung schneller geladener Teilchen I Einzelstreuung am abgeschirmten Coulomb-Feld.” In: *Zeitschrift für Naturforschung* 3a (1948).
- [13] Stephen M. Seltzer. “An assessment of the role of charged secondaries from non-elastic nuclear interactions by therapy proton beams in water.” In: *NIST technical note NISTIR 5221* (1993).
- [14] Bortfeld T. “An analytical approximation of the Bragg curve for therapeutic proton beams”. In: *Medical Physics* (1997).
- [15] Hans Babovsky. *Die Boltzmann-Gleichung*. 1998.
- [16] Medical Systems Varian. *ProtonTherapy Scattering vs Scanning*. 2011.

- [17] Bortfeld T. and Schlegel W. "An analytical approximation of depth-dose distributions for therapeutic proton beams". In: *Physics in medicine and biology* (1996).
- [18] Jette D. and Chen W. "Creating a spread-out Bragg peak in proton beams". In: *Physics in Medicine and Biology* 56 (2011).
- [19] Michael Joiner and Albert van der Kogel. *Basic Clinical Radiobiology*. 4th ed. 2009.
- [20] Kellerer A. "Theoretische Aspekte der Strahlenbiophysik." In: *Biophysikalischer Grundlagen der Medizin*. 1980.
- [21] SB. Curtis. "Lethal and potentially lethal lesions induced by radiation—a unified repair model." In: *Radiation Research* 119 (1989).
- [22] Chaudhary P., Marshall T. I., Perozziello F. M., Manti L., Currell F. J., Hanton F., McMahon S. J., Kavanagh J. N., Cirrone G. A., Romano F., Prise K. M., and Schettino G. "Relative biological effectiveness variation along monoenergetic and modulated Bragg peaks of a 62-MeV therapeutic proton beam: a preclinical assessment." In: *International Journal of Radiation Oncology* 90 (2014).
- [23] J. B. Robertson, J. R. Williams, R. A. Schmidt, Little J. B., D. F. Flynn, and H. D. Suit. "Radiobiological studies of a high-energy modulated proton beam utilizing cultured mammalian cells.." In: *Radiation Research* 35 (1975).
- [24] T Kanai, Y. Furusawa, K. Fukutsu, H. Itsukaichi, K. Eguchi-Kasai, and H. Ohara. "Irradiation of mixed beam and design of spread-out Bragg peak for heavy-ion radiotherapy." In: *Radiation Research* 147 (1997).
- [25] Y Kanai, N. Kanematsu, Kanai T., and Matsufuji N. "Biological dose calculation with Monte Carlo physics simulation for heavy-ion radiotherapy." In: *Physics in Medicine and Biology* (2006).
- [26] N. Tilly, J. Johansson, U. Isacson, Medin J., E. Blomquist, and E. Grusell. "The influence of RBE variations in a clinical proton treatment plan for a hypopharynx." In: *Physics in Medicine and Biology* 50 (2005).
- [27] Yoshihisa Takada. "Dual-Ring Double Scattering Method for Proton Beam Spreading". In: *Journal of Applied Physics* 33 (1994).
- [28] Erik Grusell, Anders Montelius, Anders Brahme, Rikner Goeran, and Kellie Russell. "A general solution to charged particle beam flattening using an optimized dual-scattering-foil technique, with application to proton therapy beams". In: *Physics in Medicine and Biology* 39 (1994).
- [29] Östen Hakan. "In vivo Simulation der relativen biologischen Wirksamkeit der Protonentherapie mittels der Monte Carlo Methode". masterthesis. Technische Universität Dresden, 2015.
- [30] Kooy Hanne M, Rosenthal Stanley J, Engelsman Martijn, Mazal Alejandro, Slopsema Roelf L, Paganetti Harald, and Flanz Jacob B. "The prediction of output factors for spread-out proton Bragg peak fields in clinical practice". In: *Physics in Medicine and Biology* 50 (2005).
- [31] Kooy Hanne M, Schaefer Matthew, Rosenthal Skip, and Bortfeld Thomas. "Monitor unit calculations for range-modulated spread-out Bragg peak fields". In: *Physics in Medicine and Biology* 48 (2003).

- [32] Daartz J., Engelsman M., Paganetti H., and Bussière M. R. “Field size dependence of the output factor in passively scattered proton therapy: influence of range, modulation, air gap, and machine settings.” In: *Medical Physics* 36 (2009).
- [33] M. Testa, Schümann J., Lu H. M., Shin J., Faddegon B., Perl J., and Paganetti H. “Experimental validation of the TOPAS Monte Carlo system for passive scattering proton therapy”. In: *Medical Physics* 40 (2013).
- [34] Geant4 Collaboration. *Geant4 User’s Guide for Application Developers*. 2015.
- [35] Geant4 Collaboration. *Physics Reference Manual*. 2015.
- [36] Christina Jarlskog Zacharatou and Harald Paganetti. “Physics Settings for Using the Geant4 Toolkit in Proton Therapy”. In: *IEEE Transactions of Nuclear Science* 55 (2008).
- [37] Geant4 Collaboration. *Physics Reference Manual*. 2014.
- [38] Perl Joseph, Shin Jungwook, Schümann Jan, Ramos José, Hall David, Biegun Aleksandra, and Guan Fada. *User Guide for TOPAS Version 2.0 (rev. 20151104a)*. 2015.
- [39] Perl Joseph, Shin Jungwook, Schümann Jan, Ramos José, Hall David, Biegun Aleksandra, and Guan Fada. *User Guide for TOPAS Version 3.0 (rev. 20160522b)*. 2016.
- [40] Geant4 Collaboration. *Geant4 User’s Guide for Application Developers*. 2014.
- [41] José Ramos-Méndez, Joseph Perl, Bruce Faddegon, Jan Schümann, and Harald Paganetti. “Geometrical splitting technique to improve the computational efficiency in Monte Carlo calculations for proton therapy”. In: *Medical Physics* 40 (2013).
- [42] Jan Eulitz. “Introduction of a method for simulation of the proton therapy gantry at the Oncoray Dresden based on the Monte-Carlo-Tool TOPAS”. In: *Bachelor Thesis* 1 (2011).
- [43] Zhang R. and Newhauser W. D. “Calculation of water equivalent thickness of materials of arbitrary density, elemental composition and thickness in proton beam irradiation”. In: *Physis in Medicine and Biology* (2009).
- [44] Paganetti Harald. “Monte Carlo calculations for absolute dosimetry to determine machine outputs for proton therapy fields”. In: *Physis in Medicine and Biology* 51 (2006).
- [45] U Schneider, E. Pedroni, and A. Lomax. “The calibration of CT Hounsfield units for radiotherapy treatment planning.” In: *Physis in Medicine and Biology* 41 (1996).
- [46] Patrick Wohlfahrt, Christian Moheler, Volker Hietschold, Stefan Menkel, Steffen Greilich, Mechthild Krause, Michael Baumann, Wolfgang Enghardt, and Christian Richter. “Clinical Implementation of Dual-energy CT for Proton Treatment Planning on Pseudo-monoenergetic CT scan.” In: *International Journal of Radiation Oncology* 97 (2016).
- [47] D.A. Low, W.B. Harms, S. Mutic, and J.A. Purdy. “A technique for the quantitative evaluation of dose distributions.” In: *Medical Physics* 25 (1998).
- [48] International Commission on Radiation units and measurements. *Prescribing, Recording, and Reporting Proton-Beam Therapy*. Research Note. ICRU, 2009.
- [49] Chul Min Hee, Harald Paganetti, Brian Winey, Judith Adams, Shannon M. MacDonald, Nancy J. Tarbell, and Torunn I. Yock. “Evaluation of permanent alopecia in pediatric medulloblastoma patients treated with proton radiation.” In: *Radiation Oncology* 9 (2014).

- [50] Liyong Lin, JiaJien Shen, G. Christopher Ainsley, Timothy D. Solberg, and James E. McDonough. “Implementation of an improved dose-per-MU model for double-scattered proton beams to address interbeamline modulation width variability”. In: *Journal of Applied Clinical Medical Physics* 15 (2013).

Acknowledgment

I would like to express my gratitude to my first supervisor Dr. Armin Lühr for the long and lively discussions, expedient ideas, hard questions, motivating words and funny jokes during my master thesis. I would like to thank my second supervisor Dr. Benjamin Lutz for the great software support, the useful and critical comments and the providing of such an accurate model of the IBA nozzle. Besides my supervisors, I would like to thank my referees Prof. Dr. Arno Staessner and Prof. Dr. Wolfgang Enghardt for their encouragement, insightful comments, and hard questions. Furthermore I would like to thank Steffen Löck, Julia Hytry, Patrick Wohlfahrt, Hakan Östen and Daniela Kunath for answering questions, helping with software related issues and providing clinical informations. Furthermore I would like to thank again Dr. Armin Lühr and Dr. Benjamin Lutz and Markus Firmbach for the endurance to check this thesis for content, style, spelling and grammar uncertainties. In addition, I want to thank Sebastian Gantz and Lukas Dünger for the small amount of Quizzduell-matches, which I was able to win, and the group of Dr. Guntram Pausch for the pleasant lunch breaks. Finally, I would like to thank my family for their continuous support during my studies and Janneke Grau for all those beautiful moments in the last year.

Dresden, March 15, 2017

Selbständigkeitserklärung

Ich versichere, dass ich die vorliegende Arbeit selbständig verfasst und keine anderen als die angegebenen Quellen und Hilfsmittel benutzt habe. Ich reiche sie erstmals als Prüfungsleistung ein. Mir ist bekannt, dass ein Betrugsversuch mit der Note "nicht ausreichend" (5,0) geahndet wird und im Wiederholungsfall zum Ausschluss von der Erbringung weiterer Prüfungsleistungen führen kann.

Dresden, March 9, 2017

=====

Appendix

A Adjustment and Validation of TOPAS Depth-Dose Distributions

Table A: IBA nozzle options and sub-Options , including the lowest and highest achievable range R_{min}/R_{max} , the second scatterer component (SS ID), the range modulation wheel track (Track ID) and the ID of the beam current modulation functionfile name (BCM ID).

Option	SS ID	Track ID	Sub-Option	R_{min}/cm	R_{max}/cm	BCM ID
1	SS2	Track7	1.1	4.6	4.99	BCMod11
			1.2	4.99	5.41	BCMod12
			1.3	5.41	5.87	BCMod13
2	SS2	Track7	2.1	5.87	6.37	BCMod21
			2.2	6.37	6.91	BCMod22
			2.3	6.91	7.49	BCMod23
3	SS2	Track4	3.1	7.49	8.12	BCMod31
			3.2	8.12	8.81	BCMod32
			3.3	8.81	9.55	BCMod33
4	SS2	Track5	4.1	9.55	10.32	BCMod41
			4.2	10.32	11.09	BCMod42
			4.3	11.09	11.86	BCMod43
5	SS3	Track4	5.1	11.86	13.09	BCMod51
			5.2	13.09	14.32	BCMod52
			5.3	14.32	15.54	BCMod53
6	SS3	Track5	6.1	15.54	16.86	BCMod61
			6.2	16.86	18.28	BCMod62
			6.3	18.28	19.83	BCMod63
7	SS3	Track6	7.1	19.83	21.18	BCMod71
			7.2	21.18	22.61	BCMod72
			7.3	22.61	23.91	BCMod73
8	SS4	Track8	8.1	23.91	24.67	BCMod81
			8.2	24.67	26.54	BCMod82
			8.3	26.54	28.4	BCMod83

Table B: Requested ranges R_{req} and requested modulations M_{req} of all reference and validation data depth-dose distributions (spread-out Bragg peaks).

Sub-Option	R_{req}/cm Reference	M_{req}/cm Reference	R_{req}/cm Validation	M_{req}/cm Validation
1.1	4.9	4.9	4.6	3.2
1.2	5.4	5.4	5.0	3.2
1.3	5.8	5.8	5.5	3.8
2.1	6.3	6.3	5.9	4.0
2.2	6.9	6.9	6.4	4.4
2.3	7.4	7.4	7.0	4.8
3.1	8.1	8.1	7.5	5.0
3.2	8.8	8.8	8.2	5.6
3.3	9.5	9.5	8.9	5.9
4.1	10.3	10.3	9.6	6.5
4.2	11.0	11.0	10.4	6.8
4.3	11.8	11.8	11.1	7.4
5.1	13.0	13.0	11.9	8.0
5.2	14.3	14.3	13.1	8.6
5.3	15.5	15.5	14.4	9.5
6.1	16.8	16.8	15.6	10.4
6.2	18.2	17.0	16.9	11.5
6.3	19.8	17.0	18.3	11.5
7.1	21.1	17.0	19.9	11.5
7.2	22.6	15.0	21.2	11.5
7.3	23.9	15.0	22.7	10.1
8.1	24.6	15.0	24.0	10.1
8.2	26.5	15.0	24.7	10.1
8.3	28.0	15.0	26.6	10.1

Table C: Requested ranges R_{req} , requested modulations M_{req} and the requested depth position points z_{pos} of the validation data lateral profiles.

R_{req}/cm	M_{req}/cm	z_{pos}/cm	R_{req}/cm	M_{req}/cm	z_{pos}/cm
5.0	1.8	1.0	5.0	3.4	1.0
5.0	1.8	3.2	5.0	3.4	1.6
5.0	1.8	4.1	5.0	3.4	3.3
6.4	2.2	1.0	6.4	4.4	1.0
6.4	2.2	4.2	6.4	4.4	2.0
6.4	2.2	5.3	6.4	4.4	4.2
8.2	2.8	1.0	8.2	5.6	1.0
8.2	2.8	5.4	8.2	5.6	2.6
8.2	2.8	6.8	8.2	5.6	5.4
10.4	3.6	1.0	10.4	6.8	1.0
10.4	3.6	6.8	10.4	6.8	3.6
10.4	3.6	8.6	10.4	6.8	7.0
13.1	4.4	1.0	13.1	8.6	1.0
13.1	4.4	8.7	13.1	8.6	4.5
13.1	4.4	10.9	13.1	8.6	8.8
16.9	5.6	1.0	16.9	11.5	1.0
16.9	5.6	6.0	16.9	11.5	5.4
16.9	5.6	11.3	16.9	11.5	11.2
21.2	5.6	1.0	21.2	11.5	1.0
21.2	5.6	8.3	21.2	11.5	9.7
21.2	5.6	15.6	21.2	11.5	15.5
24.7	5.0	1.0	24.7	10.1	1.0
24.7	5.0	10.4	24.7	10.1	14.6
24.7	5.0	19.7	24.7	10.1	19.7

Table D: Comparison between adjusted simulated depth-dose curves to reference data measurements, including the mean value and standard deviation ($\mu_{D,\text{Plateau}}$, $\sigma_{D,\text{Plateau}}$) of the dose difference distribution in the central plateau region and the range offsets at the distal fall-off region ΔR_{90} , ΔR_{80} and ΔR_{20} .

R_{req}/cm	M_{req}/cm	$\mu_D \%$	$\sigma_D \%$	$\Delta R_{90}/\text{mm}$	$\Delta R_{80}/\text{mm}$	$\Delta R_{20}/\text{mm}$
4.9	4.9	0.03	0.33	0.09	0.00	0.01
5.4	5.4	-0.04	0.29	-0.03	0.00	0.00
5.8	5.8	0.02	0.25	-0.10	0.01	0.09
6.3	6.3	-0.03	0.29	-0.02	0.00	0.05
6.9	6.9	-0.03	0.25	-0.12	0.00	0.10
7.4	7.4	-0.02	0.25	-0.14	0.00	0.03
8.1	8.1	-0.03	0.30	-0.16	0.00	-0.09
8.8	8.8	0.01	0.22	-0.11	0.00	-0.12
9.5	9.5	0.03	0.24	0.02	0.00	-0.18
10.3	10.3	0.04	0.33	0.01	0.00	-0.17
11.0	11.0	-0.01	0.29	0.05	0.00	-0.18
11.8	11.8	0.03	0.33	0.11	0.00	-0.27
13.0	13.0	-0.02	0.29	0.01	0.01	-0.46
14.3	14.3	0.00	0.29	-0.02	0.00	-0.35
15.5	15.5	-0.01	0.19	0.00	0.01	-0.43
16.8	16.8	0.09	0.23	0.08	0.01	-0.31
18.2	17.0	0.08	0.28	-0.02	0.01	-0.26
19.8	17.0	0.05	0.29	-0.09	0.01	-0.13
21.1	17.0	0.10	0.33	0.03	0.00	-0.14
22.6	15.0	0.03	0.26	-0.07	0.00	0.32
23.9	15.0	0.04	0.29	-0.02	0.00	0.44
24.6	15.0	0.17	0.26	0.00	0.00	-0.16
26.5	15.0	0.06	0.34	-0.19	0.00	0.09
28.0	15.0	0.15	0.32	-0.13	-0.01	0.48

Table E: Comparison between adjusted simulated depth-dose curves to validation data measurements, including the mean value and standard deviation ($\mu_{D,\text{Plateau}}$, $\sigma_{D,\text{Plateau}}$) of the dose difference distribution in the central plateau region and the range offsets at the distal fall-off region ΔR_{90} , ΔR_{80} and ΔR_{20} .

R_{req}/cm	M_{req}/cm	$\mu_D\%$	$\sigma_D\%$	$\Delta R_{90}/\text{mm}$	$\Delta R_{80}/\text{mm}$	$\Delta R_{20}/\text{mm}$
4.6	3.2	0.25	0.98	0.22	0.00	-0.12
5.0	3.2	0.05	0.45	0.06	0.00	-0.03
5.5	3.8	-0.11	0.36	-0.04	0.00	0.07
5.9	4.0	-0.02	0.8	-0.02	0.00	-0.08
6.4	4.4	-0.17	0.5	-0.09	0.00	-0.11
7.0	4.8	-0.13	0.48	0.00	0.00	-0.07
7.5	5.0	0.22	0.96	0.08	0.00	-0.25
8.2	5.6	0.26	0.97	0.01	0.00	-0.17
8.9	5.9	-0.06	0.91	-0.02	0.00	-0.13
9.6	6.5	-0.04	0.62	0.05	0.00	-0.26
10.4	6.8	-0.12	0.74	0.15	0.00	-0.34
11.1	7.4	-0.05	0.57	0.04	0.01	-0.27
11.9	8.0	-0.21	0.68	-0.15	0.00	-0.48
13.1	8.6	-0.2	0.74	-0.08	-0.01	-0.37
14.4	9.5	-0.19	0.83	0.04	0.01	-0.49
15.6	10.4	-0.18	0.57	0.22	0.01	-0.54
16.9	11.5	-0.1	0.48	0.08	0.00	-0.48
18.3	11.5	-0.18	0.71	0.15	-0.00	-0.31
19.9	11.5	-0.04	0.46	-0.02	0.00	-0.28
21.2	11.5	-0.07	0.46	-0.05	0.02	0.03
22.7	10.1	-0.24	0.85	-0.07	0.02	0.16
24.0	10.1	0.19	0.61	0.14	0.00	-0.33
24.7	10.1	0.13	0.40	0.09	0.00	-0.21
26.6	10.1	0.14	0.44	-0.02	0.00	0.23

Table F: Comparison between adjusted simulated lateral profiles and validation data measurements, including the mean value and standard deviation ($\mu_{D,\text{Plateau}}$, $\sigma_{D,\text{Plateau}}$) of the dose difference distribution in the central plateau region, the field size deviations ΔW_{50} (sim - exp) and the deviations in the lateral penumbras of the left ΔP_{left} and the right profile flanks ΔP_{right} . All values are listed for the x - and y - projection.

$R_{\text{req}} M_{\text{req}} z_{\text{pos}}$ cm	μ_D (x y) %	σ_D (x y) %	ΔW_{50} (x y) mm	ΔP_{right} (x y) mm	ΔP_{left} (x y) mm
5.0 1.8 1.0	-0.15 0.27	1.71 1.92	-0.75 - 0.52	-0.36 - 0.46	0.54 0.56
5.0 1.8 3.2	-0.34 0.27	1.63 1.72	-0.69 - 0.39	-0.55 - 0.32	0.52 0.42
5.0 1.8 4.1	-0.11 0.15	1.60 1.63	-0.63 - 0.48	-0.23 - 0.29	0.37 0.57
5.0 3.4 1.0	-0.01 0.28	1.54 1.83	-0.74 - 0.55	-0.27 - 0.55	0.46 0.63
5.0 3.4 1.6	0.17 0.02	1.54 1.55	-0.78 - 0.58	-0.51 - 0.37	0.56 0.39
5.0 3.4 3.3	-0.02 - 0.29	1.56 1.58	-0.65 - 0.53	-0.35 - 0.35	0.48 0.43
6.4 2.2 1.0	0.16 0.31	1.61 1.75	-0.85 - 0.63	-0.45 - 0.38	0.57 0.53
6.4 2.2 4.2	0.27 - 0.04	1.58 1.63	-0.65 - 0.45	-0.45 - 0.42	0.42 0.52
6.4 2.2 5.3	-0.23 - 0.16	1.51 1.67	-0.78 - 0.34	-0.42 - 0.76	0.63 0.88
6.4 4.4 1.0	0.31 0.23	1.40 1.66	-0.82 - 0.69	-0.46 - 0.43	0.44 0.43
6.4 4.4 2.0	0.20 0.04	1.62 1.60	-0.71 - 0.61	-0.35 - 0.32	0.52 0.53
6.4 4.4 4.2	0.00 - 0.23	1.37 1.40	-0.71 - 0.40	-0.35 - 0.46	0.56 0.51
8.2 2.8 1.0	0.18 0.38	1.54 1.85	-0.61 - 0.63	-0.37 - 0.20	0.56 0.47
8.2 2.8 5.4	-0.21 - 0.05	1.50 1.57	-0.70 - 0.80	-0.47 - 0.29	0.25 0.33
8.2 2.8 6.8	-0.11 - 0.23	1.58 1.67	-1.00 - 0.55	-0.44 - 0.12	0.42 0.47
8.2 5.6 1.0	-0.04 0.32	1.43 1.73	-0.76 - 0.49	-0.38 - 0.29	0.49 0.49
8.2 5.6 2.6	-0.07 - 0.01	1.39 1.68	-0.77 - 0.71	-0.44 - 0.50	0.44 0.51
8.2 5.6 5.4	-0.02 - 0.07	1.47 1.64	-0.77 - 0.58	-0.28 - 0.54	0.31 0.14
10.4 3.6 1.0	0.25 0.12	1.56 1.61	-0.65 - 0.53	-0.29 - 0.39	0.37 0.37
10.4 3.6 6.8	-0.11 - 0.11	1.29 1.25	-0.61 - 0.63	-0.21 - 0.41	0.24 0.19
10.4 3.6 8.6	0.27 - 0.04	1.47 1.42	-0.74 - 0.60	-0.25 - 0.38	0.26 0.46
10.4 6.8 1.0	0.25 0.07	1.45 1.53	-0.70 - 0.45	-0.39 - 0.44	0.43 0.43
10.4 6.8 3.6	-0.06 0.07	1.40 1.46	-0.74 - 0.50	-0.28 - 0.35	0.41 0.41
10.4 6.8 7.0	-0.07 - 0.05	1.23 1.28	-0.77 - 0.55	-0.28 - 0.53	0.16 0.42

Table G: Comparison between adjusted simulated lateral profiles and validation data measurements, including the mean value and standard deviation ($\mu_{D,\text{Plateau}}$, $\sigma_{D,\text{Plateau}}$) of the dose difference distribution in the central plateau region, the field size deviations ΔW_{50} (sim - exp) and the deviations in the lateral penumbras of the left ΔP_{left} and the right profile flanks ΔP_{right} . All values are listed for the x - and y - projection.

$R_{\text{req}} M_{\text{req}} z_{\text{pos}}$ cm	μ_D (x y) %	σ_D (x y) %	ΔW_{50} (x y) mm	ΔP_{right} (x y) mm	ΔP_{left} (x y) mm
13.1 4.4 1.0	0.09 0.18	1.47 1.59	-0.75 - 0.66	-0.36 - 0.37	0.36 0.26
13.1 4.4 8.7	-0.12 - 0.09	1.32 1.22	-0.90 - 0.65	-0.21 0.11	0.07 0.25
13.1 4.4 10.9	-0.21 0.16	1.37 1.44	-0.76 - 0.87	-0.38 0.14	0.21 0.12
13.1 8.6 1.0	0.01 0.28	1.26 1.38	-0.71 - 0.53	-0.36 - 0.34	0.23 0.36
13.1 8.6 4.5	-0.14 0.13	1.35 1.37	-0.70 - 0.53	-0.32 - 0.19	0.24 0.40
13.1 8.6 8.8	-0.25 - 0.05	1.13 1.20	-0.70 - 0.68	-0.30 - 0.08	0.23 0.23
16.9 5.6 1.0	0.24 0.53	1.37 1.47	-0.71 - 0.54	-0.38 - 0.27	0.42 0.39
16.9 5.6 6.0	0.18 0.16	1.34 1.40	-0.69 - 0.57	-0.19 - 0.13	0.26 0.21
16.9 5.6 11.3	0.01 0.14	1.21 1.28	-0.64 - 0.61	-0.21 - 0.02	0.14 - 0.02
16.9 11.5 1.0	0.10 0.16	1.14 1.18	-0.74 - 0.61	-0.29 - 0.32	0.40 0.52
16.9 11.5 5.4	-0.20 0.05	1.12 1.27	-0.66 - 0.63	-0.12 - 0.15	0.26 0.30
16.9 11.5 11.2	-0.20 - 0.03	1.19 1.17	-0.82 - 0.72	-0.13 0.07	-0.02 0.25
21.2 5.6 1.0	-0.04 0.21	1.31 1.38	-0.73 - 0.55	-0.20 - 0.29	0.36 0.35
21.2 5.6 8.3	-0.06 - 0.00	1.22 1.29	-0.77 - 0.62	-0.03 - 0.18	0.04 0.09
21.2 5.6 15.6	-0.14 - 0.07	1.21 1.39	-0.81 - 0.87	-0.00 0.07	-0.03 0.19
21.2 11.5 1.0	-0.21 0.11	1.20 1.20	-0.83 - 0.57	-0.25 - 0.26	0.30 0.30
21.2 11.5 9.7	0.04 0.08	1.16 1.19	-0.76 - 0.65	-0.06 - 0.27	0.17 0.18
21.2 11.5 15.5	-0.27 - 0.13	1.29 1.26	-0.69 - 0.97	-0.04 - 0.10	0.04 0.10
24.7 5.0 1.0	-0.31 0.18	1.33 1.83	-0.80 - 0.54	-0.29 - 0.35	0.21 0.33
24.7 5.0 10.4	-0.28 - 0.21	1.06 1.55	-0.89 - 0.51	-0.03 - 0.03	0.03 0.10
24.7 5.0 19.7	-0.22 - 0.11	0.88 1.28	-0.95 - 0.75	0.45 0.21	-0.11 0.04
24.7 10.1 1.0	-0.01 - 0.00	1.24 1.78	-0.74 - 0.55	-0.27 - 0.35	0.29 0.36
24.7 10.1 14.6	-0.13 - 0.04	1.04 1.42	-0.79 - 0.72	0.13 0.16	0.00 0.06
24.7 10.1 19.7	-0.31 - 0.19	0.97 1.01	-0.72 - 0.94	0.10 0.05	-0.22 0.03

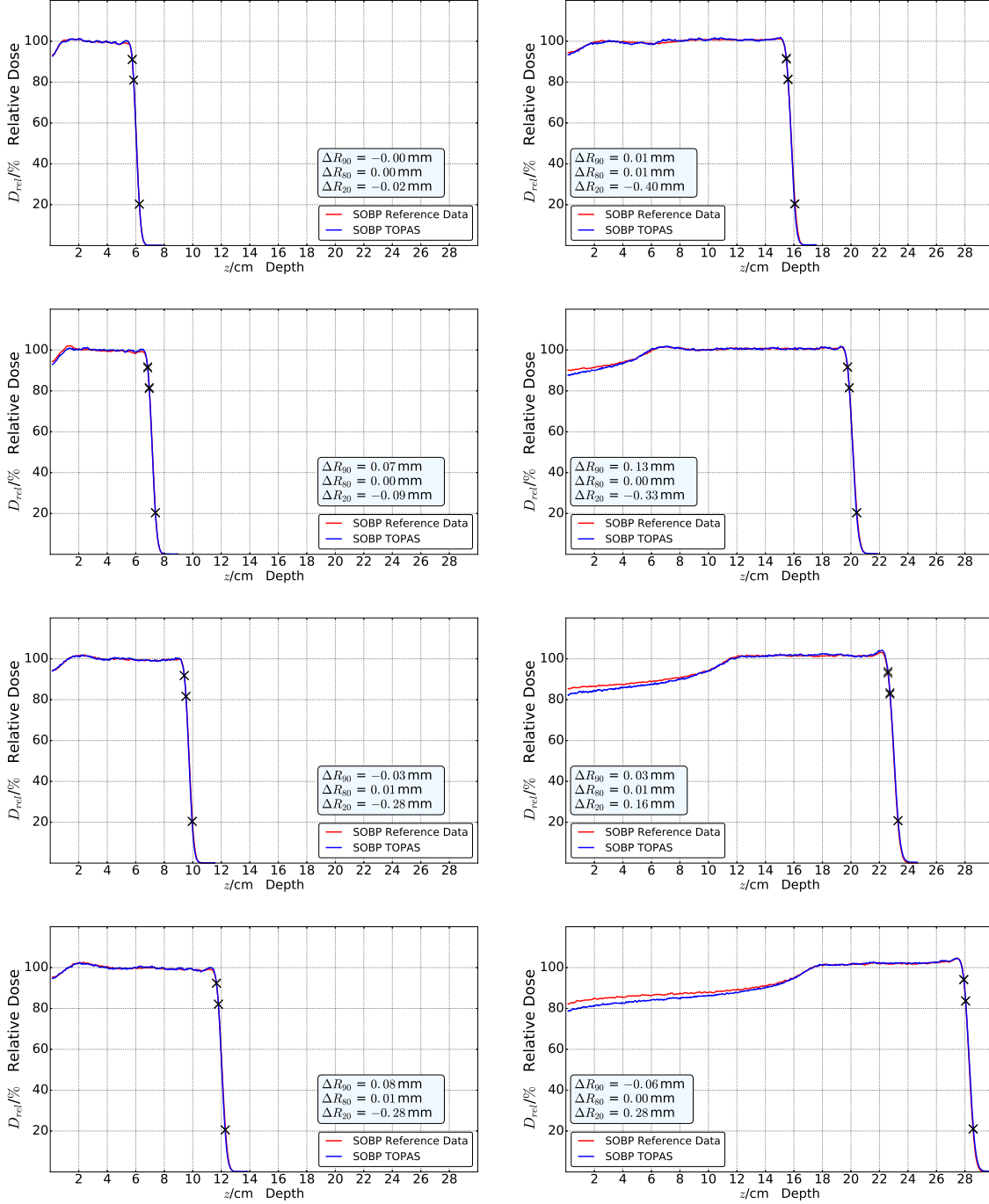


Figure A: Simulated and measured (validation data) spread-out Bragg peaks with $R_{\text{req}} = 5.8, 6.9, 9.5, 11.8, 15.5, 19.8, 22.6, 28.0$ cm. The corresponding modulations are listed in Table B. The depth differences at three characteristic dose points at the distal fall-off region are calculated. Two default ring apertures ($R_{\text{inner}} = 8.15$ cm) are used. The snout position is $d_{\text{pos}} = 10$ cm.

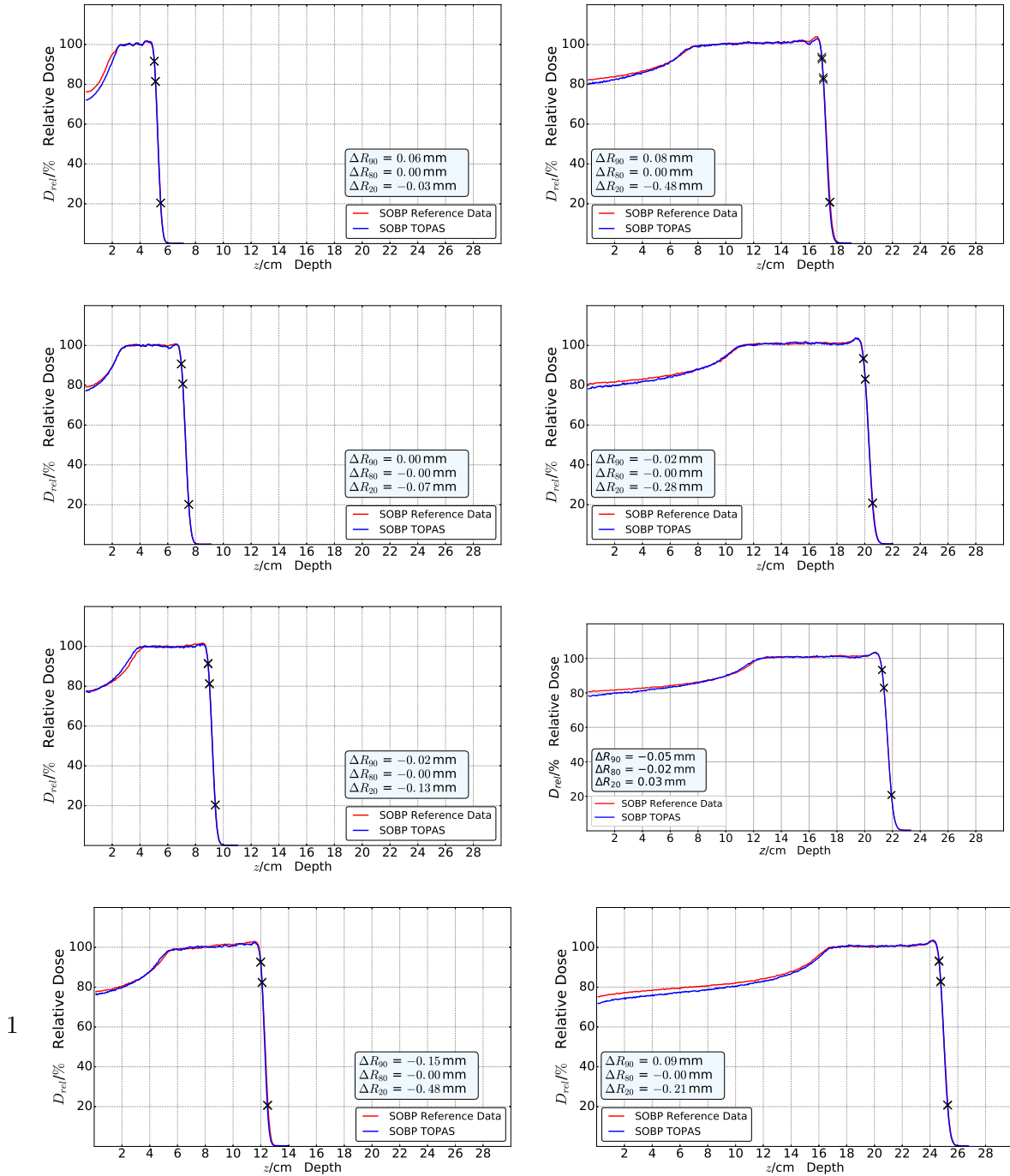


Figure B: Simulated and measured (validation data) spread-out Bragg peaks with $R_{\text{req}} = 5.0, 7.0, 8.9, 11.9, 16.9, 19.9, 21.2, 24.7$ cm. The corresponding modulations are listed in Table B. The depth differences at three characteristic dose points at the distal fall-off region are calculated. Two default ring apertures ($R_{\text{inner}} = 8.15$ cm) are used. The snout position is $d_{\text{pos}} = 10$ cm.

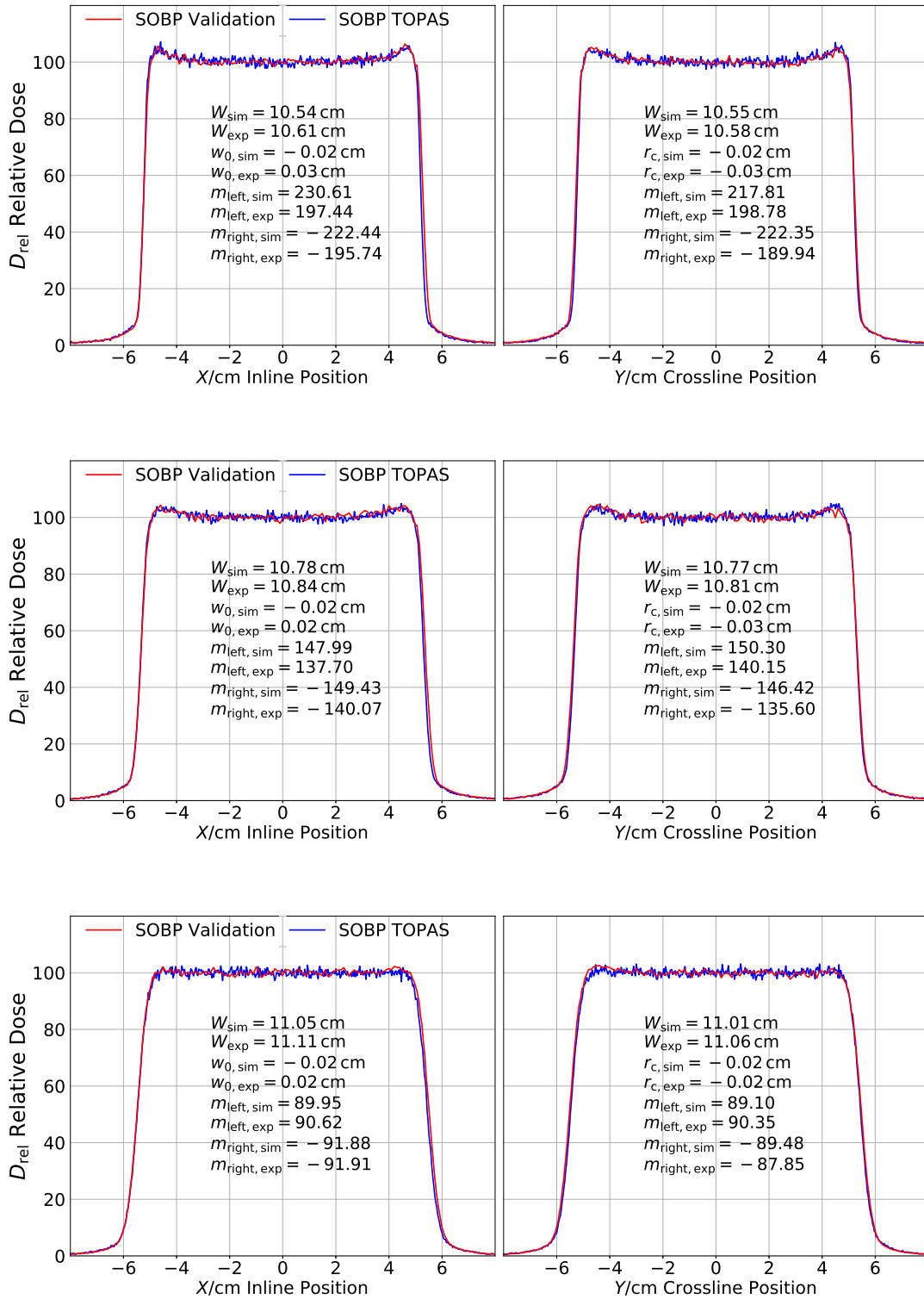


Figure C: Simulated and measured (validation data) lateral profiles, which belong to a SOBP field with $R_{\text{req}} = 16.9$ cm and $M_{\text{req}} = 11.5$ cm and a depth positions from top to bottom $z_{\text{pos}} = 1.0, 5.4, 11.2$ cm. (center) The field sizes W , the central field positions w_0 and the slopes of the left m_l and the right m_r profile flank are calculated. Two square apertures (10 cm \times 10 cm) are used. The snout position is $d_{\text{pos}} = 10$ cm.

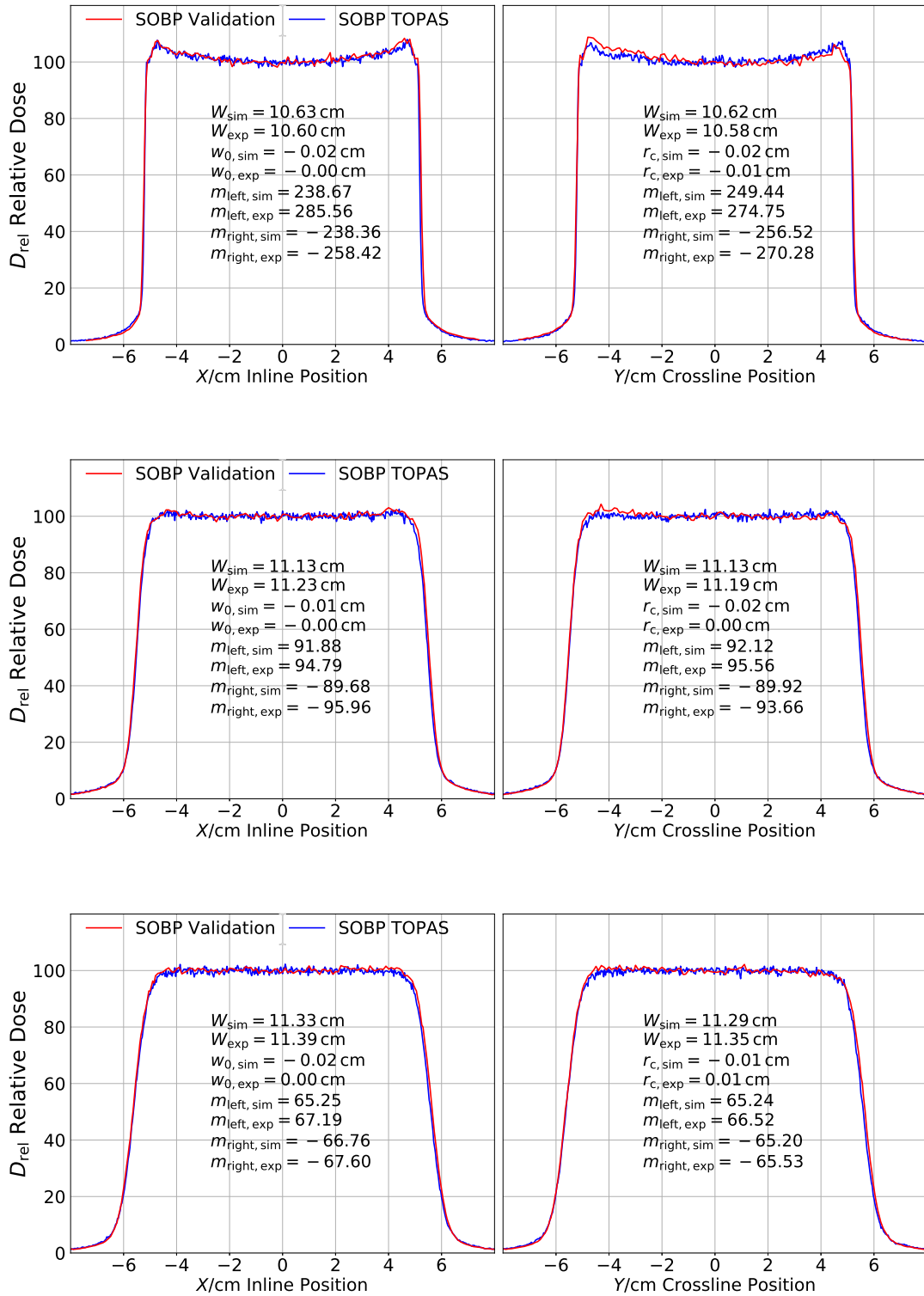


Figure D: Simulated and measured (validation data) lateral profiles, which belong to a SOBP field with $R_{\text{req}} = 24.7$ cm and $M_{\text{req}} = 10.1$ cm and a depth positions from top to bottom $z_{\text{pos}} = 1.0, 14.6, 19.7$ cm. (center) The field sizes W , the central field positions w_0 and the slopes of the left m_l and the right m_r profile flank are calculated. Two square apertures (10 cm \times 10 cm) are used. The snout position is $d_{\text{pos}} = 10$ cm.

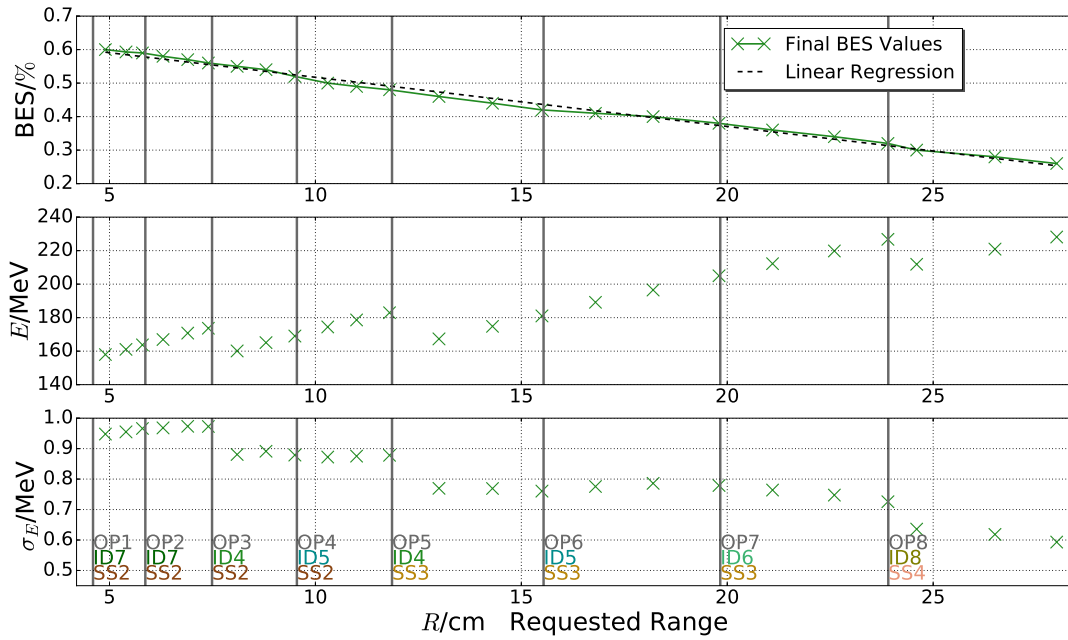


Figure E: Illustration of the parameters of the initial beam energy distribution after the BES adjustment and before the range adjustment for all requested ranges R_{req} , which belong to the reference data \mathcal{D}_{Ref} . The upper sub-plot shows the finally optimized BES (relative standard deviation $\sigma_{E,rel}$) values. The center sub-plot illustrates the the mean beam energies \bar{E} , before the range adjustment. The lower sub-plot visualizes the absolute standard $\sigma_{E,abs}$, which is the product of the BES and \bar{E} .

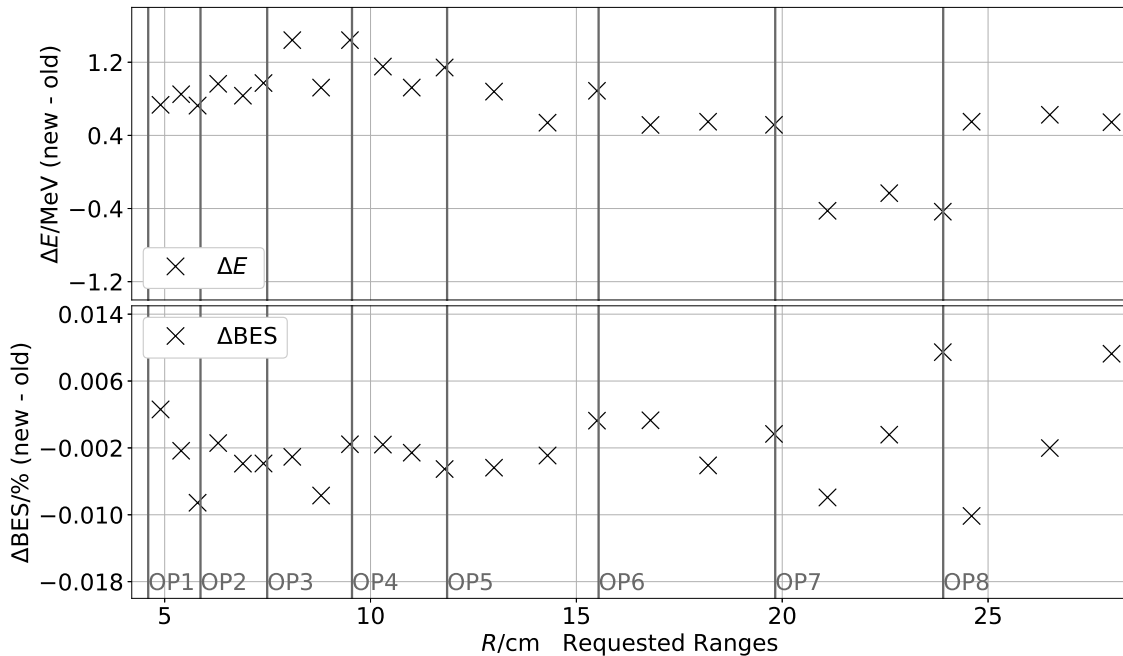


Figure F: Differences of the mean initial beam energy (top) before (old) and after (new) the option dependent range adjustments. The corresponding BES differences (bottom) are derived by assuming a constant absolute standard deviation $\sigma_{E,abs}$ within an option.

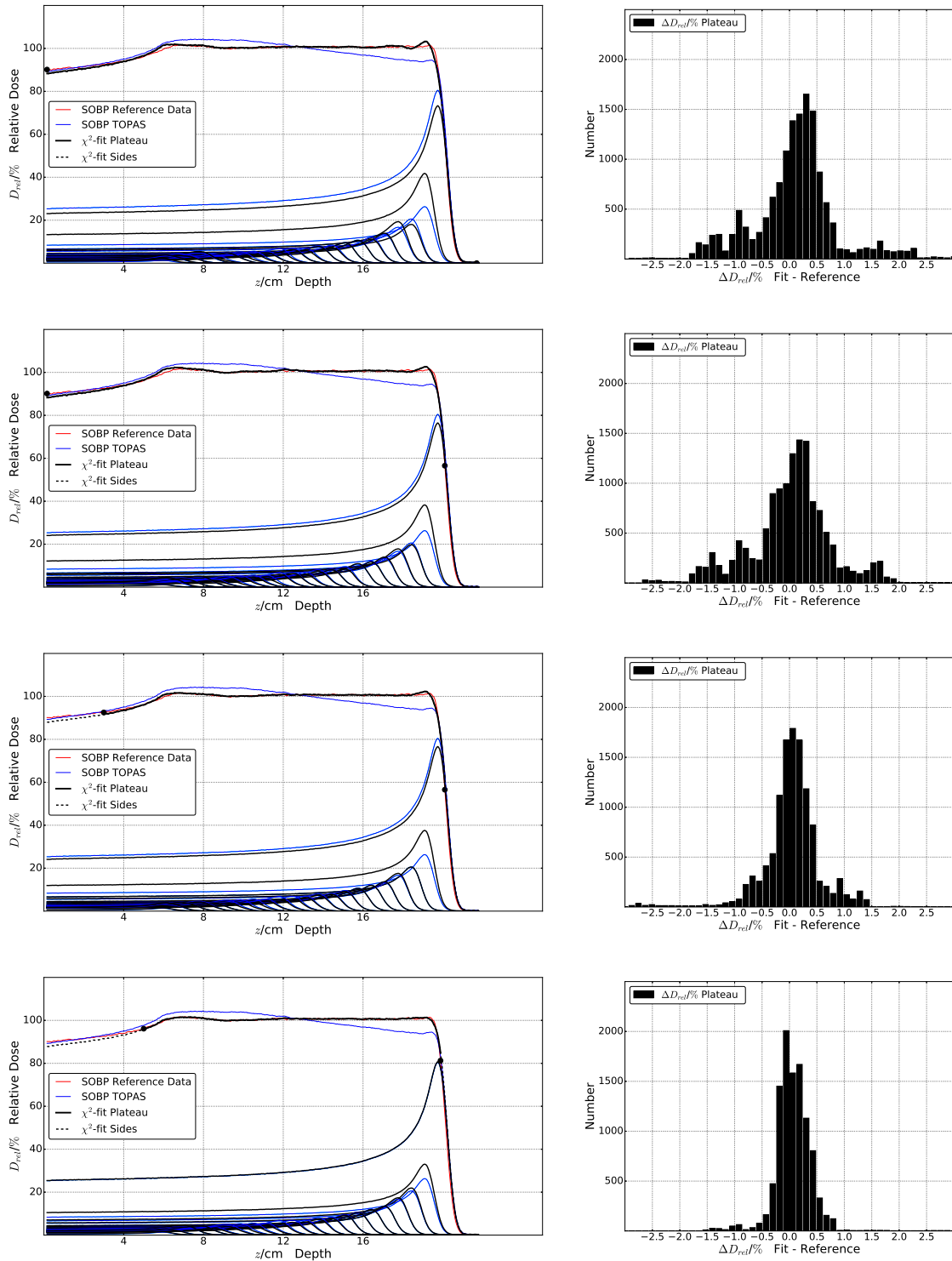


Figure G: χ^2 -fits with varying fit intervals of a reference data SOBP ($R = 19.8$ cm, $M = 17.0$ cm) using TOPAS PP as base functions. The first fit interval (upper sub-plot) spreads over the depth interval $[0$ cm/ 21.7 cm], the second one over $[0$ cm/ 20.1 cm] (second sub-plot from above), the third $[3$ cm/ 20.1 cm] (second sub-plot from bottom) and the fourth over $[5$ cm/ 19.8 cm] (bottom sub-plot). On the right sides there are the corresponding dose difference histograms.

B Output Factor Simulations for Absolute Dosimetry

Table H: List of requested ranges R_{req} , modulations M_{req} and depth calibration points z_{calib} of the reference fields, which are used in the patient quality assurance measurements at UPTD.

$R_{req} M_{req} z_{calib} // \text{cm}$	$R_{req} M_{req} z_{calib} // \text{cm}$	$R_{req} M_{req} z_{calib} // \text{cm}$
4.8 4.6 2.77	10.7 8 6.97	21.9 11.5 16.42
6.6 5 4.37	15 7.1 11.72	27.5 13 21.27
8.5 6.2 5.67	16 10 11.27	

Table I: List of requested ranges R_{req} , modulations M_{req} of the SOBPs fields, which are measured in reference measurements for research purposes at UPTD and are used to validate the prediction of output factor with TOPAS. All fields have a constant requested modulation of 4 cm.

R_{req}/cm	M_{req}/cm	R_{req}/cm	M_{req}/cm	R_{req}/cm	M_{req}/cm
5	4	10.5	4	18.5	4
5.5	4	11	4	19	4
6	4	11.2	4	20	4
6.5	4	11.5	4	21	4
7	4	12	4	22	4
7.5	4	13	4	23	4
7.7	4	14	4	23.5	4
8	4	15	4	24	4
8.6	4	15.5	4	25	4
9	4	16	4	26	4
9.5	4	17	4	27	4
10	4	18	4	28	4

Table J: List of requested ranges R_{req} , modulations M_{req} of the SOBPs fields, which are measured in reference measurements for research purposes at UPTD and are used to validate the prediction of output factor with TOPAS. There are five field sections, each with a constant requested range of 4 cm and varying modulations.

R_{req}/cm	M_{req}/cm	R_{req}/cm	M_{req}/cm	R_{req}/cm	M_{req}/cm
11	2	14	6	18	1.0
11	4	14	8	18	1.6
11	6	14	10	18	3.3
11	8	14	12	18	1.0
11	10	14	14	18	1.6
22	7	26	4		
22	11	26	6		
22	14	26	8		
22	17	26	10		
		26	12		
		26	15		

Table K: Mean values and the corresponding variances of $\Delta\psi_{\text{rel}}$ for the data sets \mathcal{M}_{Ref} and \mathcal{M}_{Res} .

Data	Value/%	V_{IC23_1}	V_{IC23_2}	V_{IC23_3}	V_{IC23_4}
$(\mathcal{M}_{\text{Ref}})$	$\mu(\Delta\psi_{\text{rel}})$	0.41	-0.06	-0.23	0.63
	$\nu(\Delta\psi_{\text{rel}})$	7.15	9.46	4.2	145.63
$(\mathcal{M}_{\text{Res}}, \text{Part 1})$	$\mu(\Delta\psi_{\text{rel}})$	1.69	1.3	1.02	0.44
	$\nu(\Delta\psi_{\text{rel}})$	0.8	0.39	0.34	0.24
$(\mathcal{M}_{\text{Res}}, \text{Part 2})$	$\mu(\Delta\psi_{\text{rel}})$	1.36	0.67	0.51	3.05
	$\nu(\Delta\psi_{\text{rel}})$	2.03	1.66	1.74	1.91

Table L: Parameters of the $\Delta\psi_{\text{rel}}$ distribution, which belongs to $(\mathcal{M}_{\text{Res}}, \text{Part 1})$. For each option, the mean value, the variance and the slope is calculated.

Volume	Value/%	Opt 1	Opt 2	Opt 3	Opt 4	Opt 5	Opt 6	Opt 7
V_{IC23_1}	$\mu_{\text{opt}}(\Delta\psi_{\text{rel}})$	2.58	1.64	-0.19	1.43	0.67	2.82	2.9
	$\nu_{\text{opt}}(\Delta\psi_{\text{rel}})$	0.01	0.05	2.60	0.96	0.16	0.91	0.92
	$m_{\text{opt}}(\Delta\psi_{\text{rel}})$	0.3	0.29	-0.41	-0.76	-0.15	0.01	-0.31
V_{IC23_2}	$\mu_{\text{opt}}(\Delta\psi_{\text{rel}})$	2.52	1.31	-0.57	0.84	0.34	2.28	2.41
	$\nu_{\text{opt}}(\Delta\psi_{\text{rel}})$	0.0	0.1	.66	0.81	0.35	0.66	0.15
	$m_{\text{opt}}(\Delta\psi_{\text{rel}})$	0.01	-0.29	-0.23	-0.82	-0.17	-0.14	-0.31
V_{IC23_3}	$\mu_{\text{opt}}(\Delta\psi_{\text{rel}})$	1.6	0.92	-0.86	0.5	0.33	2.35	2.29
	$\nu_{\text{opt}}(\Delta\psi_{\text{rel}})$	0.0	0.02	0.27	0.95	0.25	0.13	0.79
	$m_{\text{opt}}(\Delta\psi_{\text{rel}})$	0.02	-0.19	-0.33	-0.91	-0.18	-0.14	-0.26
V_{IC23_4}	$\mu_{\text{opt}}(\Delta\psi_{\text{rel}})$	0.59	-0.15	-2.3	-0.84	1.97	2.33	1.49
	$\nu_{\text{opt}}(\Delta\psi_{\text{rel}})$	0.04	0.06	0.37	0.27	0.18	0.22	0.57
	$m_{\text{opt}}(\Delta\psi_{\text{rel}})$	0.55	0.33	-0.39	-0.47	-0.1	0.01	-0.27

Table M: Distribution of the $\Delta\psi_{\text{rel}}$ values which belong to $(\mathcal{M}_{\text{Res}}, \text{Part 2})$. For each dataset with constant R_{req} , the mean value, the variance and the slope is calculated.

Volume	Value/%	R_{req}/cm	R_{req}/cm	R_{req}/cm	R_{req}/cm	R_{req}/cm
		11	14	18	22	26
V_{IC23_1}	$\mu_R(\Delta\psi_{\text{rel}})$	1.32	-0.72	1.38	1.42	3.38
	$\nu_R(\Delta\psi_{\text{rel}})$	0.7	2.74	4.23	0.42	2.04
	$m_R(\Delta\psi_{\text{rel}})$	-0.19	-0.21	-0.22	-0.11	-0.18
V_{IC23_2}	$\mu_R(\Delta\psi_{\text{rel}})$	0.6	-0.73	0.84	0.86	1.76
	$\nu_R(\Delta\psi_{\text{rel}})$	0.39	2.55	3.69	0.33	1.34
	$m_R(\Delta\psi_{\text{rel}})$	-0.13	-0.19	-0.2	-0.09	-0.14
V_{IC23_3}	$\mu_{\text{opt}}(\Delta\psi_{\text{rel}})$	0.35	-1.11	0.67	0.94	1.71
	$\nu_R(\Delta\psi_{\text{rel}})$	0.33	2.64	3.57	0.45	1.71
	$m_R(\Delta\psi_{\text{rel}})$	-0.1	-0.21	-0.2	-0.11	-0.16
V_{IC23_4}	$\mu_R(\Delta\psi_{\text{rel}})$	-1.17	0.75	0.94	0.87	13.88
	$\nu_R(\Delta\psi_{\text{rel}})$	0.55	4.6	3.44	0.3	0.67
	$m_R(\Delta\psi_{\text{rel}})$	-0.16	-0.29	-0.2	-0.07	-0.1

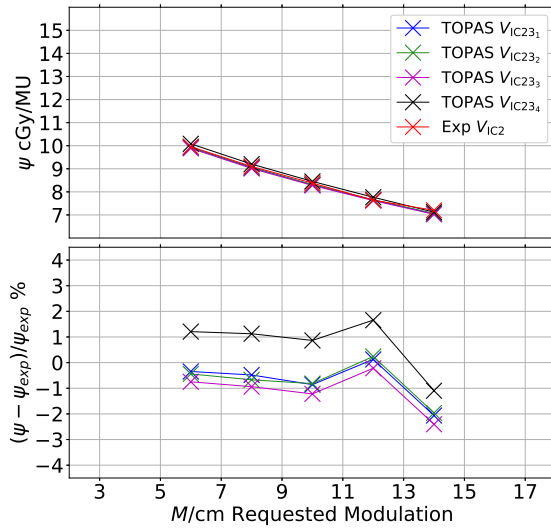


Figure H: $\psi_{rel}(M_{req})$ and $\Delta\psi_{rel}(M_{req})$ distributions, which are derived by comparing TOPAS simulations to the second part of \mathcal{M}_{Res} , with constant range $R_{req} = 14$ cm. Four different volumes are used to compare the accuracy of the mapping of the MU charge collection. All output factors are normalized to the reference field ($R_{req} = 16$ cm and $M_{req} = 11$ cm).

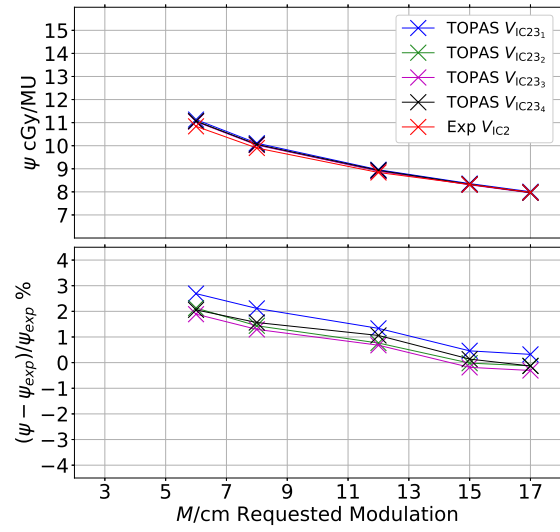


Figure I: $\psi_{rel}(M_{req})$ and $\Delta\psi_{rel}(M_{req})$ distributions, which are derived by comparing TOPAS simulations to the second part of \mathcal{M}_{Res} , with constant range $R_{req} = 18$ cm. Four different volumes are used to compare the accuracy of the mapping of the MU charge collection. All output factors are normalized to the reference field ($R_{req} = 16$ cm and $M_{req} = 11$ cm).

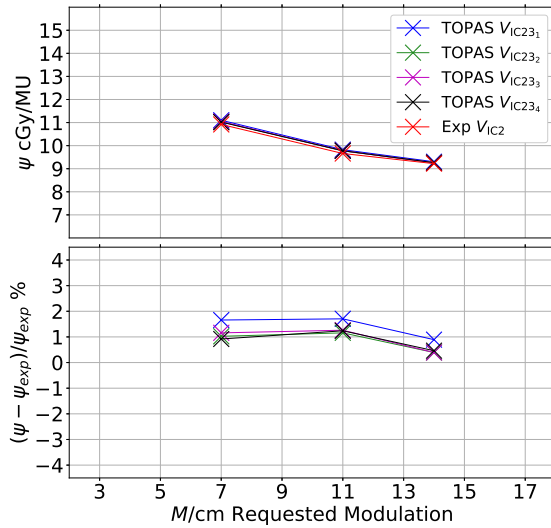


Figure J: $\psi_{rel}(M_{req})$ and $\Delta\psi_{rel}(M_{req})$ distributions, which are derived by comparing TOPAS simulations to the second part of \mathcal{M}_{Res} , with constant range $R_{req} = 22$ cm. Four different volumes are used to compare the accuracy of the mapping of the MU charge collection. All output factors are normalized to the reference field ($R_{req} = 16$ cm and $M_{req} = 11$ cm).

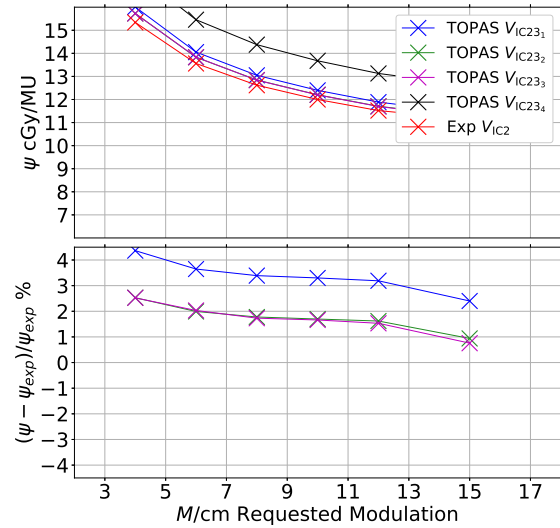


Figure K: $\psi_{rel}(M_{req})$ and $\Delta\psi_{rel}(M_{req})$ distributions, which are derived by comparing TOPAS simulations to the second part of \mathcal{M}_{Res} , with constant range $R_{req} = 26$ cm. Four different volumes are used to compare the accuracy of the mapping of the MU charge collection. All output factors are normalized to the reference field ($R_{req} = 16$ cm and $M_{req} = 11$ cm).

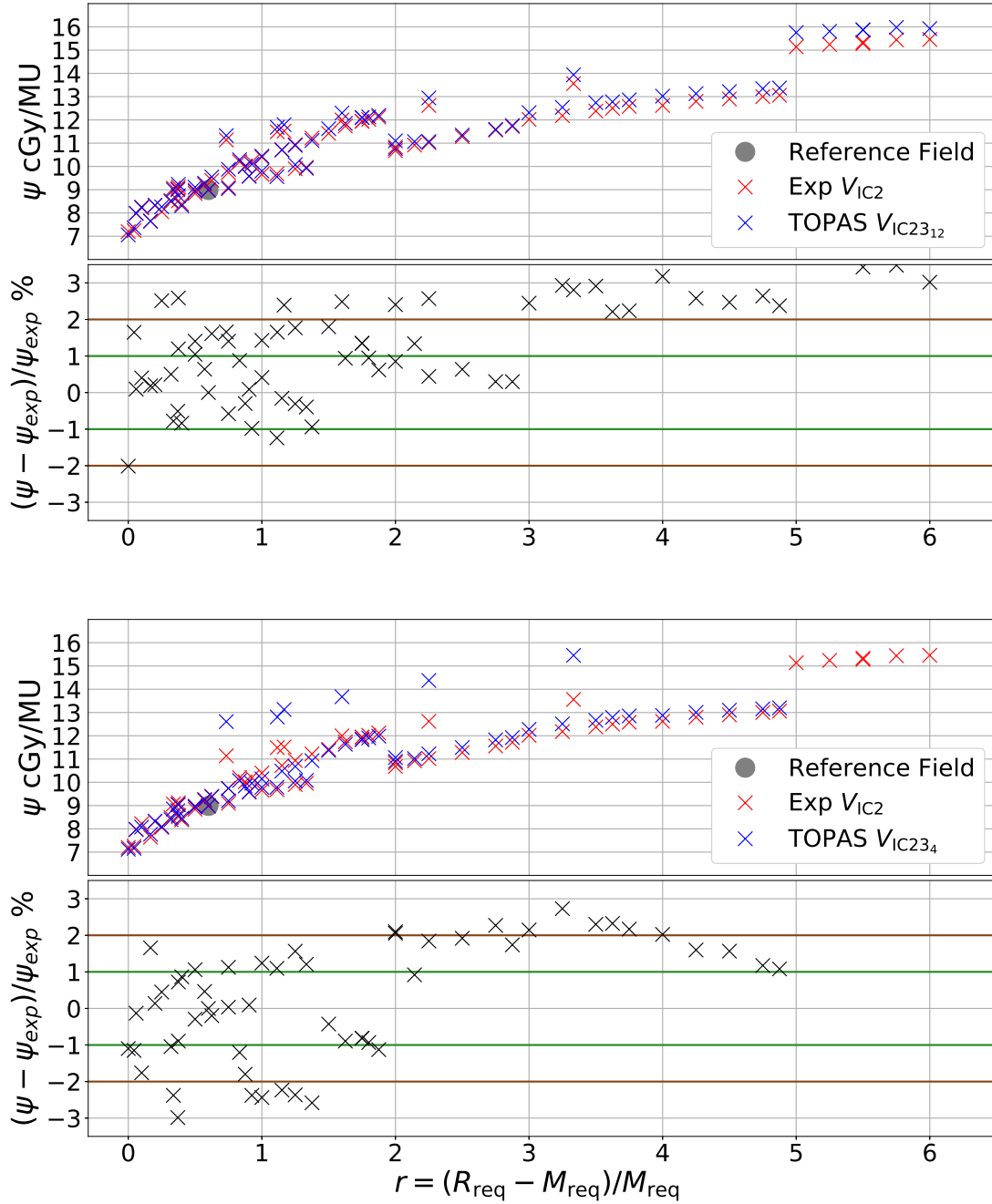


Figure L: $\psi_{\text{rel}}(r)$ and $\Delta\psi_{\text{rel}}(r)$ distributions, which are derived by comparing TOPAS simulations to the measured data sets \mathcal{M}_{Ref} and \mathcal{M}_{Res} . All output factors are normalized to the reference field ($R_{\text{req}} = 16$ cm and $M_{\text{req}} = 11$ cm). The volumes $V_{\text{IC}23_{12}} = V_{\text{IC}23_1} + V_{\text{IC}23_2}$ and $V_{\text{IC}23_4}$ are used to compare the accuracy of the mapping of the MU charge collection.

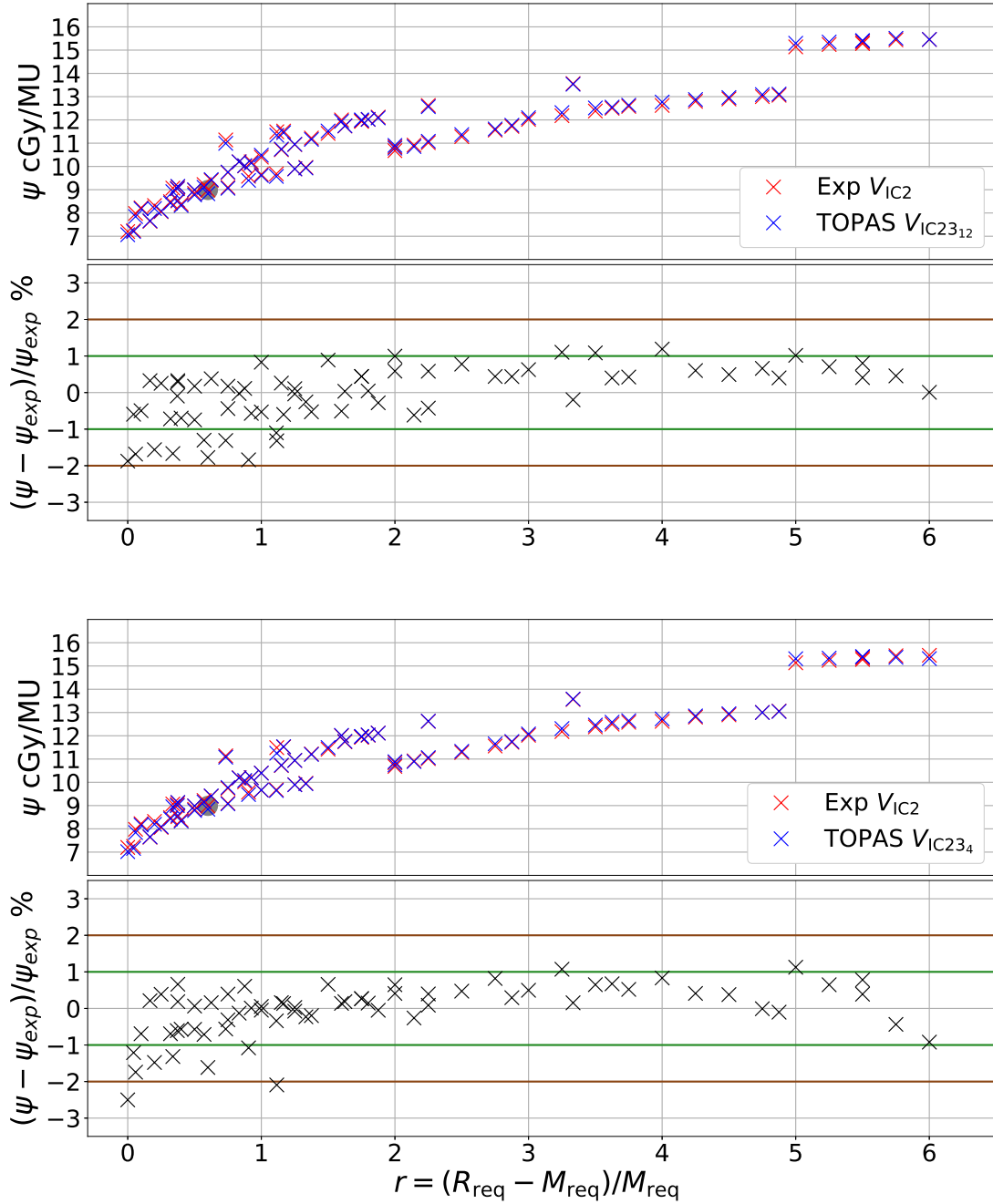


Figure M: $\psi_{rel}(r)$ and $\Delta\psi_{rel}(r)$ distributions, which are derived by comparing TOPAS simulations to the measured data sets M_{Ref} and M_{Res} . The simulated output factors are adjusted with an option dependent calibration factor. The volumes $V_{IC23_{12}} = V_{IC23_1} + V_{IC23_2}$ and V_{IC23_4} are used to compare the accuracy of the mapping of the MU charge collection.

C TOPAS Simulation of a Proton Treatment Plan

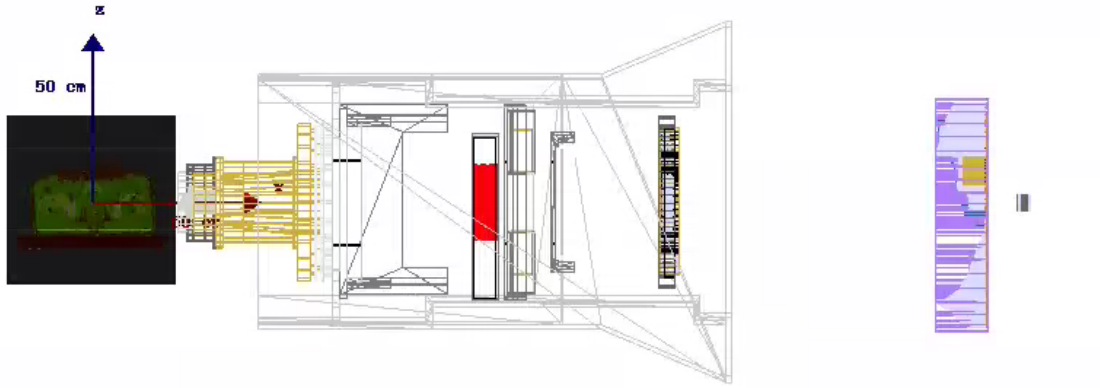


Figure N: Illustration of the geometrical setup in TOPAS, which belong to the first field of the proton plan for Patient1. The gantry angle is $\Theta_{Gantry} = -90^\circ$ and the snout position $d_{pos} = 29.96$ cm.

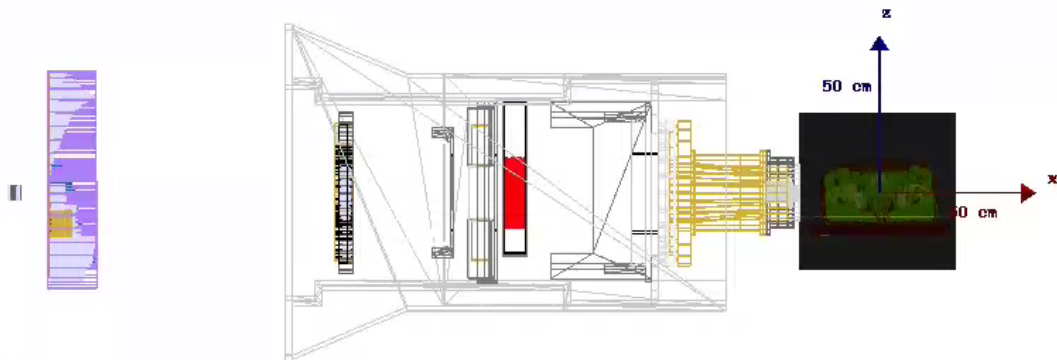


Figure O: Illustration of the geometrical setup in TOPAS, which belong to the first field of the proton plan for Patient1. The gantry angle is $\Theta_{Gantry} = -270^\circ$ and the snout position $d_{pos} = 29.5$ cm.

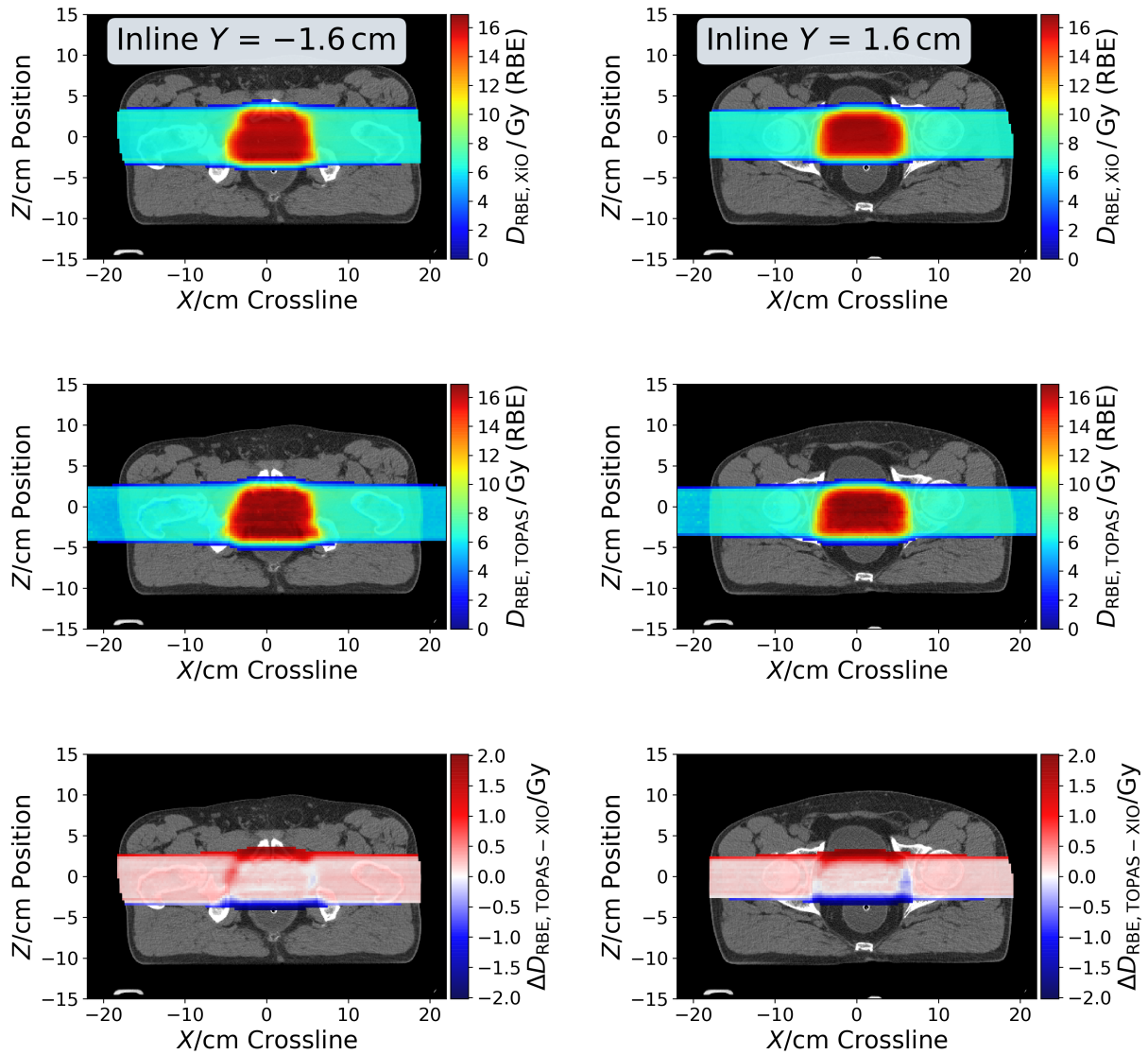


Figure P: Planned (XiO, top) and simulated (TOPAS, center) dose distributions, which correspond to the proton plan of Patient 1. The dose differences (TOPAS - XiO) are visualized on the bottom sub-plots. Only doses above 3% of the mean dose value at the central high dose region of the planned distribution, are visualized. The dose distributions are shown for two different computed tomography slices, with the inline positions $Y = -1.6$ cm (left) and $Y = 1.6$ cm (right). All doses are given in the units of RBE, whereby a constant RBE of 1.1 is applied.